Antireflection coatings based on La doped ZnO and Diamond-like carbon via wet-chemistry and vapor deposition methods for PV Applications

By

M. Altamash Shabbir

Reg # 00000319845

Session 2019-21

Supervised

by

Prof. Dr. Zuhair S. Khan

U.S. Pakistan Center for Advanced Studies in Energy (USPCAS-E)

National University of Sciences and Technology (NUST)

H-12, Islamabad 44000, Pakistan

March 2022

Antireflection coatings based on La doped ZnO and Diamond-like carbon via wet-chemistry and vapor deposition methods for PV Applications

By

M. Altamash Shabbir

Reg # 00000319845

Session 2019-21

Supervised

by

Prof. Dr. Zuhair S. Khan

A Thesis Submitted to the U.S. Pakistan Centre for Advanced Studies in Energy in partial fulfillment of the requirements for the degree of

MASTERS of SCIENCE in

ENERGY SYSTEMS ENGINEERING

U.S. Pakistan Center for Advanced Studies in Energy (USPCAS-E)

National University of Sciences and Technology (NUST)

H-12, Islamabad 44000, Pakistan

March 2022

THESIS ACCEPTANCE CERTIFICATE

Certified that final copy of MS thesis written by Mr. M. Altamash Shabbir, (Registration No 00000319845) of U.S.-Pakistan Center for Advanced Studies in Energy (USPCAS-E), NUST has been vetted by undersigned, found complete in all respects as per NUST Statues/Regulations, is within the similarity indices limit and is accepted as partial fulfillment for the award of MS degree. It is further certified that necessary amendments as pointed out by GEC members of the scholar have also been incorporated in the said thesis.

Signature: _____

Name of Supervisor: Prof. Dr. Zuhair S. Khan

Date: _____

Signature (HoD): _____

Date: _____

Signature (Dean/Principal): _____

Date: _____

Certificate

This is to certify that work in this thesis has been carried out by **Mr. Altamash Shabbir** and completed under my supervision in Advanced Energy Materials and Systems Laboratory, USPCAS-E, National University of Sciences and Technology, H-12, Islamabad, Pakistan.

Supervisor: _____

Prof. Dr. Zuhair S. Khan
U.S. Pakistan Centre for Advanced Studies in Energy
NUST, Islamabad

GEC member 1: _____

Prof. Dr. Naseem Iqbal
U.S. Pakistan Centre for Advanced Studies in Energy
NUST, Islamabad

GEC member 2: _____

Dr. Nadia Shahzad
U.S. Pakistan Centre for Advanced Studies in Energy
NUST, Islamabad

GEC member 3: _____

Dr. Ghulam Ali
U.S. Pakistan Centre for Advanced Studies in Energy
NUST, Islamabad

HOD-ESE: _____

Dr. Rabia Liaqat
Department of Energy Systems Engineering
NUST, Islamabad

Principal: _____

Prof. Dr. Adeel Waqas
U.S. Pakistan Centre for Advanced Studies in Energy
NUST, Islamabad

Acknowledgments

All praise to Allah Almighty who gave me the strength and knowledge to do the work presented in this thesis.

I would like to express my sincere gratitude to my research supervisor, Prof. Dr. Zuhair S. Khan for letting me be part of the research group at Advanced Energy Materials Lab, USPCAS-E, NUST, Islamabad. I feel privileged to have worked under his kind supervision. It's the blend of his patience, persistence, guidance, and motivation that made me accomplish my research aims in due time. He polished my research skills and I have learned a lot under his supervision and guidance.

I would also like to thank the members of my GEC committee, Dr. Naseem Iqbal, Dr. Ghulam Ali, and Dr. Nadia Shahzad who honored my committee's presence. I would like to sincerely thank my dear brother Mr. Hafiz M. Haseeb, my fellows and friends Wajahat Qasim, and Zain Hussain for their unconditional support. Especially, I pay gratitude to Lab Engineers Mr. Asghar Ali, Mr. Aamir Satti, Mr. Nisar Ahmad, and Miss Hina Pervaiz for their unmatchable support during the whole research work.

I gratefully acknowledge the financial support provided by the USPCAS-E / NUST

Abstract

In this era, renewable energy technologies are suitable to meet the challenges of fuel depletion and global warming. One of the potential approaches to mitigate the reliance on fossil fuels is to generate electricity by photovoltaic technology. In recent years, huge advances have been made in the development of photovoltaic technology. Reflection losses of incident light on the Solar cell is an important factor that affects the efficiency of solar cells. Antireflection (AR) coatings can enhance the optical characteristics of Solar Cells. Diamond-like carbon (DLC) has high hardness, is chemically inert, and optically transparent. Due to its superior antireflection properties, DLC films are more suited for photovoltaic technology. Rare earth metal doping in Zinc Oxide can introduce structural defects that help capture light and improve the photocatalytic performance of the Solar Cells. In this work, we synthesized Diamond-like carbon and Lanthanum doped ZnO film via wet chemistry and vapor phase deposition technique. In the first section, we report two different methods to fabricate DLC thin film over the surface of the silicon and FTO substrates via PECVD and Electrodeposition techniques. In the second section, we report the fabrication process of Lanthanum doped ZnO via the sol gel/spin coating method. Various process routes such as the effect of substrate temperature, the effect of voltage, and the effect of concentration of dopants, etc. were studied. Morphological, structural, optoelectrical, and wettability properties of the synthesized film were analyzed by using Scanning Electron Microscopy, FTIR, Raman Spectroscopy, UV-Vis NIR Spectrophotometer, Hall Effect, and Water contact angle measurement, etc. The DLC films were deposited at 2.7, 4, 6, 8, and 10 Volts by electrodeposition route, and it was shown that for a fixed electrolyte concentration and electrode spacing, the applied voltage can be adjusted to obtain varying deposition rates. Likewise, the solution concentration was varied in the 2 vol.% to 10 vol.%, and it was demonstrated that by increasing the solution concentration the deposition rate increases. The increase in the deposition rate was evidenced by an increase in the deposition current as well as the roughness of the films. It was noticed that smaller-sized, well-defined, and more uniform DLC films were obtained at lower concentrations and low voltage levels. The band gap was varied from 2.91 eV to 3.39 eV. Properties of DLC deposited via PECVD also depend on the substrate temperature. DLC deposited at ambient temperature shows high optical transparency throughout the visible and IR region as compared to 100 ^{o}C deposited

DLC film. In the case of ZnO, studies revealed that ZnO has a wurtzite hexagonal structure and after doping of La into ZnO, reduced the particle size of the films. The bandgap of the doped ZnO was found to vary between 3.22 to 3.29 eV. Synthesized La-doped ZnO thin film shows a hydrophilic property. It clearly showed that the reflection had reduced remarkably after depositing DLC and La-doped ZnO film on the substrate surface. This work demonstrates that DLC and La-doped ZnO films have the potential to be utilized as antireflection layers in photovoltaic applications.

Keywords: Photovoltaic, Antireflection coating, Diamond-like Carbon, La-doped ZnO.

Table of Contents

List of Figures

List of Tables

List of Abbreviations / Nomenclatures

GWP	Global warming potential
GHGs	Green House Gasses
CO_2	Carbon dioxide
UNFCCC	United nations framework convention on climate change
CH_4	Methane
NO_2	Nitrous Oxide
COP	Conferences of the Parties
CPEC	China-Pakistan economic corridor
CPVs	Concentrating photovoltaics
CSP	Concentrated solar power
OSCs	Organic solar cells
PSCs	Polymer solar cells
DSSCs	Dye-sensitized solar cells
CIGS	Copper indium gallium diselenide
CdTe	Cadmium telluride
CIS	Copper indium diselenide
CZTS	Copper zinc tin sulphide/selenide
DLC	Diamond like Carbon
ZnO	Zinc Oxide
LZO	Lanthanum doped Zinc Oxide
AZO	Aluminium doped Zinc Oxide
MW	Mega Watt
ARCs	Antireflection Coatings
Si	Silicon
FTO	Fluorine doped Tin Oxide
SLG	Soda lime glass
PECVD	Plasma Enhanced Chemical Vapor Deposition.
CH_3^+	Methyl Radicals
C-H	Hydrogenated carbon
SiNWs	silicon nanowires
Psi	Porous silicon
SEM	Scanning Electron Microscopy

EDS	Energy Dispersive Spectroscopy
FTIR	Fourier Transform Infrared Spectroscopy
ZnSe	Zinc Selenide
TiO_2	Titanium dioxide
SiO_2	Silicon dioxide
PCE	Power Conversion Efficiency
a-C:H	Hydrogenated Amorphous Carbon
ta-C	Tetrahedral Amorphous Carbon
ta-C:H	Hydrogenated tetrahedral Amorphous Carbon
SnO_2	Tin Oxide
QDs	Quantum Dots
ITO	Indium Tin Oxide
CVD	Chemical vapor deposition
PVD	Physical Vapor deposition
RF-PECVD	Radio Frequency Plasma Enhanced Chemical Vapor Deposition.
XRD	X-ray diffraction
BSE	Back Scattered Electrons
AFM	Atomic Force Microscopy
SO	Surface optical
LO	Longitudinal optical
TO	Transverse optical
WCA	Water contact Angle
CA	Contact Angle
UV-Vis	Ultraviolet -Visible
IR	Infrared Region
SCs	Solar Cells
MgF_2	Magnesium Fluoride

List of Journal/Conference Papers

1. "Diamond-Like Carbon Film Deposited Via Electrochemical Route for Antireflection Applications in Photovoltaic." Altamash Shabbir[1], Zuhair S. Khan*, Asghar Ali, Zain Hussain, Wajahat Qasim, Nisar Ahmed.
   Journal of Key Engineering Materials, Scientific.net ISSN: 1662-9795. **(Under Review)**
2. "Lanthanum doped ZnO Film Deposited via Wet Chemistry Route for Photovoltaic Applications." Altamash Shabbir[1], Zuhair S Khan* **(To be submitted)**
3. "Diamond-Like Carbon Film Deposited Via PECVD technique for Antireflection Applications in Photovoltaic." Altamash Shabbir[1], Zuhair S Khan* **(To be submitted)**

Chapter 1: Introduction

Energy performs a crucial role in many aspects of our lives. For example, we need electricity for lighting, heating, ventilation, cooking, preservation, calculation, recreation, etc. Similarly, we use fossil fuels for transportation, power generation, heating, and cooking. Simply, we need energy in one form or the other to help us perform activities with relative ease and comfort.

Environmental pollution and climate change are other major concerns to be associated with energy-related processes. Irrespective of the energy source, energy-related practices are generally not always perfectly hygienic, such as particulate matter, fog, etc. may result because of these practices. However, some effects that could be traced to energy sources can be environmentally more distracting, harmful, and long-lasting than others. In this regard, fossil fuels are the most polluting ones, as a major portion (78.3%) of the energy that we use today comes from these fuels. If we kept on exploiting fossil fuels at the current rate, then by the time fossil fuels become scarce, it would have brought about huge misery upon the inhabitants of the earth. Fossil fuels (whether coal, natural gas, or petroleum) processing and burning cause environmental pollution and climate change. Compounds of heavy metals (like mercury, lead, etc.) are released into the earth's crust, while acid gases (NO_x, SO_x) and greenhouse gases (GHGs) are liberated into the atmosphere. In this way atmospheric CO_2 level is being disturbed. CO_2 is a greenhouse gas (GHG) and contributes to global warming. Global warming is the number one contributor to climate change. Similarly, nuclear energy, though around 2.6% of the global final energy consumption, is also disturbing the environment. Radioactive materials because of nuclear fuel enrichment, or fission keep on contaminating the earth's crust. If such materials make their way to drinking water, then the biosphere gets at huge risk.

1.1 Energy Crisis

The world's population has grown faster than ever in the last century. With the advancement in science, our living standards improved a lot, which ultimately leads to an increase in energy demand. Human being always tends to find easy and economical ways of energy to meet those requirements. In the last 12 decades, human beings relied mostly on fossil fuels, as they were the most economical and easiest to access. Electric

power demand is met mostly by coal power plants and transportation needs are met by crude oil derivatives. But things were not as easy as they were looking [1]. Those fossil fuel reserves are not only depleting but humanity is paying a huge price due to climate changes caused by carbon dioxide emissions.

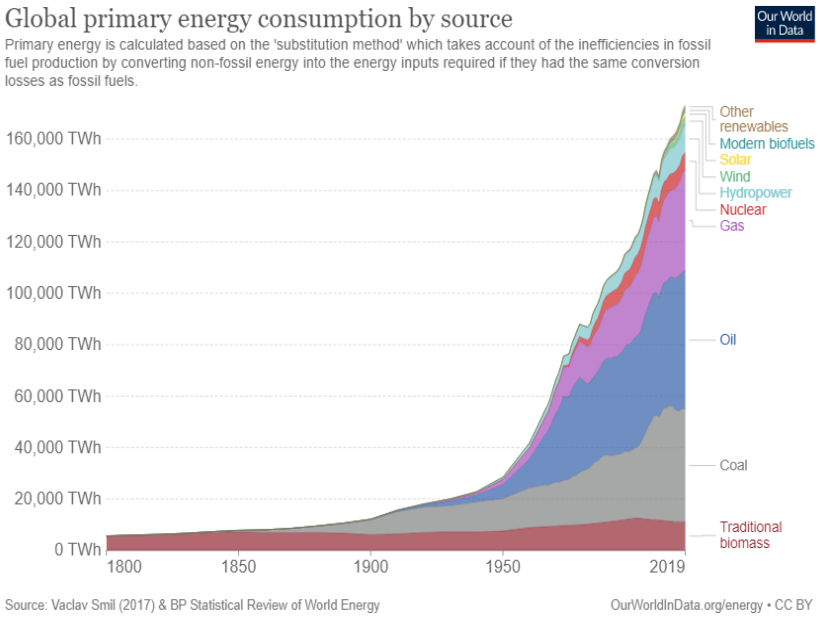

Figure 1-1. Global primary energy consumption by source [2].

These major environmental issues have compelled humanity to find out nature-friendly energy sources. Solar, Wind, Biomass, hydro energy, and fission-based nuclear plants are some of them. But their shorter availability and ever-increasing demand for energy have compelled us to establish the most advanced energy technologies [3].

1.2 Effect of Non-Renewable Energy Resources on Climate

Energy and climate are interrelated. Energy and climatic links energy sector account for nearly two-thirds of all anthropogenic GHG emissions [4]. CO_2 is the main GHG, although CH_4 and N_2O are other potent GHGs from the energy industry. The GWP of CH_4 is 28-30 times that of CO_2, whereas that of N_2O is at least 265 times that of CO_2. Although CH_4 and N_2O have greater GHG effects than CO_2, they get less attention due to their lesser magnitude and shorter atmospheric lifetime.

Fossil fuels provide over 80% of primary energy consumption. These fuels emit emissions into the atmosphere when burned. More than 90% of the carbon dioxide that is related to energy comes from the burning of these fossil fuels. Nearly 10% of energy-

related emissions are CH_4. The remaining half is N_2O, which is produced by energy conversion, industry, transportation, and buildings [4]. This concentration of GHGs is growing. ppm CO_2 concentration now. For example, in the last 27 years, global energy-related CO_2 emissions have matched all preceding years' CO_2 levels [4].

To mitigate GHGs emissions, the United Nations conducts yearly conferences by the United Nations framework convention on climate change (UNFCCC) treaty. These conferences are the formal meetings of the UNFCCC parties and are commonly known as Conferences of the Parties (COP). COP is meant to assess the yearly progress in dealing with climate change. The first in the series was COP1, held in Berlin in 1995. These gases are causing global warming, endangering our loved ones. To avert serious climate change, fossil fuels must be kept in the ground. We are fortunate to see renewables increase, reducing climate change risks while enhancing the economy, improving human health, and generating new employment possibilities. The UN holds annual conferences to reduce GHG emissions in compliance with the UNFCCC treaty.

These conferences are known as Conferences of the Parties and are official gatherings of UNFCCC parties (COP). The COP is supposed to evaluate annual climate change progress. COP1 was held in Berlin in 1995. In 2005, the pact took effect. 2008-2012 was its first promised period The treaty required developed nations to reduce GHG emissions by 5.2 percent since 1990. During the 5 years, the target was to decrease the overall emissions of six key GHGs: CO_2, CH_4, N_2O, HFCs, PFCs, and SF_6 [5].

As the name applies, renewables like solar, wind, geothermal, hydropower, biomass, biofuels, etc. are inexhaustible, yet much more environmentally friendly than fossil or nuclear energy. Except for conventional hydropower, an issue with the renewable energy systems, for the time being, is their high energy output costs. However, through improved scientific and engineering practices, renewables are closing in on the conventional in the price department as well. Let’s hope that shortly renewable energy becomes at least as affordable as the conventional, and then the actual boon period begins.

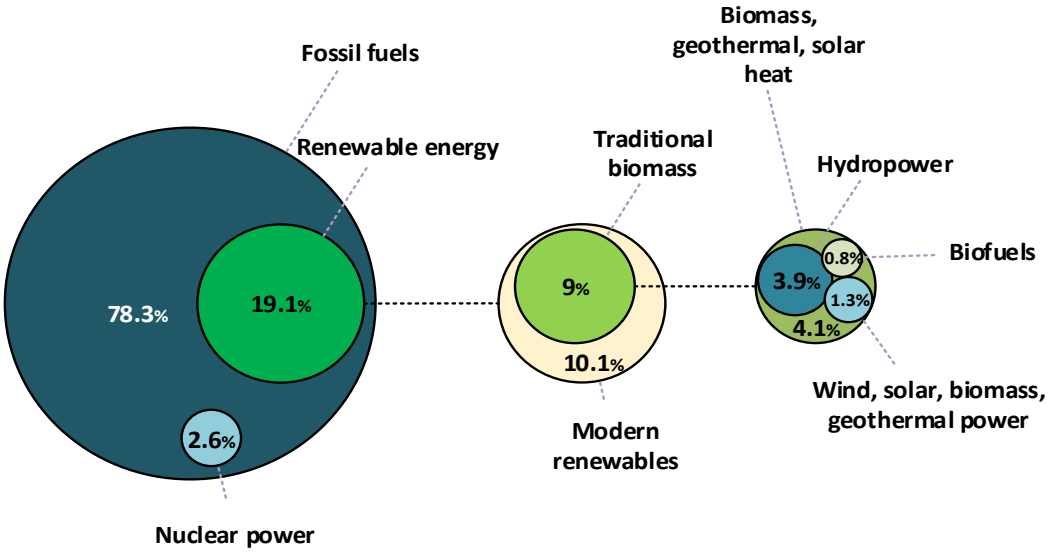

Figure 1-2. Renewable energy share from various sources.

Protocol's first commitment term concluded in 2012, and a second commitment period was agreed to in Doha, Qatar, during COP18. COP18 was the 8th Conference of the Parties to the Kyoto Protocol (CMP8), also known as the Doha Amendment. The Doha Amendment is still not in place as of July 2016, since only 66 states have adopted it. The Kyoto Protocol is still in place, although just 10% of world GHG emissions are predicted by 2020 [4]. On April 22, 2016, 174 nations signed and ratified the accord. Other governments have till April 21, 2017, to sign. The goal was to keep global warming below 2 °C. It calls for zero net man-made GHG emissions in the second part of this century. Parties would also attempt to keep the average temperature rise to 1.5 °C. Some experts say the 1.5 °C target will need zero net GHG emissions by 2030 or 2050 [6]. Many individuals still question climate change. The greenhouse effect was found earlier. Carbon dioxide in our atmosphere continually heats our environment. The majority comes from fossil fuels. The complete heat gained from the sun is usually sent into space in the form of infrared radiation.

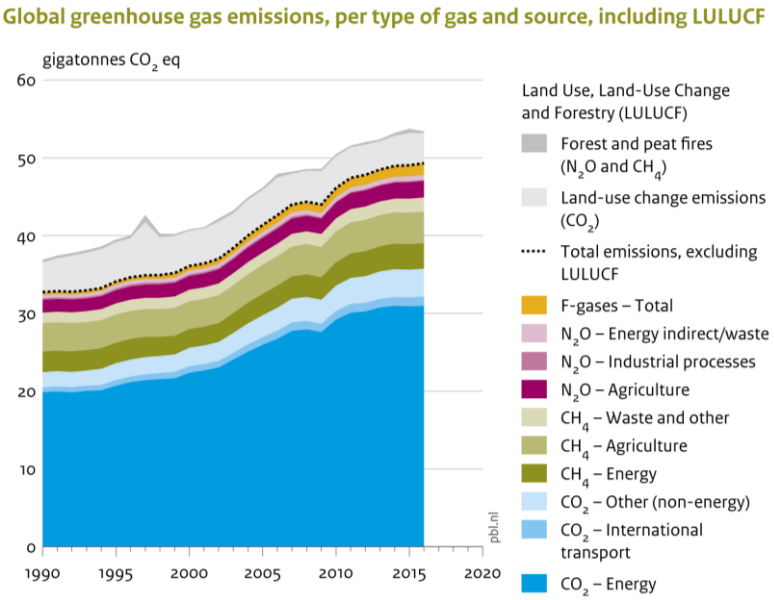

Figure 1-3. Global GHG emissions [7].

However, much carbon dioxide disrupts this equilibrium by entrapping heat. Plants and woodlands absorb most CO_2. This leads to excess CO_2 production. Our current CO_2 concentration is at 407 ppm, which is three times the average CO_2 concentration for the previous 100000 years. They say if we keep producing CO_2 at this pace, the earth will become inhabitable and resemble Venus. In Pakistan, carbon dioxide is responsible for around 60% of greenhouse gas emissions. CO_2 emissions have risen from 30 million tonnes in the 1980s to 170 million tonnes presently. Every year, CO_2 emissions rise by 6–8 % [2].

1.3 Energy shortage in Pakistan

Pakistan always has power and energy shortage problems. The situation was worse a few years back. Most of the power demand in Pakistan is met by coal and fossil fuels in the form of thermal power plants.

Pakistan is one of the top ten countries vulnerable countries that are most affected by climate change, increase in energy demands and depletion in fossil fuel is the major concern that compelled us to start thinking about such kind of energy facilities that can give abundant, sustainable, and environmentally friendly energy. Currently, Pakistan's energy mix from fossil fuels and hydrocarbons is 86 % (Natural gas 47 %, Oil 33 %, Coal 6 %). Power generated from Fission based nuclear reactor accommodate 2 % of national need. Renewables have a very small portion.

It is well noticeable that Pakistan is not a poor nation as far as accessibility of natural resources yet, it is a nation that falls behind at the administration end. It is shocking to express that about 15% of the population has no access to power. Energy shortfall is presently the reason for numerous different issues the present circumstance requests to fathom not just the energy crises yet in addition to the human advancement which are enormously interlinked.

Advance power generation technologies, for example, hydrogen-based novel assets for Fusion reactors are one of the answers for these musings. In this system, Pakistan has officially settled the Nation Tokamak Program which requires a great deal of devoted work to make it ready to begin vitality creation in the not-so-distant future and this examination is a step towards the goal [7].

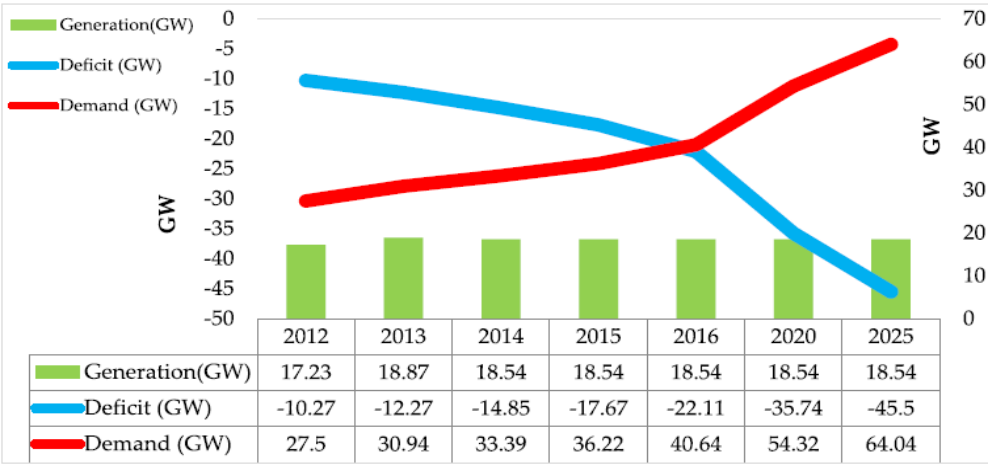

	2012	2013	2014	2015	2016	2020	2025
Generation(GW)	17.23	18.87	18.54	18.54	18.54	18.54	18.54
Deficit (GW)	-10.27	-12.27	-14.85	-17.67	-22.11	-35.74	-45.5
Demand (GW)	27.5	30.94	33.39	36.22	40.64	54.32	64.04

Figure 1-4. Pakistan's Energy Generation, Deficit, and Demand [8].

1.4 Solution of Problem

Pakistan is under a major electricity crisis. Per capita, Pakistan uses three times less electricity than the globe. This issue must be resolved quickly since industrial development and GDP are closely tied to electricity usage. We need to establish electricity sources that can give a long-term answer. They must be both cost-effective and eco-friendly. Pakistan is taking good progress. Every year, renewable energy grows in share. Nuclear energy contributes roughly 1300 MW to the national grid. Pakistan plans to double its nuclear power capacity by 2025. In Pakistan, several departments have been set up to perform energy research and development. These departments include AEDB (Alternative Energy Development Board) and PCRET (Pakistan Council of Renewable Energy). These institutions exist to do energy research and train

personnel. Pakistan must use all available electricity sources. All conventional and renewable energy sources must be combined. Pakistan now has over 25000 MW installed. Our demand ranges from 17000 to 23000 MW and is predicted to double by 2050 [9].

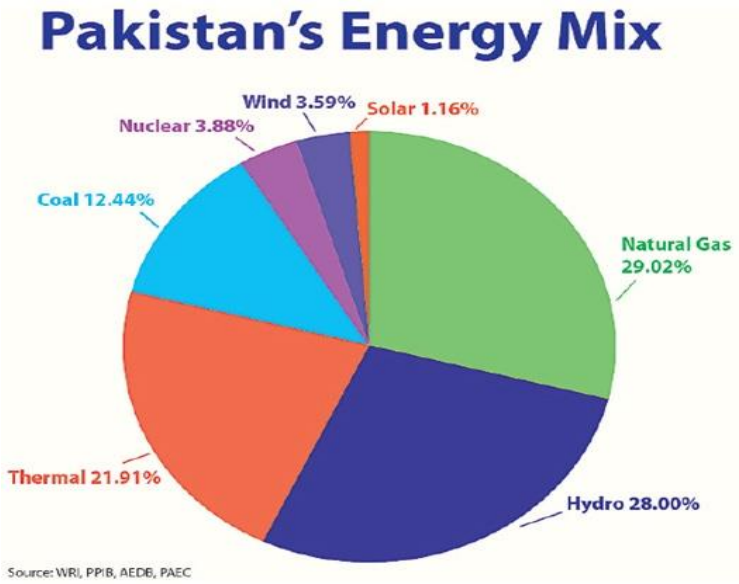

Figure 1-5. Energy Mix of Pakistan by Sector [8].

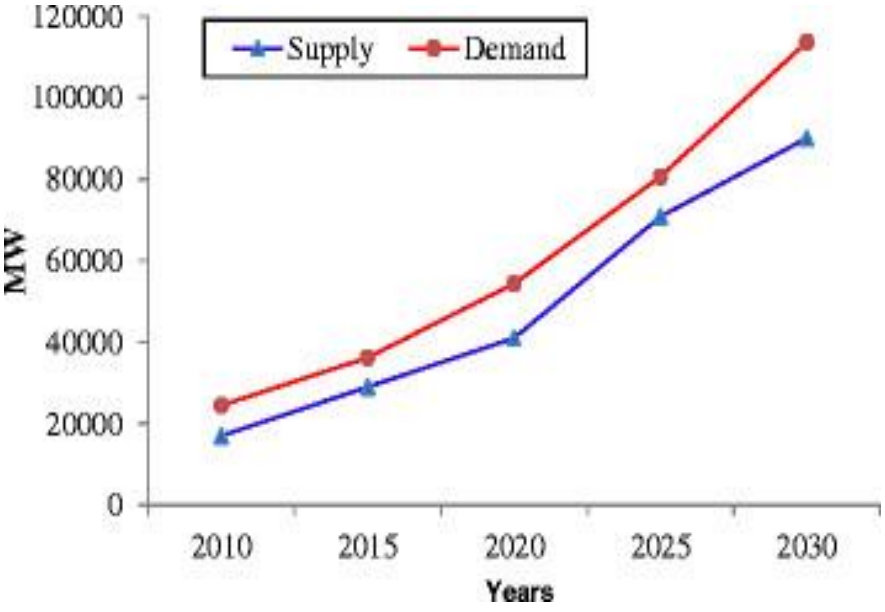

Figure 1-6. Energy Demand and Supply of Pakistan [4].

1.5 Need for Renewable Energy

All human activities influence our environment. Energy from renewable sources is not exempt from this restriction. The benefits of renewable energy over fossil fuels are undeniable: less water and land consumption, less air and water pollution, less wildlife and habitat loss, and no or reduced carbon emissions. Their local and decentralized nature, as well as technological advancement, assist the economy and individuals. Renewable energy produces no or little CO_2. Fossil fuel burning produces considerable greenhouse gas emissions that contribute to global warming. Although most renewable energy sources produce little to no emissions during their entire life cycle, some do. Renewable energy generates little pollution. Global growth in fossil fuel-based vehicle travel, industrial activity, electricity production, and waste burning lead to increased air pollution. In many underdeveloped nations, heating, and cooking with charcoal and wood add to poor indoor air quality. Fossil fuel pollution practically asphyxiates towns. The World Health Organization says their presence causes millions of premature deaths and costs billions. Renewable energy is cheap. Energy costs and resource scarcity are typically linked to geopolitical unrest. Weaker geopolitical conflicts, price hikes, and supply chain disruptions due to local production. Biomass creates jobs. Most renewable energy expenses are on materials and labor for construction and operation. Many renewable energy investments are regional, national, or local. The money individuals pay for energy remains local, helping to generate employment and power the economy. Renewable energy bolsters the energy grid. Renewables reduce reliance on faraway sources and grids. To minimize interruptions, businesses and industries invest in renewable energy sources.

1.6 Renewable Energy Resources

Renewable energy is energy that is generated by nature and is derived from the wind, photosynthetic, hydropower, and solar energy stored in biomass. Renewable energy does not contain fossil fuels, fossil waste products, or inorganic waste [10]. Renewable energy systems transform natural energy into electrical, thermal, and fuel energy. In Fig.1-7, renewable energy sources can provide over 3000 times the current global energy consumption [8]. Renewable energy has expanded substantially in the past five years. Traditional technologies like hydro and newer technologies like wind and solar photovoltaic have experienced fast deployment due to greater faith in technology, decreased prices, and new possibilities.

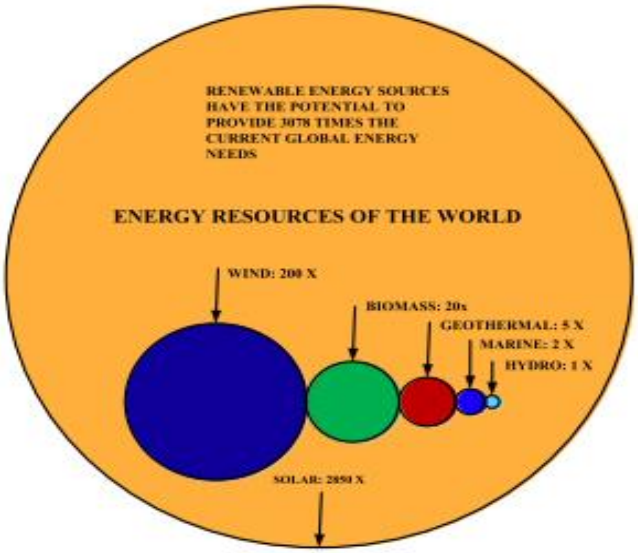

Figure 1-7. Energy resources of the world [9].

Table 1-1 illustrates that worldwide renewable power generation will double between 2010 and 2035. During this time, biofuel use is predicted to triple, reaching 4.5 million mboe/d in 2020. Transportation uses almost all biofuels; however, aviation biofuels will be used by 2035. The usage of current renewables will nearly triple from 2010 to 2035. On the other hand, as shown in Fig.1-7 [11], renewables are employed more in power generating than in heating. In this post, we will look at renewable energy sources, their current and future condition, their contribution to various applications, and their benefits. Renewable Energies will benefit from power electronics and smart grids.

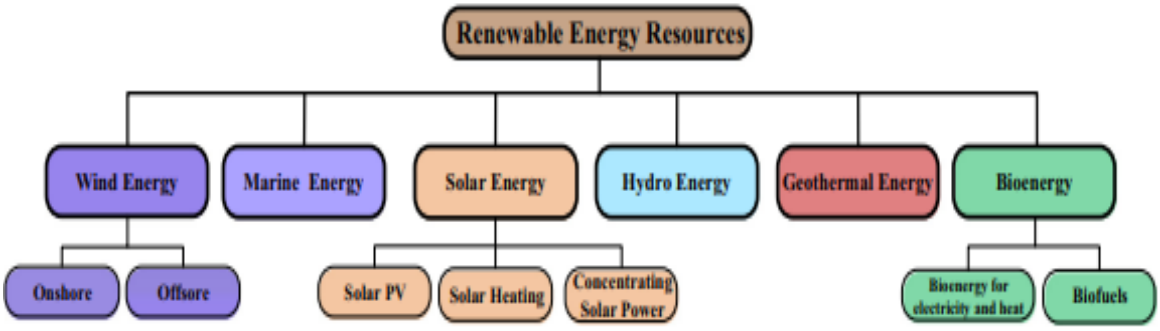

Figure 1-8. Overview of renewable energy sources.

Biomass Energy

The term "biomass" refers to all organic matter generated from plants, trees, and crops. Biomass may be used to generate energy in the form of heat, electricity, and liquid fuels (biofuels). Despite their benefits, biomass-to-energy facilities confront significant

obstacles. Biomass fuels have a low energy density and are inconvenient to collect and transport. While the use of biomass to generate electricity is widespread, the cost of biomass fuel is seldom repaid. Biofuels need a significant number of inputs, including land, water, land, fossil fuels, and crops, all of which have associated opportunity costs.

Geothermal Energy

Geothermal energy is a very efficient and powerful method of obtaining green energy out from the ground. This can be done on a small scale, such as to heat a home, or on a large scale, such as to generate energy via a geothermal power plant. Geothermal energy is a relatively inexpensive, reliable, and environmentally-friendly form of energy. Numerous hot springs (with temperatures over 180 °C) are associated with recent volcanic activity. Under some situations, high-temperature geothermal fields can be exploited directly to create energy or heat.

Hydropower Energy

Hydropower is generated by the energy of flowing water. Aquatic energy is absorbed and turned into electrical energy via turbines. Dams are the most frequent kind of hydropower, while wave and tidal power are becoming increasingly widespread. Water flowing in the hydrological cycle is used to create hydropower. Hydropower plants vary in size from a few watts to many GW. The biggest projects are Itaipu (14,000 MW) in Brazil and Three Gorges (22,400 MW) in China, each generating 80-100 TW h/yr. A river system's hydropower project is always site-specific.

Marine Energy

Ocean thermal energy conversion, tidal range, waves, salinity gradients, and tidal range, are all renewable marine (ocean) energy sources. It can produce 7400 EJ/yr, much beyond current and future human energy needs. Between 2004 and 2009, less than 3 MW of combined wave and tidal current generation capacity was developed annually. Installed capacity is predicted to grow by around 25 MW per year in the USA, UK, and Portugal.

Wind Energy

In short, wind power is the use of wind turbines to turn wind energy into usable forms of energy that can be used for things like electricity, water or drainage pumping, or ship propulsion. In the early 1900s, wind turbines were used to make electricity. Since the early 1970s, technology has changed a lot. One of the most important renewable energy sources came back in the late 1990s when wind energy was one of the most important sources. Wind turbines and power plants that convert the kinetic energy of moving air

into mechanical and electrical energy are hard to build economically. The more wind speed there is, the more kinetic energy there is that can be taken out. Wind turbine design aims to reduce the number of materials used while increasing the size of the turbine, the reliability of its parts, and the efficiency of its operations.

Solar Energy

Solar energy is made by using the sun's power to make hot water or electricity (photovoltaic and concentrating solar power). Many systems have been used around the world in the last few years to show that this technology works. Solar PV systems convert sunlight into electricity right away. The PV cell is a semiconductor device that converts solar energy into electricity that can be used right away or DC. It is made up of PV cells (50-200 W). In recent years, thin-film modules, which can also be made of non-silicon semiconductors, have become more important. Concentrating PV cells can be up to 40% more efficient. There is still a lot of work to do on organic PV cells, for example. Solar PV has two good things. PV is a modular technology, but large-scale module production can save money because it can make a lot of them at once. PV is different from CSP in that it uses both direct and diffuse sunlight to make electricity. This means that even when the sky is cloudy, PV can still make electricity. This power allows for far more global use than CSP.

Table 1-1. Renewable energy Resources.

	2010	**2020**	**2035**
Electricity generation (TWh)	**4206**	**6999**	**11,342**
Bioenergy	331	696	1,487
Hydro	3431	4513	5,677
Wind	342	1272	2,681
Geothermal	68	131	315
Solar PV	32	332	846
Concentrating solar power	2	50	278
Marine	1	5	57
Share of total generation	**20%**	**25%**	**31%**
Heat demand (Mtoe)	**337**	**447**	**604**

Industry	207	263	324
Building and agriculture	131	184	280
Share of total production	10%	12%	14%
Biofuels (mboe/d)	1.3	2.4	4.5
Road transport	1.3	2.4	4.4
Aviation	_	_	0.1
Share of total transport	**2%**	**4%**	**6%**

1.7 Solar Cells Technology

It was in 1839 that Alexandre Edmond Becquerel discovered that some materials created little quantities of electric current when they were exposed to light. Physicist William Grylls Adams, together with his student Richard Evans Day, discovered in 1876 that the element selenium generates electricity when light shines on it. It was because of these findings that PV technology was able to evolve and become commercially viable later. It took more than a century, however, for the notion of solar-generated electrical power to become more than simply a laboratory experiment. Since then, the solar cell industry has grown dramatically [10].

1.7.1 Physics of Photovoltaics

Photovoltaics is the conversion of light energy into electricity at the atomic level. This is a property of some materials that permits them to absorb photons of light and release electrons as a result of the interaction between them. When free electrons are gathered, an electric current is formed, which may be used to generate energy if the current is large enough.

In 1839, French scientist Edmund Becquerel found that some materials created minute amounts of electric current when exposed to light. In 1905, Albert Einstein explained the physics of light and the photoelectric effect, which is the basis of photovoltaic systems.

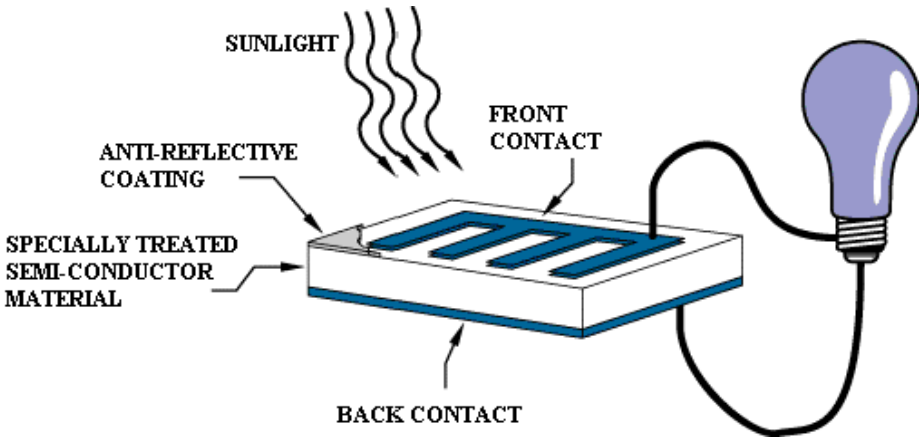

Figure 1-9. Schematic of Photovoltaic effect.

As far back as 1954, Bell Laboratories produced the first solar module. A solar battery was marketed for its low cost, but in reality, it was more of a curiosity than anything else. In the 1960s, the space industry began to rely heavily on technology to power spacecraft. Through space initiatives, technology improved, reliability was established and costs decreased [10]. For non-space applications, photovoltaic technology became prominent during the 1970s energy crisis.

A photovoltaic (or solar) cell is depicted in the image above. Semiconductor materials, such as silicon, are used in solar cells and microelectronics. Solar cells are made from the positive and negative sides of a thin semiconductor wafer. When light energy enters the solar cell, it causes the atoms in the semiconductor material to release electrons. When two conductors of opposite polarity are connected, electrons can be trapped in the form of electricity. A load, such as a lamp or a tool, may then be powered by this energy.

A photovoltaic module is a collection of solar cells that are mounted on a support frame. They are intended to deliver a certain voltage, for example, 12 volts. The quantity of light that strikes the module dictates the amount of current that is produced. Multiple modules can be connected to form arrays, with bigger modules and arrays generating greater power. PV modules and arrays create direct current electricity. It is possible to create any voltage or current combination wanted by connecting two or more devices in series or parallel. Most of the current PV devices generate an electric field within a semiconductor by utilizing a single junction, also known as an interface. In a single-junction PV cell, the only photons that may cause an electron to be released are those that have an energy equal to or greater than the band gap of the cell. Consequently, less

energetic photons are not used because their energy falls below the band gap of the absorbing material. Using many cells with a variety of band gaps and junctions may be beneficial in overcoming this problem. Multijunction cells (MJCs) are a kind of cell that has many junctions (also called "cascade" or "tandem" cells). As a result, the total conversion efficiency of multijunction devices improves. Each single-junction cell is stacked in descending order of band gap size for maximum density (Eg). Take advantage of high-energy photons and transmit the rest to cells with a smaller band-gap for absorption.

Parameters effect on PV performance

Weather, equipment, and system configuration all have an impact on the performance of solar systems. The relationship between actual solar PV system production and expected values is crucial for the efficient management and maintenance of solar PV facilities. The global light irradiance of a solar array, which is a combination of direct and diffuse radiation, is the primary energy source for the array.

PV monitoring systems evaluate performance and typically include a weather station to provide additional data (device utilized on sites or an independent source of weather data). When used in conjunction with a photovoltaic performance monitoring system, it can track trends in a single PV system, identify flaws or damage to solar panels and inverters, and compare system performance to design specifications. It can also compare PV systems at different locations.

Sensors and monitoring systems that are tailored to the specific needs of each application are required. PV facility output expectations must be standardized using both electronic monitoring sensors and independent weather sensing (irradiance, temperature, and other variables). The PV industry is primarily reliant on irradiance sensing, which may be classified into two categories. The third option to onsite pyranometers is regional weather stations driven by the Industrial Internet of Things (IIoT), which provides lower data quality. The Industrial IoT-powered sensor-less measurement approach has just developed as a third alternative. [12].

1.8 Generations of Photovoltaics

Photovoltaic technologies are currently divided into three basic categories, which are referred to as generations of solar cells. Solar cells are available in three generations: the first, second, and third.

1.8.1 First Generation of Solar Cells

These cells are typically constructed from silicon wafers. These solar cells are sometimes referred to as crystalline silicon (c-Si) solar cells. Solar cells are classified into two types: monocrystalline Si (mono-Si) and polycrystalline Si (multi-Si). In the lab, a cell efficiency of 25.6 percent has already been achieved, and modules are working at a rate of 15 - 20% of their theoretical capacity. These solar cells, which are commonly found on roofs, account for most of the market share in photovoltaics. Most solar panels sold throughout the world use silicon technology, which accounts for more than 80% of total sales. The great efficiency and stability of the technology are two of its most important characteristics. These cells, on the other hand, need a lot of energy to manufacture, are inflexible, and are less stable in extreme settings, such as space [6].

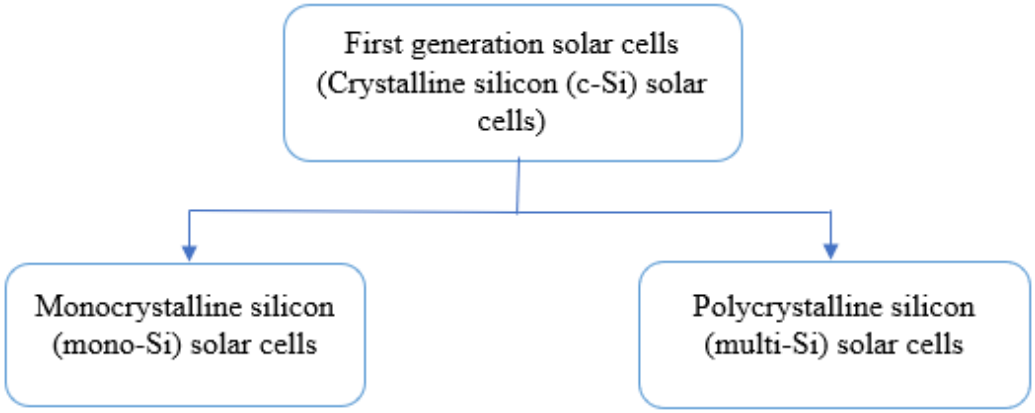

Figure 1-10. First-generation solar cells.

1.8.2 Second Generation Solar Cells

Thin-film solar cells, which are used in second-generation solar cells, are commonly referred to as thin-film solar cells. The cells were given this name because, as compared to first-generation solar cells, they are constructed from extremely thin layers of semiconductors, thus the moniker. The layers are typically only a few micrometers thick in the majority of situations. Second-generation cells that have been successfully commercialized include devices made of materials such as CIGS, amorphous silicon, and CdTe. When it comes to marketed cells, module efficiencies in the region of 10-15 percent are relatively unusual for these sorts of cells. The technologies of copper indium diselenide (CIS) and thin film polycrystalline silicon (TFPS) photovoltaics (PV) are also commercially viable. Thin-film monocrystalline Si solar cell technology has just lately been made commercially available to the public. Another category of thin film devices that has sparked significant research interest is those based on copper zinc tin

sulfide/selenide (CZTS) systems. Unlike CIGS, which utilizes indium that is pricey, or CdTe, which uses tellurium that is restricted in supply, and cadmium that is hazardous, the CZTS system makes use of elements that are abundant on the planet and are non-toxic. The second generation of solar cells is explained in the figure by discussing the types of cells that are used in this technology.[6].

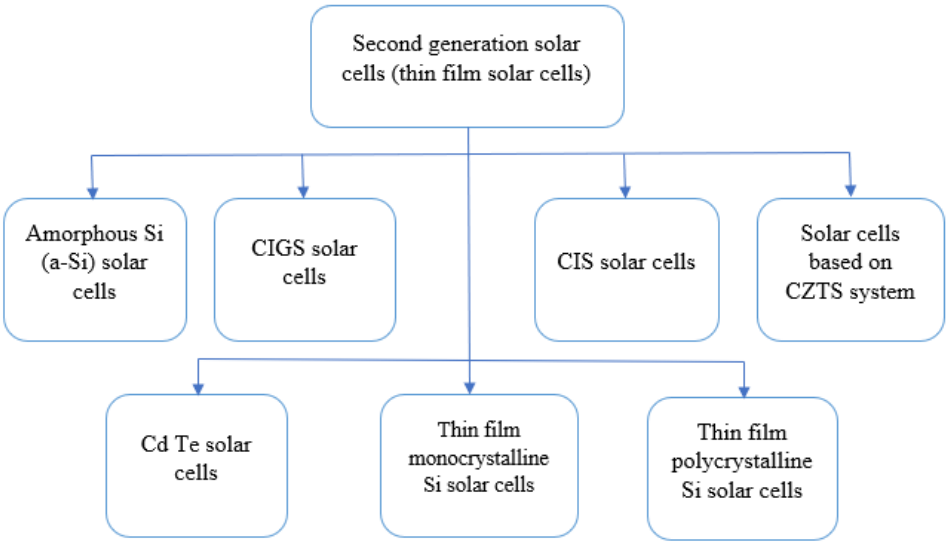

Figure 1-11. The second generation of solar cells.

The technology is famous for its overall lower costs than first-generation solar cells. Lower prices result mainly as a result of less material consumption in these cells than first-generation cells. Mechanical flexibility of modules is another attractive feature of this technology. However, the technology uses high vacuum, inert atmosphere, and high-temperature treatments (in many cases) for processing, making the fabrication process energy-intensive and requiring expensive processing tools, thus incrementing the overall prices of these cells. Solution-based processes for thin film deposition, which are less energy-intensive and don't necessarily require very expensive tools, are currently being researched [12, 13].

1.8.3 Third Generation Solar Cells

The previous two generations mentioned had their benefits due to which they exist till today, however, there are fundamental limitations with either of the two, due to which the PV industry has not been able to extend to its full potential. Post-2020, photovoltaics, as a hugely profitable industry, will be under immense pressure for improved performance. Improved performance would mean a reduced price per watt of electricity generation. Third-generation approaches aim to reduce costs to

$0.50/watt, potentially to $0.20/watt or even lower, primarily by increasing efficiencies and yet maintaining the environmental friendliness and robustness of these modules [14, 15].

The capital cost of a PV system may be separated into two categories: PV module cost and balance of system (BOS) cost. PV module cost is the cost of the solar panels themselves. The cost of a module is determined by the raw material costs, the cost of cell manufacturing/processing, and the cost of module assembly. The cost of things such as the structural system, the electrical system, and the storage system are included in the total cost of the system balance (if storage is required).

Materials cost of the total cost of a cell varies from technology to technology. Irrespective of the technology used, lower material consumption certainly reduces the overall cost per watt of electricity generated. This means we must search for easily available materials, yet we shall be using the least amount of material possible in developing modules. Furthermore, if processing costs are reduced by adopting low-cost processing routes, the overall cost per watt of electricity generated can further be reduced. This implies that the cost of each process step needs to be carefully examined and thus reduced where possible. Improving efficiency further leverages a reduction in costs because the smaller area required per watt also reduces balance-of-systems costs.

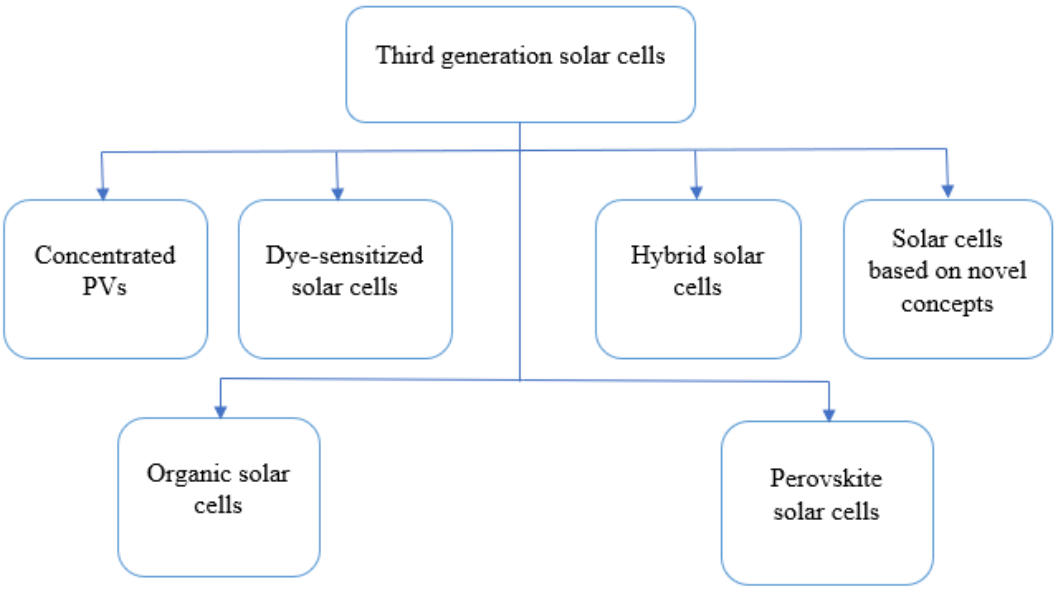

Figure 1-12. The third generation of solar cells.

The next-generation idea relies on various underlying concepts to go as close to the Carnot limit of 95% efficiency as possible, and hence achieve the aforementioned objectives. Nanotechnology lies at the heart of these approaches. The approaches may mainly be related to effects/processes such as 1) multiple energy threshold processes 2) multiple electron-hole pair generation per incident photon 3) hot carrier effects 4) solar thermal electric systems 5) thermionic conversion to electricity 6) thermoelectric power generation 7) thermophotovoltaics and 8) thermophotonics.

Progress in molecular electronics and nanostructure engineering in general, suggested material systems comparable to Si, when it comes to cost, abundance, and non-toxicity. Many such photoactive materials such as conductive polymers or perovskites are solution processable. Further materials research needs to be conducted to have materials of performance and stability comparable or even superior to Si. Current research in this generation of PVs has resulted in several new solar cells such as Concentrating PVs (CPVs), Dye-sensitized solar cells (DSSCs), Organic solar cells (OSCs), Hybrid solar cells, Perovskite solar cells and solar cells based on the novel and emerging concepts (such as quantum dots/wires/wells and super lattice technologies). The diagram in the figure elaborates on these different types of third-generation solar cells. The technology is mainly under the research and demonstration phase; however,

the technology shows great promise, and commercial production of some third-generation solar cells such as organic solar cells has already been started.

1.9 Components of Photovoltaics

Photovoltaic (PV) panels are made of solar cells that are connected. Every solar cell can generate power. A solar module is constructed by joining a large number of solar cells together. PV systems range in size from small rooftop or building-integrated systems generating tens of kilowatts to enormous utility-based stations generating hundreds of megawatts, depending on the application. PV systems may be divided into two categories: grid-connected (grid-direct or grid-hybrid) and off-grid (or stand-alone).

Solar cells generate direct current electricity by converting light (photons) into electrons. DC energy must be converted to alternating current (AC) to power a home or business (alternating current). The electrical system makes use of alternating current (AC) to carry electricity across long distances. Some household appliances run on alternating current (AC), while others run on direct current (DC). At the end user's discretion, AC power can be converted back to DC if necessary.

Modern PV systems are modular, allowing users to add or remove power capacity own will. Consumption may be adjusted using these methods. Other components of photovoltaic systems are Inverters, batteries, and chargers are examples of mechanical mounting components. A solar system's cost can be as much as half if these components aren't reliable. Typical photovoltaic components are as follows [19].

- Output power lines Power inverter (converts DC electricity to AC electricity)
- Charge controller
- Mechanical mounting equipment
- Wiring Batteries for energy storage
- Power processing equipment
- Electrical meter (for grid-connected systems)
- Grounding equipment

Modern photovoltaic systems are also utilized to generate power. Axis tilting systems with automated cooling and cleaning. Makes a hybrid system with solar photovoltaic for energy storage.

1.10 Importance of Antireflection coating in Photovoltaics

AR coatings reduce reflection and increase light absorption by solar cells. Over 30% surface reflectance in silicon. Texturing and ARC reduce reflection. Solar cells have anti-reflection coatings similar to camera lenses. As a result of interfering with the wave reflected off the semiconductor surfaces, the coating's top surface is out of phase. As a result of this, there is no net reflected energy. When a thin coating of oil over water generates rainbow-like color bands [16].

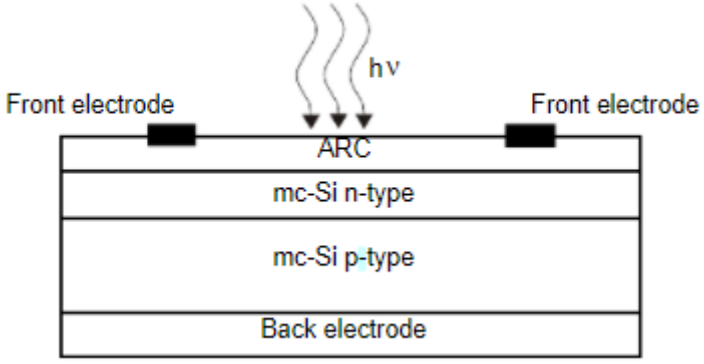

Figure 1-13. Schematic of silicon solar cell.

Anti-reflective solar cells help to increase the amount of light that is absorbed or transmitted. Because bare silicon solar cells reflect around 30% of the light they receive, an anti-reflective coating is required. The AR Coating is comprised of either silicon nitride or titanium oxide, depending on the application. Upon removal of the anti-reflection coating, the cells turn a dark grey colour. The thickness of the anti-reflection coating can influence the colour of the solar cell. Anti-reflection coatings for solar cells are similar to those used on camera lenses in terms of effectiveness.

Anti-reflective coatings are now available for solar cells as well as the glass surfaces of solar panels, making them more efficient. Reflective coatings on solar panel glass enhance light transmission, hence increasing the efficiency of the PV module.

1.10.1 Materials for Antireflection coating

The basic purpose of an antireflective coating is to reduce Fresnel reflection loss and help the light to propagate through PV bulk materials with the highest feasible light transmission. The material utilized to make ARC, the structure of ARC (especially the top surface), and the fabrication techniques used to produce an AR coating are all factors that influence the coating's efficacy. Materials, for example, have an important

role in determining qualities such as transparency, weight, corrosion, chemical, and thermal inertness. Furthermore, the manufacturing process is largely dependent on material qualities and has an impact on the cost factor. The AR coating materials are categorized and evaluated in this part, along with their varied structures, preparation processes, high transmission, and other characteristics. The research potential for each reported study is also listed in tables beneath each area [17]. The following is a list of ARC material classifications:

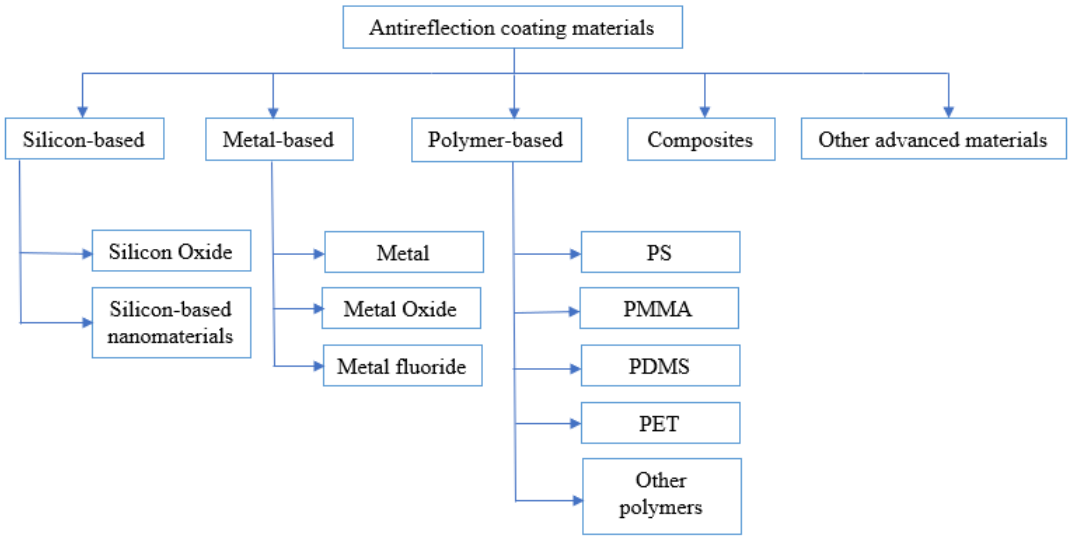

Figure 1-14. Classification of Antireflection coatings.

Silicon-Based Antireflection Coating

Porous silicon (PSi) and silicon nanowires have been widely studied as antireflection coatings (SiNWs). Its compatibility with Si solar cells and utilization in the photovoltaic sector make it required despite undesired reflection losses (reflectivity > 30%). For PV cells, a light-trapping silicon surface structure is necessary due to its high refraction index (nsi > 3.4). Over the last decade, researchers have made tremendous progress in fabricating an efficient antireflection coating using Silicon [17].

Metal-Based Antireflection Coating

When it comes to optical applications, thin metal films have been widely researched and used. Because metal surfaces are flat and highly reflective, they both reduce transmittance and absorption of light over the surface of the substrate. Reduces light reflection by texturing the metal surface with appropriate structures and enhances light transmission into the solar cell because of texturing the metal surface with appropriate structures. For example, a flexible nanostructured gold thin film that is both light-

absorbing and antireflective. A nano-cone array of gold vapor is formed and deposited. The height and periodicity of the nanostructured cone array may be varied by varying the diameter of the beads and the length of time the array is etched. Throughout the 450–950 nm spectral range with an incidence angle of 0-70^{o}, this customized thin film exhibits a reflectance of less than 1%, indicating that it is highly reflective. In this case, the result is owing to the combination of plasmonic absorption and diffractive scattering loss. Thin gold sheets in the shape of nano-cones may be formed using this technology. [18]. Plasma etching colloidal bilayers can create nanopyramids, nanocaps, and nanocavities. To reduce reflection loss and boost light propagation into a substance, metallic Nano level films have recently been found to be effective. To enhance light transmission, structures on metallic materials must utilize metal nanoparticles of proper shape and size.

Polymer-Based Antireflection Coating

Polymer films as ARCs have been more popular in recent years for reducing reflection loss between air and substrate. Polymers offer several advantages over other materials, including great mechanical strength, ease of construction, excellent optical qualities, light weight, chemical and heat resistance, and most importantly, low cost of manufacture. These nanopatterned antireflective polymer films have been shown to improve light transmission in PS, PMMA, PDMS, PET, polyimide, and ETPTA. Many nanopatterning techniques, including as microinjection, plasma etching, and soft imprint lithography compression molding, may readily create nano-polymer films.

Composites Based Antireflection Coating

ARCs must be stacked to achieve minimum reflection over a broad wavelength range. Researchers have created numerous material combinations to enhance antireflective coatings. Similarly, a bilayer of SiO_2 and TiO_2 film was described in the literature with good antireflective and self-cleaning properties. The TiO_2 layer improves self-cleaning, while the low-refractive-index SiO_2 layer works as an AR coating. DLARC had a maximum transmittance of 96.7 percent at normal incidence. We used sol-gel to cover silicon solar cells with Single layer ARC, Double layer ARC, and Triple layer ARC coatings. In the 400–1000 nm wavelength range, SLARC, DLARC, and TLARC coatings had average reflectance of 9.3%, 6.23%, and 3.23%. The PCE of monocrystalline silicon cells was also improved by 39%, suggesting the promise of

low-cost sol-gel-produced ARC [19]. These films have high thermal stability, chemical resistance, photocatalytic activity, and are non-toxic. A sol-gel produced double-layer TiO_2-SiO_2 broadband ARC. The RI may be controlled from 1.19 to 1.45 by adjusting the TiO_2 incorporation into the SiO_2 nanopore layer. In the visible and near-IR area, the double-layer coating had the $T_{max.}$ (98.4%) and $T_{avg.}$ (97.7%). To refine ARC refractive indices, this work takes a different approach than usual. Another study created an ARC using microwave-assisted reactive magnetron sputtering to deposit five TiO_2 and SiO_2 thin films. The photocatalytic effect is achieved by depositing a thin TiO2 layer with a WCA larger than 90^o. In the intended wavelength range, ARC had a transmittance of over 97 percent. Preparation of a scratch-resistant coating combining hydrophobicity and photocatalytic activity.

Other Advanced Materials for Antireflection Coating

Several researchers have worked on this point, so, graphene or diamond-like carbon film has enormous promise in that relevant business. Hexagonal carbon ring with homogeneous honeycomb crystal lattice structure. Fullerene (zero dimension) is an allotrope of carbon made from graphene. CNTs may be made by rolling the graphene sheet or piled on top of each other to generate a three-dimensional graphite structure. It is also being studied intensively as an electrode material for PV devices [20]. These materials are used in PV devices as active components in solar cells. Recently, an ultrathin graphene layer was created via layer stacking and nanotexturing metal nanopatterns. This graphene layer has excellent optical absorption capabilities from the mid-infrared to the ultraviolet, with a 99.9 % light absorption efficiency. Graphene-based Schottky junction solar cells with an ARC on Si substrate for improved performance. The manufactured cell has a PCE of 12.5 %. Graphene is employed as transparent conductive electrodes in a silicon QDs solar cell. The graphene layer is doped with $AuCl_3$ and silver nanowires. This layer also reduces reflections, resulting in a 16.2 % maximum power conversion efficiency.

1.11 Flow Chart for Research Work

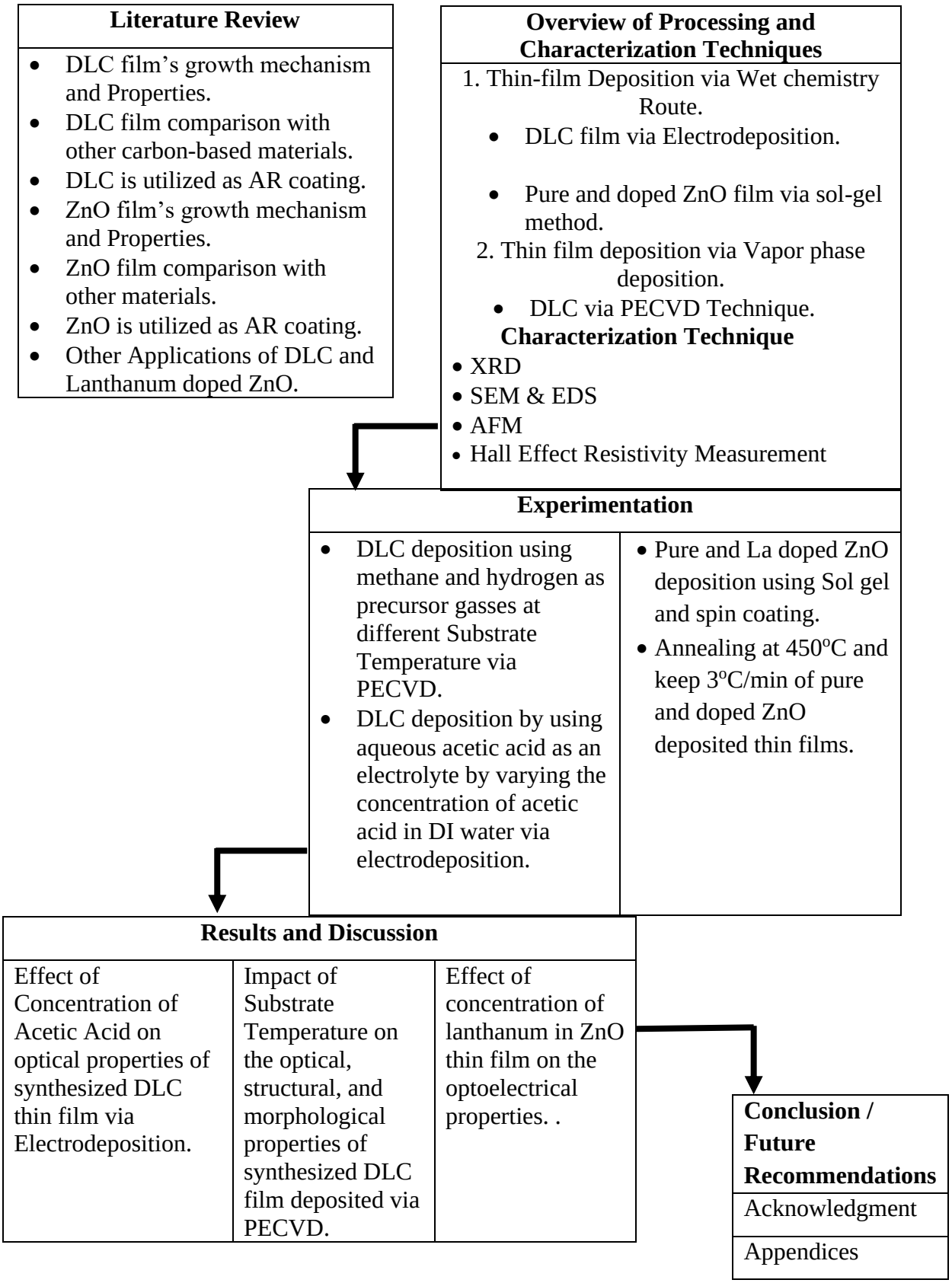

Summary

Concerns with meeting the energy demand are threesome, i.e., sustainability, environment friendliness, and financial viability. Fossil fuel reserves are going to deplete at some point in the future, but not without causing environmental pollution and global warming. We have to fulfill our energy needs as well as the pledges to safeguard the environment. Renewables seem attractive in this perspective. Out of renewables, solar PV is the fastest growing technology. It is renewable, and environment friendly, however, cost prohibitive relative to fossils. The big challenge with solar PV, for the time being, is to reduce its per-unit cost to compete with fossils. Efforts are underway to bring down the per-unit cost by adopting new technologies, new and cheap materials, and novel and cheap processes to make solar PV more affordable. Since the discovery of the photovoltaic effect and then the invention of the first solar cell, PV technology has evolved tremendously and has resulted in the emergence of three solar cell generations thus far. On a silicon wafer, more than 30-35 % of the light is reflected. Reflectivity on the surface of the silicon solar cell is an issue nowadays. Most of the solar radiation is reflected over the surface of the solar cell which can reduce the efficiency of the solar module. So, Antireflection coating is one of the most fascinating components in the solar cell that can reduce the reflection and help to capture the light. There are several numbers of coating based on silicon, metal, composites, and polymers. In metal-based ZnO thin films are used as an antireflection coating to improve the efficiency of the solar cell. Carbon-based films are also improved the capturing ability of light over the surface of the solar module.

References

1. Rehman, A., et al., *The effect of carbon dioxide emission and the consumption of electrical energy, fossil fuel energy, and renewable energy, on economic performance: evidence from Pakistan.* 2019. **26**(21): p. 21760-21773.
2. Ahmad, N., et al., *Modelling the CO2 emissions and economic growth in Croatia: is there any environmental Kuznets curve?* 2017. **123**: p. 164-172.
3. Wang, Z., B. Zhang, and B.J.J.o.c.p. Wang, *Renewable energy consumption, economic growth and human development index in Pakistan: evidence form simultaneous equation model.* 2018. **184**: p. 1081-1090.
4. REN, R.J.R.e.p.n.f.t.s.c.P., France: REN21 Secretariat, *Global status report.* 2015.
5. Facts, S.J.M.a.U.t.a., disadvantages of different solar cells and w.t.m.l. are, *Advice.(2013).* 2015.
6. Tarrant, D. and R. Gay, *Commercialization of CIS-based thin-film PV: Phase 1 annual technical status report, August 1998--August 1999*. 2000, National Renewable Energy Lab., Golden, CO (US).
7. Maqbool, R. and Y.J.J.o.c.p. Sudong, *Critical success factors for renewable energy projects; empirical evidence from Pakistan.* 2018. **195**: p. 991-1002.
8. Khan, J., M.H.J.R. Arsalan, and S.E. Reviews, *Solar power technologies for sustainable electricity generation–A review.* 2016. **55**: p. 414-425.
9. Sheikh, M.A.J.R. and S.E. Reviews, *Energy and renewable energy scenario of Pakistan.* 2010. **14**(1): p. 354-363.
10. Kruskopf, M., et al., *Comeback of epitaxial graphene for electronics: large-area growth of bilayer-free graphene on SiC.* 2016. **3**(4): p. 041002.
11. Timilsina, G.R., et al., *Solar energy: Markets, economics and policies.* 2012. **16**(1): p. 449-465.
12. Conibeer, G.J.M.t., *Third-generation photovoltaics.* 2007. **10**(11): p. 42-50.
13. Yang, Y., et al., *A general water-based precursor solution approach to deposit earth abundant Cu2ZnSn (S, Se) 4 thin film solar cells.* 2016. **313**: p. 15-20.
14. Candelise, C., et al., *Materials availability for thin film (TF) PV technologies development: a real concern?* 2011. **15**(9): p. 4972-4981.
15. Raheem, A., et al., *Renewable energy deployment to combat energy crisis in Pakistan.* 2016. **6**(1): p. 1-13.
16. Farah, H. *The Case of Geothermal Energy from Productive, Depleted and Abandoned Oil and Gas Wells*. in *Proceedings, 42nd Workshop on Geothermal Reservoir Engineering*. 2017.
17. Chen, D.J.S.E.M. and S. Cells, *Anti-reflection (AR) coatings made by sol–gel processes: a review.* 2001. **68**(3-4): p. 313-336.
18. Dey, T., D.J.J.o.S.-G.S. Naughton, and Technology, *Cleaning and anti-reflective (AR) hydrophobic coating of glass surface: a review from materials science perspective.* 2016. **77**(1): p. 1-27.
19. LI, S., et al., *Design and Fabrication of Visible and Infrared Dual-band AR Coating.* 2014: p. 07.
20. Sood, A.K., et al. *Development of nanostructured antireflection coating technology for IR band for improved detector performance*. in *Sensors, Systems, and Next-Generation Satellites XXV*. 2021. SPIE.

Chapter 2: Literature Review on DLC and ZnO as an anti-reflection coating for PV

2.1 Diamond-like Carbon

Nanomaterials have a vital role in the development of the material science & engineering field either those taken to perfections in mechanical engineering, quantum, and electronics computing, bioengineering, or other disciplines. One of the most important parameters or fascinating things about nanotechnology is that the characteristic of material can behave differently when the size or the dimension of the material reaches nanometers. The coating is one of the best methods to enhance the radiation resistance and boost the thermal and optical characteristics of the system [1, 2]. Several coatings like SiO_2, MgF_2, ZnO, Si_3N_4, and SiN: H are used as an antireflection and serve a protective purpose for solar cells. Kotsay et al. have shown that IR optical coatings based on conventional fluoride such as BaF_2, PbF_2, ThF_4 have poor mechanical and adhesive strength [3]. The wear resistance of DLC coating is better in comparison with the conventional anti-reflection coating. These days DLC films are employed as a protective layer as well as antireflection, especially for silicone solar cells. DLC is a class of carbonaceous material, consists of hydrocarbon that are bonded by sp^2 and sp^3 hybridization or electronic configurations.

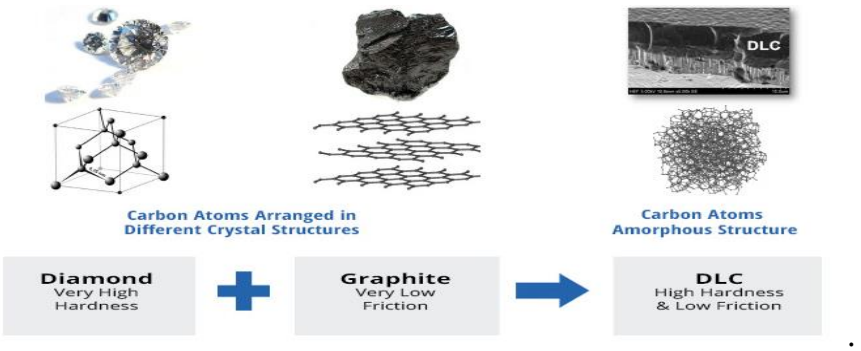

Figure 2-1. Schematic of Diamond-like carbon material [4].

C-H denotes hydrogen-containing films, which must be deposited using hydrocarbon precursors, whereas C- denotes non-hydrogen-containing films. Unlike rough diamond films, At ambient temperatures, smooth and confined DLC coatings may be deposited

across large areas of the surface [5]. DLC films may be made utilizing a range of carbon-containing solid or gaseous source sources, including DC or RF plasma-assisted CVD, ion beam deposition, and sputtering [6]. DLC's characteristics are intermediate between diamond, graphite, and hydrocarbon polymers.

Solar cells have surface reflection which reduces their efficiency. This reflection may reduce by applying antireflection coating (ARC) on the solar cell by using the texturing method. Alkali texturing has a great advantage for the multi-crystalline silicon because anisotropic etching cannot homogenously texturize multi-crystalline silicon which is the basic stuff for the fabrication of the solar cell. The acidic solution is the key method to texturize the multi-crystalline silicon surface by producing a thin, porous silicon layer on the SC's surface. The DLC porous silicon layer or coating is utilized to decrease the reflection from the solar cell surface and improve the conversion factor of the solar cell. One of the major issues regarding porous silicon is, its characteristic to oxidize decreasing its capacity of antireflection. The conversion efficiency of the solar cell may increase by introducing the aluminum (Al) and phosphorous (P) gettering in the solar cell manufacturing process [7].

2.1.1 Types of DLC film

There are several types of DLC films that we can deposit on the different substrates. Some of the materials are mentioned below [8, 9].

i) Amorphous Carbon (a-C)

In this category, the film shows the presence of sp^2 bonds predominates, with hydrogen content typically less than one percent.

ii) Hydrogenated Amorphous Carbon (a-C: H)

In this category, films have a wide range of properties due to varying amounts of sp^3/sp^2 bonds and hydrogen content.

iii) Tetrahedral Amorphous Carbon (ta-C)

Ta-C has the highest percentage of sp3 bonds; it is typically synthesized from solid graphite but does not contain a lot of hydrogen.

iv) Hydrogenated tetrahedral Amorphous Carbon (ta-C:H)

Tetrahedral amorphous carbon (a-C: H) with a hydrogen content of approximately 30% and a variable fraction of sp^3/sp^2 bonds (typically around 30% hydrogen content).

2.1.2 General View on Properties of Diamond-like Carbon Film

In most cases, sp^3 and sp^2 bonds are found in DLC thin films. Hydrogen is the third constituent. Using the film structure as the basis, Figure 2.2 shows the ternary diagram composition. Amorphous carbon films with diamond-like characteristics are formed when the sp^3 concentration is increased, and the film characteristics become more diamond-like. In terms of mechanical properties, sp^2 is graphitic.

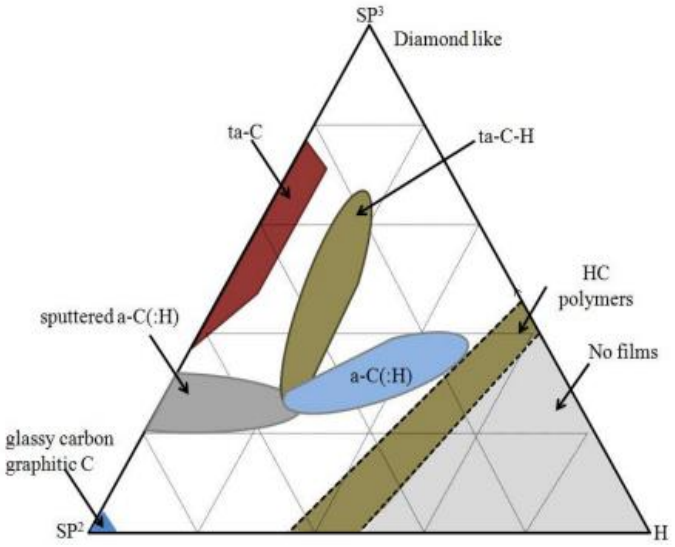

Figure 2-2. sp^2, sp^3, and hydrogen contents of various DLC films [10].

The world's hardest substance is diamond. It possesses exceptional hardness values and a low coefficient of friction, making it more wear-resistant than other known hard thin films. Table 2.1 compares diamond, ta-C, a-C: H, and graphite.

2.1.3 Growth Mechanisms and Structural Analysis on Hydrogenated Amorphous Diamond-Like Carbon

Diamond is recognized as a carbon allotrope, which means that it is made up of carbon atoms linked together by covalent bonds in a certain arrangement. With its ability to create short, medium, and long-range combinations with both itself and other elements, carbon stands out as a particularly useful and interesting element. The nucleus of a single carbon atom is surrounded by six electrons. This shape is known as the C-ground atom's state $1s^2\ 2s^2\ 2p^2$ orbital arrangement [10]. The four $2s^2$ and $2p^2$ electrons are

converted into one of three fundamental hybridization configurations, sp^1, sp^2, and sp^3 during the bonding process with other atoms (Figure 2-3). Two of the four valence electrons enter orbitals in the sp^1 configuration, generating strong bonds along the x-axis, while the other two valence electrons create weaker links (form polymers). Graphite is the most stable carbon allotrope with sp^2 trigonal bonding (3 bonds with 120^o separation, one perpendicular to the plane) whereas diamond is an allotrope with sp3 tetragonal bonding (4 bonds with 109.5-degree angles). The strong, directed connections in diamond give it its exceptional physical qualities.

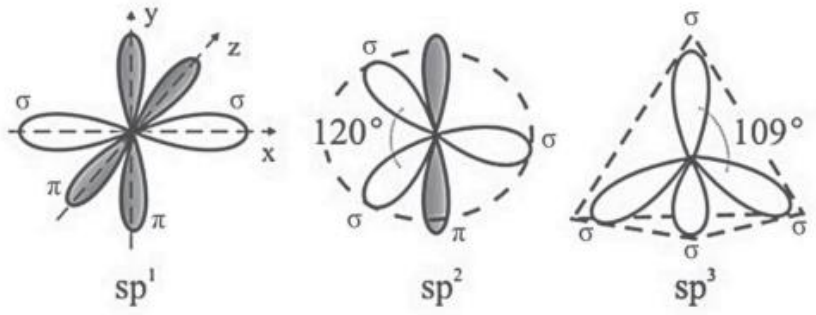

Figure 2-3. Three possible carbon atom hybridization structures.

Even though the C-C sp^3 bonds in the film give DLC its "diamond-like nature," the film must have other types of bonds and atoms if it is to be referred to as DLC, since only diamond is nearly entirely formed of carbon single sp^3 type bonds. According to literature, a film with less than 70% sp^3 percentage may be considered as amorphous-based DLC material [11]. Different types of bonds may be found in DLC films, including C-C sp^3, C-C sp^2, and C-H. sp^3 C-C modulus and hardness characterize the general characteristics of young. There isn't much contribution from the sp^2 C-C bonds. It's not necessarily a disadvantage because C-H bonds don't connect the network, but it may assist overcome pure diamond's inflexibility by producing relaxation throughout the film, which provides some elasticity to the film. It is also simpler to apply DLC coatings to complex geometries because of C-H bonding [12].

2.1.4 Diamond-like Carbon film as an Antireflection coating

DLC films are getting much consideration for the last two decades due to their extensive performance in the field of science. DLC coating has an enormous potential to use for several applications, As discussed in some literature review. Park and Chin deposited DLC film deposited on a polycarbonate sheet to protect it against radiation-

induced degradation [13]**.** Zhang et al. deposited DLC film adjacent to the infrared region with smaller thickness and showed a transmission rate greater than 85% [14]. Varied et al. showed that adhesion of DLC film on the wafer surface like germanium is poor at high temperatures such as 140 ^{o}C and infrared transmission is attained up to 95% in the array of 3 to 7-micrometer wavelength deposited at 25 ^{o}C. Raman data showed that the sp^3 structure in the DLC film attributes to the low-level adhesion produced by the internal stress which can be increased at high temperatures [15]. V.G. Levchenko & klyui et al. explained that there is a remarkable increase in the solar cell efficiency after depositing the film of DLC on the working side of the SCs. They deposited the film of Nitrogen-based DLC on the working side of the SC through RF plasma-enhanced CVD. Results revealed that nitrogen-containing DLC film with high radiation resistance can also be efficiently used for protecting coating for silicon cells and protect against the action of SCs that have low energy proton and UV radiations. They concluded that solar cell efficiency increased up to 1.45 times after deposition of DLC film on both sides of the silicon Solar cell [16]. Applebaum et al. explained the electron-damaging effect on the diamond-like carbon (DLC) coated crystalline solar cells [17]. Gontar et al. deposited Hydrogenated DLC film on the substrate surface by using the PECVD technique and 99% infrared (IR) transmission could be attained [18]. IR optic coatings such as BaF_2 and ThF_4 have poor adhesion and mechanical strength, according to Kotsay et al. A thin layer of DLC with a peak hardness of 3.6 GPa has also been coated by Kotsay et al. For ultra-broadband bandwidth of 2–16 microns, Pan et al. applied multilayer anti-reflective coating and DLC with a total thickness of 1.712 microns on ZnSe substrates The germanium buffer layer was 15 nm thick, with a DLC coating thickness of 100 nm. [19]. Li et al. sputtered high-thickness germanium–carbon films on ZnSe at higher temperatures. However, many sources report poor DLC adherence on germanium substrates at high temperatures. [20]. Miller et al. reported that internal stresses created during deposition cause film surface defects and poor DLC adhesion on germanium. Both authors reported DLC delamination and degradation on germanium deposited at 150 °C and 600°C. Varade et al. found poor adhesion of DLC films on germanium at temperatures above 150 °C but achieved 90% IR transmission at 3–7 μm wavelengths deposited at room temperature. [21]. Heeg et al. observed that fabricating DLC with a thickness greater than 600 nm at 160 °C could cause stresses that result in poor adhesion [22]. Reddy et al. improved DLC coating on a silicon wafer

and achieved transmission up to 89 percent and observed that by increasing acetylene flow rate, resulting in softer DLC. [23].

The first experiment was performed by Namba in 1992, he successfully deposited DLC coating on silicon by using the electrolysis of alcohol at a temperature under 70 ^{o}C [24]. Ismail et al. deposited DLC film from electrodeposition at 1200 V by varying the ratio of ethanol to methanol content [25]. Pang et al. prepared DLC film at low pressure and voltage (60-100 V) by using water and anhydrous ethanol as carbon sources [26]. Ceo et al. used methanol as a carbon source to deposit DLC film on a silicon substrate, the deposited film was composed of compact and small grains [27]. Gupta et al. deposited carbon-based film at a low voltage of 2.1 V and relatively high temperature by using acetic acid as a carbon source [11]. Ismail et al. and other investigators prepared DLC film from N, N-dimethylformamide, ethanol, methanol, and other organic liquid [28]. They deposited DLC film at a higher electric field (2 kV) [29]. Q. Zhang et al. successfully deposited compact and amorphous DLC film on SnO_2 glass at a lower voltage (3 V) and ambient temperature. He used chloroacetic acid as a carbon source. Mousa et al. prepared DLC film by electrolysis of pure methanol under constant voltage (1200 V) [30]. Mominuzzaman and Uddin deposited DLC film via electrodeposition on copper (Cu) and aluminum (Al) substrate by using variation in the volume content of methanol and applied different values of voltages [31].

Deposition from organic liquid source mostly carried out at high voltage (400-3000 V) and marginally higher than room temperature. At high voltage, the organic liquid near the electrode walls starts to boil. Tosin et al. studied the effect of liquid boiling near the electrode walls during the deposition of DLC film. He concluded that boiling near the electrode walls leads to a decrease in deposition rate and non-adhesive films. This issue can be resolved by lowering the applied voltage. However, a decrease in the potential leads to a decrease in current density but the deposition rate will also be decreased. This problem can be overcome by decreasing the separation distance between the electrodes. Moreover, at the lower separation distance between the electrodes, there is a great probability of radicals or ions arriving at a desirable electrode before recombination [32].

2.1.5 Comparison of DLC with other materials

DLC films may be deposited in several ways, such as by Chemical vapor deposition (CVD), ion beam assisted deposition (IBD), DC/RF plasma-assisted CVD, and sputtering. By employing, Vapor deposition using RF-assisted (13.56 mHz) plasma is a reliable method for depositing DLC film. DLC may be fabricated by PECVD at temperatures as low as 100-150 °C, while other CVD methods need high temperatures. The RF source employed in this technology also creates plasma, from which the film is created. Characteristics of light DLC Aluminum Transparency in optics NIR to FIR transition IR bands with a high reflectivity a refractive index ranging between 1.85 and 2.0 is not known [39]. The maximum thickness is 3 micrometers. The roughness of the surface all depends on the substrate you choose. Stresses It's impossible to quantify. Additional features Temperature range for DLC deposition: -10 to +400 degrees Celsius biocompatibility ensures cell integrity and prevents inflammation. sturdiness and effectiveness many things can activate plasma species in the form of ionized species (such as ions), excited species (such as electrons), abrasion-resistant species (such as dust and sand), water-soluble species (such as salt), acid-resistant species (such as ions), thermal shock (such as salt spray fog), and mechanical strikes. These up the ante in terms of vigor. Argon may be used as an etching agent in plasma to improve the film's durability. Stronger bonds are more stable and have "diamond-like" characteristics when Ar^+ is used to selectively etch weaker ones. A film's surface and physical qualities must match those of the substrate if it is to adhere well and last over time. As a result, it is critical to choose the proper substrate for the film and vice versa. Even if silicon may be a better option as a substrate, with DLC it may withstand many practical hard circumstances and produce some kind of synergy.

Table 2-1. Comparison of carbon-based materials.

	Diamond	**DLC (ta-C)**	**DLC(a-C:H)**	**Graphite**
Crystal system	Diamond cubic	Amorphous	Amorphous	Hexagonal
Mass density (g/cm^3)	3.51	2.5-3.3	1.5-2.4	2.26
Sp^3 Content (%)	100	50-90	20-60	0

Hydrogen content (%)	0	-1	10-50	0
Hardness (GPa)	100	50-80	10-45	<5
Friction coefficient in humid air	0.1	0.05-0.25	0.02-0.3	0.1-0.2
Friction coefficient in dry air	0.1	0.6	0.02-0.2	>0.6
Band gap (eV)	5.5	1-2.5	1-4	-0.04
Electrical resistivity (Ω cm)	10^{18}	10^{6}-10^{10}	10^{4}-10^{12}	10^{-6}-10^{-2}
Thermal stability in air (^{0}C)	800	400-600	300-350	>500

2.1.6 Other Applications of Diamond-like Carbon

DLC coatings can be used in a wide range of applications, with PVD coatings being the most common, aside from cutting tools, for high operating temperatures. DLC coatings are particularly useful in situations where a combination of friction and wear reduction is required. DLC is applied to the fronts of devices that allow for the quick and dry molding of difficult unprotected wood and aluminum surfaces, such as those found on automobile dashboards. DLC is a desirable material for clinical applications due to its superior wear, deterioration, and electrical characteristics. Fortunately, DLC has been shown to have exceptional bio-similarity. Piston pins, rocker arms, and other automotive components are examples of typical applications. [33].

• Medical: surgical instruments, prosthetics

• Pistols: slides, barrels, and bolt carriers

• Pistons, plungers, gears, and mechanical seals are examples of industrial parts and machinery.

• Injection moulding: dies, ejector pins, and other slick machine parts.

• Consumer goods: wristwatches, jewelry, and golf clubs.

2.2 Zinc Oxide

The basic characteristics and scientific applications of zinc oxide are discussed in this chapter. It highlights some of the optical, electrical, and structural properties of ZnO and Lanthanum doped ZnO, as well as their present applications in research and devices

- specifically as an Antireflection coating. It also goes through some synthesis and doping procedures, as well as intrinsic flaws and their impact on the material's optoelectronic capabilities. This chapter also looks at heat treatment in diverse environments and how it affects material properties.

2.2.1 Bonding Structure in ZnO

With a 3.3 eV band gap and a 60 meV exciton binding energy, zinc oxide is a potential room-temperature semiconductor. ZnO is a transparent and n-type conductor. The material's basic properties have been studied, and it has many potential applications in optoelectronics. [34]. Doping control is problematic in wide band gap materials like ZnO due to inherent flaws in the material structure. In ambient conditions, zinc oxide has a hexagonal wurtzite structure

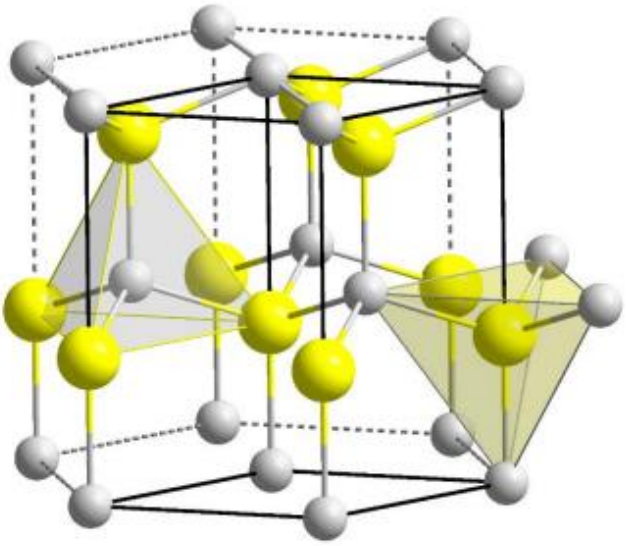

Figure 2-4. Depicted a ZnO single crystal's wurtzite structure. Each oxygen (grey) anion has four zinc (yellow) cations surrounding it.

Because defects occur in the crystal lattice of ZnO, natural n-type material can be formed, which has an impact on the structure, which in turn has an impact on the optical and electrical properties, as well as the overall quality of the device. These donors in zinc oxide can also compensate for the presence of acceptor dopants, hence preventing the formation of p-type conductivity in the material. The atmosphere in which the ZnO material is formed, as well as a variety of thermal treatment techniques used after synthesis, can all influence the presence of structural flaws. It will be possible to learn

more about the nature of defects in ZnO thin films and the material's characteristics and tuning capabilities by analyzing them.

2.2.2 General View on Properties of ZnO

Zinc oxide (ZnO) has a band gap of 3.37 electron volt. A divalent substitution on the cation site of ZnO can change the band gap of the material. While Mg doping raises the band gap (to 3.0 eV), Cd doping lowers it (to 3.0 eV). Oxygen vacancies or hydrogen doped ZnO in a normal hexagonal (wurtzite) crystal structure with a = 3.25 and c = 5.12 Zn interstitials in ZnO. About 0.01-0.05 eV below the conduction band, doping levels for n-type defects can be found. A direct band gap, a tightly bound exciton state, and gap states arising from point defects have been discovered in ZnO through photoluminescence, photoconductivity, and absorption studies, respectively. The UV photoluminescence peak at 3.2 eV is attributed to an exciton state because the exciton binding energy is approximately 60 meV. Visual emission can also be caused by defect states.

Table 2-2. Properties of wurtzite ZnO.

Property	Value
Lattice parameters at 300 k.	
a_o , c_o	0.32495 nm, 0.52069 nm
a_o/c_o	1.602 (1.633 for ideal hexagonal structure)
u	0.345
Density	5.606 g/cm^3
Stable phase at 300 K	Wurtzite
Melting point	1975^{0}C
Thermal conductivity	0.6, 1-1.2
Linear expansion coefficient (/^{0}C)	a_o:6.5 × 10^{-6}, c_o: 3.0 × 10^{-6}
Static dielectric constant	8.656
Refractive index	2.008; 2.029
Energy gap	3.4 eV (direct)
Intrinsic carrier concentration	<10^6 /cm^3
Exciton binding energy	60 meV

Electron effective mass	0.24
Electron Hall mobility at 300 K for low n-type conductivity	200 $cm^2/V. s$
Hole effective mass	0.59
Hole Hall mobility at 300 K for low p-type conductivity	5-50 $cm^2/V. s$

2.2.3 Growth Mechanisms and Structural Behavior of ZnO

Oxygen vacancies in ZnO were a major source of natural n-typing. However, oxygen vacancies are too deep to contribute to n-type conductivity [35]. This imperfection is nevertheless electrically and optically active, causing green luminescence [36]. It is possible to modify the optical properties of deep donors by using different annealing atmospheres such as hydrogen to change their colour from red to translucent [37]. The photoluminescence signal is reduced by annealing a ZnO thin film in Oxygen. In n-type ZnO, profound acceptor zinc vacancies easily occur. In oxygen-rich environments, the 2.2eV peak photoluminescence signal is stronger, indicating more zinc vacancies. Hydrogen-rich environments affect zinc vacancies. Because hydrogen is a donor, it will passivate the charge state of zinc vacancies. This increases n-type conductivity. The green luminescence is quenched when oxygen-rich ZnO is doped with hydrogen. Zinc's +2-charge state is stabilized by interstitial electrons above the conduction band minimum.

These defects cannot cause n-type doping because of their low formation energy, but they may cause p-type compensation [38]. A deep donor is zinc interstitials, however, the relationship between sublattice defects and zinc-interstitial complex is unknown. Zinc interstitials may move at normal temperature, forming a combination with nitrogen. This compound is a shallow donor that may improve ZnO conductivity [39].

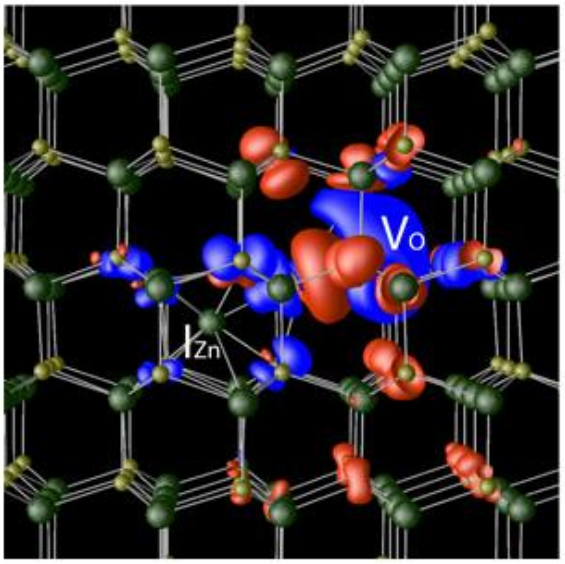

Figure 2-5. Depicts a zinc oxide lattice with oxygen vacancy (V_0) and zinc interstitial (IZn) defects. In the existence of these defects, charges are redistributed between positive (blue) and negative (red), increasing overall the conductivity of the n-type phase transition.

2.2.4 Comparison of Zinc Oxide with other materials

There have been several studies conducted about the design and production of ZnO thin films. There have been reviews of the characteristics of ZnO materials, as well as related studies on the structural and optical characteristics of ZnO films, as well as the associated production procedures, which have been documented. The fabrication of ZnO thin films was accomplished via the employment of sol-gel approaches throughout the investigation. A thin layer of Al-doped zinc oxide (ZnO: Al) was created by Singh et al. using the polycrystalline laser ablation (PLA) technology in 2001 [40]. The thin film was extremely conductive and transparent, and it was created in 10-60 minutes (6000-36000 laser shots). When it comes to producing zinc oxide nanorods, Ishikawa et al. achieved success by utilizing Polylactic acid (PLA) in deionized water medium at high temperature and ambient temperature in 2006 [41]. In addition, the effects of various variables on the films were studied by Chen and Zhang. In 2007, Thareja and Shukla created a colloidal suspension of zinc oxide nanoparticles in a variety of liquid environments. [42], which was published in the journal Nano Letters. Ajimsha et al. (2008) generated ZnO QDs in a variety of liquid environments using LP-PLA without a surfactant. They concluded that the defect and variations in laser fluency tuned the emission wavelength. Following that [43], in 2009, According to a study published in

Nature by Cho et al., they were able to make ZnO nanoparticles using (PLA) and deionized water (DIW). Factors like laser power, ablation duration, and age all showed significant increases in fluency on ZnO in their research. [43]. When ZnMnO thin films were prepared by PLA at temperatures of 300 degrees Celsius and 473 degrees Celsius, Virt et al. examined the properties of the films' polycrystalline ZnO and ZnMnO thin films. [44]. In 2011, Raid et al. produced ZnO using (PLA) and discovered that the fluency and wavelength of the laser have an impact on the optical characteristics, size, and morphology of ZnO that has been synthesized [45]. According to Atanasova et al. (2012), they generated a ZnO nanostructure using polymer liquid chromatography (PLA) and observed certain modifications on coatings after prolonged contact with air [46]. The (PLA) approach was used by Nakamura et al. in 2013 to successfully synthesize ZnO nanoparticles using a Q-switched Nd: YAG laser in the air, with spheres ranging in size from 10 to 20 microns [47]. Salim et al. (2016) [48] used an LP-PLA system to create ZnO nanoparticles utilizing a variety of laser wavelengths in the range of 1.06 and 0.532 m, laser fluency, and the number of laser pulses to achieve their results. The researchers found that the grain size of the films increased with laser fluency and decreased with the number of laser pulses used [49]. The researchers at Farhan et al. produced ZnO nanoparticles using polymer-based synthesis in 2016 and investigated the effect of different solvents (methanol and distilled water) on the characterization of ZnO nanoparticles in 2017. Because of the variation in laser pulse surroundings, they discovered that the ZnO nanoparticles had a hexagonal crystal structure and that different sizes were produced as a result of the change in laser pulse surroundings [50]. It was discovered that the surface of the nanoparticles had a granular shape by Ismail et al. made pure and Er+3 doped ZnO nanoparticles in ethanol at room temperature by using PLA [51]. Khashan and Mahdi et al. discovered that the sample contains hexagonal wurtzite when they formed nanocomposite based on ZnO:Mg in liquid using (PLA). In addition, the sol-gel technique is an essential approach in the creation of ZnO films, and various research have been conducted specifically on this technology in the last several decades. These investigations pertain to the sol-gel technique in its proper form, and the results of ZnO film are summarized below: - In 1956, the first application of sol-gel chemistry was made. Rustom Roy, a graduate student under the supervision of Elburt F. Osborn, was the first scholar to work on it. As part of phase equilibrium studies, Roy developed a sol-gel method for producing composites of tetra ethoxide and metal nitrate salts. A

group of researchers led by Phani et al. conducted research into AZO thin films prepared using the wet chemistry method in 2001. The images obtained using AFM and SEM reveal films that are uniform, continuous, and homogeneous in appearance. According to the XPS results, the film treated at 700 °C for 5 hours contained 17 % Zn, 14 % Al, and 60 % O_2. The characteristics of solution-based dip-coated ZnO thin films were investigated further by Murali in 2007. From 3.17 eV to 3.32 eV, the optical absorption measurements of the band gap energy were made. From 1000 to 10000 cm, the resistivity of the films was tested. He demonstrated that doping impurities such as Ga, Al, Mn, and other elements can reduce resistivity [52]. To measure the relative humidity in 2007, Xiaofeng et al. used a QTF-based humidity sensor coated with a sol-gel-derived nanocrystalline thin film. Highly sensitive and rapid water vapor detection was achieved using QTF coated with a nanocrystalline ZnO thin film created using sol-gel technology. [53]. In addition, in 2007, Bhattacharyya et al. investigated the fast response of a methane sensor fabricated from nanocrystalline ZnO thin films derived from the sol-gel method using the sol-gel method. Using the well-known sol-gel method to create thin nanocrystalline ZnO films, researchers were able to create a highly effective resistive gas sensor for sensing methane. As a result of these studies, Mehmet et al. carried out comparative characterizations of undoped ZnO thin films as well as reliability analyses of Al-doped ZnO thin films starting in 2009. To fabricate transparent conducting oxide modules, thin films of sol-gel derived undoped and Al-doped ZnO material systems are formed [54]. As previously stated, the annealed ZnO films demonstrated excellent transparency in the range of the wavelength between 400 to 800 nm [55]. Along with aging, Shane et al. (2011) investigated the effect of doping on the microstructure, morphology, and electric properties of transparent ZnO films made using the solution-based method. Throughout the study, the minimum doping concentration was 2 percent, and Aluminum (Al) is required to produce more conductive materials, which must be observed by hall measurements, according to the findings. When the annealing temperature is changed, the results of these measurements can change as well. For electrical properties, porous undoped ZnO films have a high resistance to current flow, while AZO films have a significantly lower sheet resistance [56]. Porous undoped ZnO films have a high resistivity to current flow [57]. Also in 2011, Sathya et al. investigated thin films from a position of strength in the ever-expanding field of solar cell research, as well as in the market itself. Zinc oxide derivatives, both pure and doped, are amongst the most adaptable materials available

for thin-film growth today. When it comes to producing high-quality thin films, the combination of dip coating and electrodeposition is a powerful tool. Indium Tin Oxide (ITO) is the primary advantage because it can be safely avoided because its procurement increases the cost and availability if it is not selective nowadays [58]. The secondary advantage is that it can be safely avoided because it is the primary precursor. ZnO thin films were investigated by Yang et al. in 2012 for their structure, morphology, and electrical characterization [59]. Because of the low boundary scattering, the study discovered that the grain size increased. Increases the value of surface roughness and the variations in electrical conductivity. Moreover, a study conducted by Yarub Al-Douri et al. in 2014 on the optical and structural properties of ZnO doped with indium (In) using a chemical spray deposition technique revealed that X-ray diffraction (XRD) peaks observed a shift in preferential orientation from (002) to (101) crystal plane with increasing indium dopant concentration [60]. Afterward, using the sol-gel method, Alaa. Ghazai and colleagues formation of pure ZnO thin films as well as Al-based ZnO films. They discovered that the films have a polycrystalline hexagonal wurtzite structure and that the lattice constants, crystallite size, and strain decrease as the Al dopant concentration in the ZnO lattice increases. Moreover, the band gap energy of ZnO is 3.37 eV for the direct band to band transitions and 3.25 eV for increased Al-doping concentrations. [61, 62]. A similar thin film of zinc oxide (ZnO) was formed by the solution-based method by Alaa. Ghazai and colleagues with a variety of zinc acetate to MEA ratios. A polycrystalline structure was observed in nature, according to XRD results for the prepared films. Lower grain size is observed for the ZnO (002) orientation, which is 9.9 nm for zinc acetate referred to as ZnO (002). The SEM images of zinc acetate films confirm that they have a rough surface, which is consistent with the XRD results.

2.2.5 Zinc Oxide as an Antireflection coating

A thin layer or multilayer of isolating dielectric materials, metals, or a blend of isolating materials is used as an anti-reflection coating to prevent undesired reflection on the surfaces of optical components [63]. These films have low absorbance (103 cm^{-1}) and are used to isolate objects. Anti-glare coatings on corrective glasses, camera lens elements, solar cells, Arial survey cameras, star sensors, and thermal imaging systems are examples of anti-reflective coating uses. Rayleigh described anti-reflection as the effect of coating optical components with a certain material (chemically) [64]. For

example, in 1857, Michael Faraday studied thin film deposition. A metallic wire heated by an electric current was constructed by Faraday.

For solar cell anti-reflection coatings, zinc oxide thin films have been produced. Because ZnO is affordable and non-toxic, it is easy to cultivate. They are transparent and non-absorbing due to their huge band gap. These ZnO nanorods may reduce broadband reflection by 10% and enhance efficiency by 2.4%, according to Chen and Sun [65]. According to Lee et al. [66], nanowires on silicon have a broadband reflectance of < 10% due to tapering throughout the growing phase. In this case, the Effective Media Approximation (EMA) of Bruggeman is used [67]. A vertical layer with varying heights or tapering may be broken into thin slabs. With a volume fill factor, each slab has an effective index of refraction. For sub-wavelength structures, Bruggemann's EMA is valid [68].

2.2.6 Other Applications of La-doped ZnO

Material features of transparent metal-oxide semiconductors (TMOS) include thermal stability, broad band gap, great transparency in the visible range, and high mobility. These qualities allow them to be used in transparent and flexible electronics, such as screens. LCDs and OLEDs are made using amorphous silicon and low-temperature poly-Si (LTPS) thin-film transistors (TFTs). With its mobility and low-temperature manufacturing, TMOS TFTs can replace a-Si and LTPS TFTs. With good mobility, electrical stability/reliability, and homogeneity, MO TFTs may be one of the most competitive technologies for next-generation displays. A-IGZO, InO, ZnO, and a-IZTO are MOs that have been intensively explored for oxide TFTs. Metal oxides are studied for their benign nature, cheap cost, broad band gap, and excellent mobility. Zinc oxide (ZnO) with a 3.15 eV band gap might be employed as a channel layer in oxide TFTs for active-matrix OLED (AMOLED) displays. ZnO TFTs may be made in a vacuum or solution. Spray coating, inkjet printing, and spin coating are all examples of solution deposition. This kind of active semiconductor is employed in TFTs. Spray coating creates a consistent, high-density layer across a vast area. The solution procedure produces polycrystalline ZnO. The threshold voltage varies in polycrystalline ZnO owing to grain boundary imperfections. In-doped ZnO TFTs have great mobility and a low threshold voltage [69].

Summary

In this chapter, there is a description of antireflection coating based on the DLC and ZnO thin film. In the first section, we describe the DLC material, its synthesis techniques, growth mechanism, and structural analysis. A comparison of DLC film with other carbon-based materials has been elaborated. In the literature review section, DLC film as an antireflection coating for silicon and advanced photovoltaics has been discussed. Surface functionalization of DLC has been described as one of the most elegant approaches for the development of carbon-based antireflection coatings for solar cell (SCs) applications. In the second section of this chapter, Zinc oxide thin film as an antireflection coating has been discussed. In which, description of Zinc oxide material, its synthesis approach, growth mechanism, and its structural analysis has been done. In the literature review section, the effect on optical, electrical, structural, and morphological properties after doping of various materials in the ZnO thin film has been elaborated. Whereas process optimization and judicious design of the DLC and Lanthanum doped ZnO-based AR coatings for solar cells application have been proposed.

References

1. Erdemir, A. and C.J.J.o.P.D.A.P. Donnet, *Tribology of diamond-like carbon films: recent progress and future prospects.* 2006. **39**(18): p. R311.
2. Bewilogua, K., D.J.S. Hofmann, and C. Technology, *History of diamond-like carbon films—from first experiments to worldwide applications.* 2014. **242**: p. 214-225.
3. Ahmed, M.H., et al., *Study of human serum albumin adsorption and conformational change on DLC and silicon doped DLC using XPS and FTIR spectroscopy*. 2013.
4. Pierson, H.O., *Handbook of chemical vapor deposition: principles, technology and applications*. 1999: William Andrew.
5. Soininen, A.J.E.-t., *Studies of diamond-like carbon and diamond-like carbon polymer hybrid coatings deposited with filtered pulsed arc discharge method for biomedical applications.* 2015.
6. Robertson, J.J.D. and R. Materials, *Mechanism of sp3 bond formation in the growth of diamond-like carbon.* 2005. **14**(3-7): p. 942-948.
7. Erdemir, A., J. Fontaine, and C.J.T.o.d.-l.c.f. Donnet, *An overview of superlubricity in diamond-like carbon films.* 2008: p. 237-262.
8. Mansour, A., *Structural Analysis of Planar sp3 and sp2 Films: Diamond-Like Carbon and Graphene Overlayers*. 2011.
9. Lifshitz, Y.J.D. and R. materials, *Diamond-like carbon—present status.* 1999. **8**(8-9): p. 1659-1676.
10. Vlček, J., et al., *UV-laser treatment of nanodiamond seeds—a valuable tool for modification of nanocrystalline diamond films properties.* 2012. **46**(3): p. 035307.
11. Taburoğlu, V.E., *Characterization and enhancement of IR optical and tribological properties of DLC films synthesized by RF-PECVD*. 2017, Middle East Technical University.
12. Macleod, A.J.T.F.C.I., Tucson, *Optical coatings from design through manufacture.* 2004.
13. Fontaine, J., C. Donnet, and A. Erdemir, *Fundamentals of the tribology of DLC coatings*, in *Tribology of diamond-like carbon films*. 2008, Springer. p. 139-154.
14. Grill, A.J.T.s.f., *Electrical and optical properties of diamond-like carbon.* 1999. **355**: p. 189-193.
15. Chen, Y.-N., et al., *Growth mechanism of hydrogenated amorphous carbon films: Molecular dynamics simulations.* 2014. **258**: p. 901-907.
16. Angus, J.C. and C.C.J.S. Hayman, *Low-pressure, metastable growth of diamond and" diamondlike" phases.* 1988. **241**(4868): p. 913-921.
17. Li, L., et al., *Growth and nucleation of diamond-like carbon (DLC) film on aluminum.* 2003. **206**: p. 691-695.
18. Lepienski, C.M., et al., *Factors limiting the measurement of residual stresses in thin films by nanoindentation.* Thin Solid Films, 2004. **447-448**: p. 251-257.
19. Van der Kolk, G., *Wear resistance of amorphous DLC and metal containing DLC in industrial applications*, in *Tribology of Diamond-Like Carbon Films*. 2008, Springer. p. 484-493.
20. Pagnoux, G., et al., *Influence of scratches on the wear behavior of DLC coatings.* 2015. **330**: p. 380-389.

21. Donnet, C., A.J.S. Grill, and C. Technology, *Friction control of diamond-like carbon coatings.* 1997. **94**: p. 456-462.
22. Choy, K.J.P.i.m.s., *Chemical vapour deposition of coatings.* 2003. **48**(2): p. 57-170.
23. Jones, A.C. and M.L. Hitchman, *Chemical vapour deposition: precursors, processes and applications*. 2009: Royal society of chemistry.
24. Fedosenko, G., et al., *Comparison of diamond-like carbon films synthesized by 2.45 GHz microwave and 13.56 MHz multi-jet radiofrequency plasma sources.* 2001. **10**(3-7): p. 920-926.
25. Huang, L.-Y., et al., *Analysis of nano-scratch behavior of diamond-like carbon films.* 2002. **154**(2-3): p. 232-236.
26. Huang, L., J. Lu, and K.J.T.S.F. Xu, *Elasto-plastic deformation and fracture mechanism of a diamond-like carbon film deposited on a Ti–6Al–4V substrate in nano-scratch test.* 2004. **466**(1-2): p. 175-182.
27. Leung, T., et al., *Determination of the sp3/sp2 ratio of aC: H by XPS and XAES.* 1999. **254**(1-3): p. 156-160.
28. Cloutier, M., et al., *Long-term stability of hydrogenated DLC coatings: Effects of aging on the structural, chemical and mechanical properties.* 2014. **48**: p. 65-72.
29. Gangopadhyay, A., et al., *Amorphous hydrogenated carbon films for tribological applications II. Films deposited on aluminium alloys and steel.* 1997. **30**(1): p. 19-31.
30. Miyake, S., J. Inagaki, and M.J.W. Miyake, *Dependence of the friction durability of extremely thin diamond-like carbon films on film thickness.* 2016. **356**: p. 66-76.
31. Wang, S., et al. *Corrosion resistance of optical diamond-like carbon film*. in *IOP Conference Series: Materials Science and Engineering*. 2020. IOP Publishing.
32. Iwamoto, Y., et al., *Preparation of DLC films on inner surfaces of metal tubes by nanopulse plasma CVD.* 2019. **380**: p. 125062.
33. Yang, Y., H. Zhang, and Y.J.C.P.B.E. Yan, *Synthesis of CNTs on stainless steel microfibrous composite by CVD: effect of synthesis condition on carbon nanotube growth and structure.* 2019. **160**: p. 369-383.
34. Hong, S.-J. and J.-I.J.J.o.t.K.P.S. Han, *Fabrication of indium tin oxide (ITO) thin film with pre-treated sol coating.* 2004. **45**(3): p. 634-637.
35. Biswas, P., et al., *Surface characterization of sol-gel derived indium tin oxide films on glass.* 2006. **29**(3): p. 323-330.
36. Kim, H.-W. and Y.-I.J.B.o.t.K.C.S. Kim, *Characteristics of indium-tin-oxide nanoparticles prepared by controlled chemical coprecipitation method.* 2008. **29**(9): p. 1827-1830.
37. Quaranta, F., et al., *Preparation and characterization of nanostructured materials for an artificial olfactory sensing system.* 2002. **84**(1): p. 55-59.
38. Ivanovkaya, M.J.E.S., *Gas-sensitive properties of thin film heterojunction based on In2O3 nanocomposites.* 2003. **7031**: p. 1-9.
39. Cox, J., G. Hass, and A.J.J. Thelen, *Triple-layer antireflection coatings on glass for the visible and near infrared.* 1962. **52**(9): p. 965-969.
40. Pulker, H.J.A.O., *Characterization of optical thin films.* 1979. **18**(12): p. 1969-1977.

41. Chopra, K., O. Grover, and R.J.A.o. Hradaynath, *Antireflection coatings effective at two wavelengths simultaneously in the visible region using homogeneously mixed dielectrics.* 1979. **18**(11): p. 1750-1752.
42. Azzam, R., et al., *Antireflection of an absorbing substrate by an absorbing thin film at normal incidence.* 1987. **26**(4): p. 719-722.
43. Nagendra, C., M. Viswanathan, and G.J.A.o. Thutupalli, *Design and optimization of low-loss wideband antireflection coatings for the visible and infrared regions: a new method.* 1985. **24**(8): p. 1156-1163.
44. Macleod, H. and T.-F.O.J.N.Y. Filters, New York, *McGraw-Hill.* 1989.
45. Chopra, K.J.N.Y., *Thin Film Phenomena McGraw-Hill.* 1969. **19692**: p. 196.
46. Klauder, J.R. and E.C.G. Sudarshan, *Fundamentals of quantum optics*. 2006: Courier Corporation.
47. Khudiar, A.I.J.U.o.T.-Q.J.o.S., *Fabrication temperature sensing by using ZnO Nanoparticles.* 2014. **4**(4): p. 75-78.
48. Musset, A. and A. Thelen, *IV multilayer antireflection coatings*, in *Progress in Optics*. 1970, Elsevier. p. 201-237.
49. Thelen, A., *Design of optical interference coatings*. 1989: McGraw-Hill Companies.
50. Rabinovitch, K. and A.J.A.o. Pagis, *Influence of heat treatments on the spectral performance of a V-type double-layer antireflection coating at 1.06 μm.* 1982. **21**(12): p. 2160-2166.
51. Hartnagel, H., et al., *Semiconducting transparent thin films*. 1995: CRC Press.
52. Özgür, Ü., et al., *A comprehensive review of ZnO materials and devices.* 2005. **98**(4): p. 11.
53. Clark, A.J.P., A.T. Films, and Devices, *Optical properties of polycrystalline semiconductor films.* 1980: p. 135-142.
54. Singh, A., et al., *Al-doped zinc oxide (ZnO: Al) thin films by pulsed laser ablation.* 2001. **81**(5): p. 527.
55. Ishikawa, Y., et al., *Preparation of zinc oxide nanorods using pulsed laser ablation in water media at high temperature.* 2006. **300**(2): p. 612-615.
56. Chen, Q.-H. and W.-G.J.A.s.s. Zhang, *Successive preparation of decorated zinc oxide organic sol by pulsed laser ablation and their luminescence characteristics.* 2007. **253**(8): p. 3751-3756.
57. Thareja, R. and S.J.A.S.S. Shukla, *Synthesis and characterization of zinc oxide nanoparticles by laser ablation of zinc in liquid.* 2007. **253**(22): p. 8889-8895.
58. Ajimsha, R., et al., *Luminescence from surfactant-free ZnO quantum dots prepared by laser ablation in liquid.* 2007. **11**(2): p. K14.
59. Cho, J.-M., J.-K. Song, and S.-M.J.B.o.t.K.C.S. Park, *Characterization of ZnO nanoparticles grown by laser ablation of a Zn target in neat water*. 2009. **30**(7): p. 1616-1618.
60. Virt, I., et al., *Properties of ZnO and ZnMnO thin films obtained by pulsed laser ablation.* 2010. **117**(1): p. 34.
61. Ismail, R.A., et al., *Preparation and characterization of colloidal ZnO nanoparticles using nanosecond laser ablation in water.* 2011. **1**(1): p. 45-49.
62. Atanasova, G., et al. *XPS study of ZnO nanostructures prepared by laser ablation*. in *Journal of Physics: Conference Series*. 2012. IOP Publishing.
63. Nakamura, D., et al., *Synthesis of various sized ZnO microspheres by laser ablation and their lasing characteristics.* 2013. **8**(3): p. 296.

64. Fadhil, F.A., I.H.J.E. Hadi, and T. Journal, *Preparation and characterization of zinc oxide nanoparticles by laser ablation of zinc in isopropanol.* 2015. **33**(5 Part (B) Scientific).
65. Salim, E.T., et al., *Physicochemical properties of ZnO Nanoparticles prepared using low energy low repetition rate Laser system.* 2016. **28**(5): p. 4501-4506.
66. Farahani, S.V., A. Mahmoodi, and M.J.I.N.L. Goranneviss, *The effect of laser environment on the characteristics of ZnO nanoparticles by laser ablation.* 2016. **6**(1): p. 45-49.
67. Ghazai, A.J., W.J. Aziz, and N.T. Yassen, *Effect of Laser Pulses and Energy on the Structural Properties of ZnO Thin Film Prepared Using PLA Technique.* 2017.
68. Khashan, K.S., F.J.S.R. Mahdi, and Letters, *Synthesis of ZnO: Mg nanocomposite by pulsed laser ablation in liquid.* 2017. **24**(07): p. 1750101.
69. Phani, A., et al., *Synthesis and characterization of zinc aluminum oxide thin films by sol–gel technique.* 2001. **68**(1-3): p. 66-71.

Chapter 3: Review on Experimental and Characterization Techniques

In this chapter, we present an overview of the materials processing and characterization tools. In the first section, we present an account of the deposition techniques used in during experimentation. Wet chemistry techniques, as well as vacuum-based film deposition techniques, have been used for thin film fabrication and/or characterization purposes. Among the wet chemistry processing techniques, we'll focus on electrodeposition and spin coating for film deposition. In the vacuum-based techniques, we discuss PECVD, and Thermal CVD, with a focus on the sputtering technique. The second section of this chapter is about an overview of the characterization tool used throughout this work. The working principles, the latest trends, and the models used in this work, all have been discussed in fair detail. Among the characterization tools, X-ray Diffraction, SEM, EDX, Infrared Spectroscopy, Atomic Force Microscopy, Electrical measurements, UV-Vis-NIR Spectroscopy, Raman Spectroscopy, Water Contact Angle, and solar cell current density–voltage analyses have been discussed.

3.1 Solution-Based Synthesis Techniques for Thin Films

The solar cell has several numbers of components. One of the most important components is antireflection coatings. It comprises several layers deposited over one another or a single layer. Besides, several characterization tools are required by films to be investigated. Bearing in mind the frequent need for film deposition, this portion presents a brief account of film deposition techniques used to fabricate coatings.

3.1.1 Sol-gel/Spin coating Technique

Sol-gel and spin coating are generally used as a solution-based technique for thin film deposition. The substrate is placed over a rotating platform, often a rotating disc. The process can be split into three basic stages. Initially, an excess of solution/dispersion is placed onto the substrate surface, usually at its center. At this time the substrate can either be at rest or already spinning. If it's spinning, the spinning speed is often kept low to equally distribute the solution/dispersion over the substrate. Surface coverage, as mentioned in the above discussion, varies to an excessive level on the wetting properties of the depositing fluid about the nature of the substrate's surface. The first stage comes to an end when sufficient volume of the solution/dispersion has been

placed on the substrate and delivery is halted. Then comes spin-up, in which the liquid begins to flow over the substrates' surface under the action of centrifugal force resulting from rotation. It is followed by a spin-off, that occurs with the increase of the angular velocity to the final spin speed. Excess of the fluid flows radially towards the edges and flies off the spinning disk at the edges. Thus, ensuring thinner films development. The disk rotation also induces a strong air flow, which in turn provides shear stress at the interface between the liquid and air. This further enhances the rate of thinning of the film. A spin-off stage is required for thin films deposition, as approximately 85–95% of the initially delivered amount of solution/dispersion outflows radially until the centrifugal effect is counterbalanced by viscous resisting forces. Film thickness depends on many but controllable parameters like spinning speed, spinning duration, number of revolutions, solution/dispersion viscosity, and concentration [1].

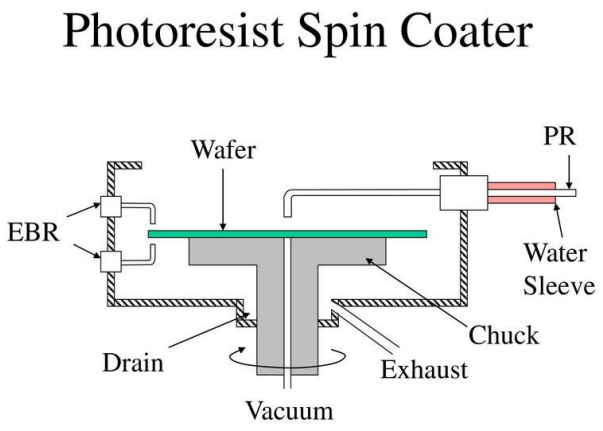

Figure 3-1. Schematic of Spin coater.

Films produced with this technology provide excellent homogeneity, precise thickness control, and consistency. However, there are limitations with the method like a considerable amount of material wastage, no large area coverage, and rapid drying of films. Rapid drying is disadvantageous in the sense that it leaves behind lesser time for molecular ordering. To do away with the problem, solvents that take longer to evaporate are often employed. To achieve sufficient molecular ordering and crystallinity, thermal annealing is often performed after deposition of the film.

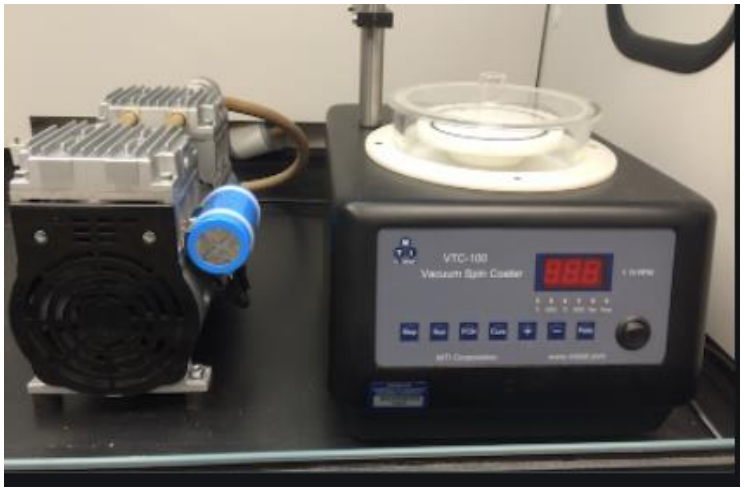

Figure 3-2. Vacuum Spin coater (VTC-100PA).

3.1.2 Dip coating

Dip coating is another solution-based wet chemistry method for the deposition of films with thickness from 25 nm to 60 µm allowing high precision in dip coating. To coat a substrate, a liquid coating material is immersed in a solution for a period and then extracted quickly. The coating process was carried out in a temperature-controlled environment. The coating's thickness can readily be adjusted. The solution's viscosity, withdrawal rate, and solid content all play a role. Thicker coatings and more viscous solutions result when substrates are withdrawn at a faster rate. [2].

Figure 3-3. Dip Coater (WPTL6-0.01 by MTI).

The advantage of using dip coating is that it is cheap and simple. It allows us to control the film thickness. Dip tanks come in different variety of shapes and sizes which allows coating on large and small substrates. The drawback of using such a deposition process

is the uncontrolled uniformity of the film. The film may be thicker at one edge of the substrate and thinner at the other.

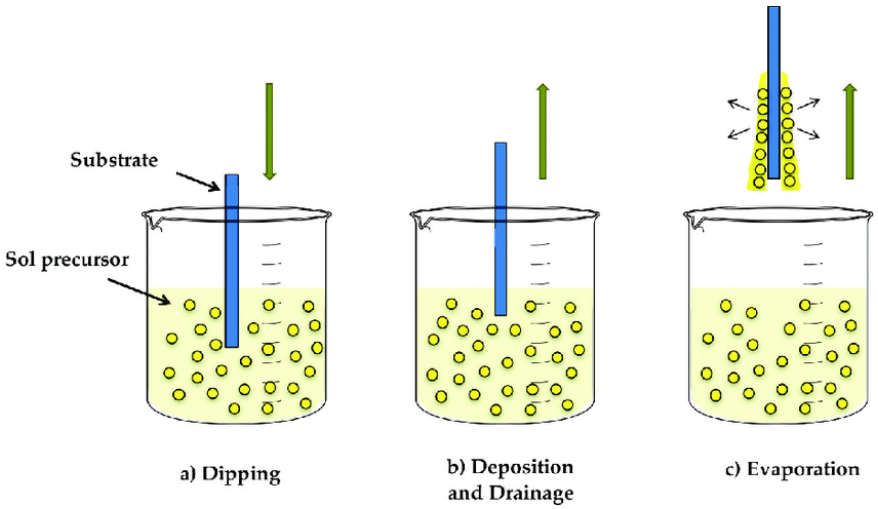

Figure 3-4. Schematic of Dip coating process.

3.1.3 Electrodeposition

The electrodeposition technique is a simple route to deposit a film on the substrate surface. Electrodeposition is getting intentions to the researchers because of its many advantages, such as lower deposition temperature, simple experimental setup, easily controllable parameters, low cost, and the possibility of a large area for deposition, as compared to the PVD and CVD techniques. Electrodeposition is a viable option for depositing most of the materials that can be deposited in the vapor phase. Methanol (CH_3OH), 2-propanol ((CH_3) CHOH), tetrahydrofuran (C_4H_8O), ethanol (CH_3CH_2OH), acetone (CH_3COCH_3), and acetic acid (CH_3COOH), and acetonitrile (CH_3CN) are the organic liquid that used for the DLC formation via electrodeposition. As an electrolyte, organic liquids rely heavily on dipole moment, dielectric constant, and viscosity coefficient to function properly. The dielectric constant and the dipole moment determine the maximum field that can be applied to a molecule. The film's qualities are greatly influenced by these parameters. The higher the dielectric constant, the higher the current density. In film deposition from organic liquids, the current density is critical. Increasing the dielectric constant can speed up the formation of thin films since it signals that more polarizing charged particles will be transported from liquid to electrode.

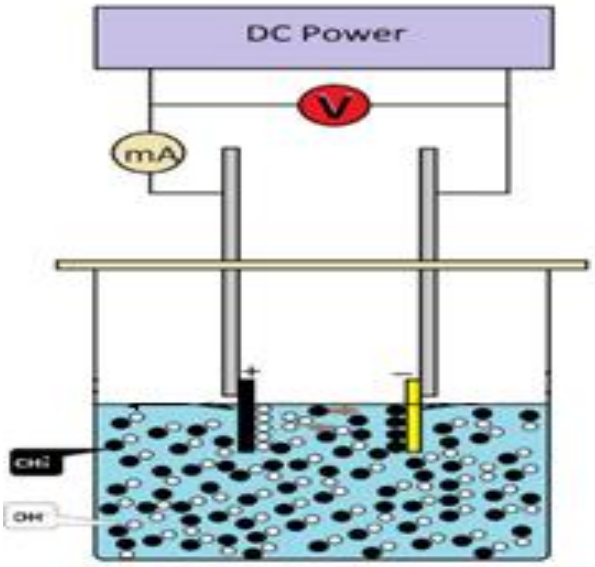

Figure 3-5. Schematic of electrodeposition Setup.

Table 3-1. Organic Liquids as an electrolyte.

Organic Liquids as an electrolyte	Dipole Moment (10^{-18}esu)	Dielectric Constant
Acetic Acid (CH_3COOH)	1.74	6.15
DI water (H_2O)	1.87	80.37
Methanol (CH_3OH)	1.70	32.7
Ethanol (C_2H_5OH)	1.69	24.55
N, N-dimethyl floramide	3.86	36.71
Formic Acid (HCOOH)	1.52	58
Formamide (CH_3NO)	3.73	109.0
Acetonitrile (CH_3CN)	3.92	37.5

In this current study, we will fabricate the DLC film via electrodeposition route by using the power supply that are capable to generate 300V (ELITE-300 PLUS).

Figure 3-6. Power Supply (ELITE-300 PLUS).

3.2 Vacuum Based Deposition Techniques for Thin Films

Using a production vacuum deposition system with several evaporation sources and a substrate heater, the vacuum deposition process was created. "Multi-source vapor deposition method with programmable substrates temperature regulation."

3.2.1 Chemical Vapor Deposition

Chemical vapor deposition (CVD) is a common method for depositing thin films on various materials. Its potential uses lie out of its ability to deposit a broad variety of materials at low temperatures. CVD is the reaction of vapor-phase chemicals (reactants) that contain the needed ingredients to generate a non-volatile solid film on a substrate. For the thin film, the reactant gases are sent into a reaction chamber, where they are broken down and reacted. At least some of the steps in a typical CVD process are [3]:

1. In the reaction chamber, the reactants, as well as diluent inert gases, are transported in bulk.

2. Reactant gas diffusion to the substrate surface.

3. Adsorption of the reactants on the surface.

4. Surface adsorption of reactants.

5. Adsorbed reactant molecules undergo a chemical reaction.

6. The removal of the byproducts of the reaction.

7. The byproducts of the reaction are dispersed by gas diffusion.

8. Bulk removal of reaction by-products and unreacted gases.

Thermally induced CVD reactions are time-dependent processes. The temperature has a big effect on how quickly things build-up, like in Figure 4. When the reaction is at a

low temperature, it is usually controlled by surface reactions. When the temperature is high, it is usually controlled by mass transfer.

An Arrhenius rule says that if you can't have too many reactions at once, you can't have too many solid films built up at once.

$$\mathbf{D.R. = A \exp (- E_a / RT)} \qquad (3.1)$$

Where,

D.R. is the deposition rate of the film.

Ea is the apparent activation energy of the chemical reaction.

R is the gas constant.

T is the absolute temperature (K).

A is constant.
The reaction rate rises with temperature, according to this equation. ln (D.R) vs. 1/T is linear.

A temperature rises to a point where the reaction rate approaches the rate at which the reactant species arrive at the surface, and the reaction rate cannot grow further unless the rate of diffusion and mass transport of the reactant species increases.

The activation energy and gas flow conditions are linked to the critical temperature at which the reaction mechanism switches from one rate-controlling regime to another. Adsorption of breakdown products on the substrate's surface might be another factor slowing film development.

Thermal CVD

The energy required for a chemical reaction that results in the development of a thin film on the substrate is provided by thermal CVD, which employs higher temperatures. The gaseous reactants are delivered into the reactor chamber by an inert gas such as nitrogen in atmospheric-pressure thermal CVD methods. Chemical vapor deposition is usually done at high temperatures to speed up the deposition process, improve crystallinity, increase density, and promote reactions that would otherwise be impossible. It's worth noting that when the film is deposited at low temperatures and then post-annealed at high temperatures, several of the film's qualities are difficult to

obtain. Stress creation, greater diffusion rates for components from the substrate into the film, and probable substrate deterioration are the main disadvantages of high-temperature deposition.

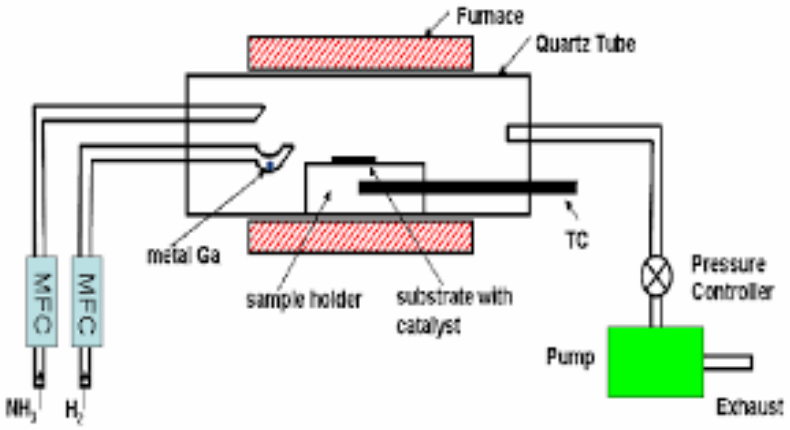

Figure 3-7. Schematic of Thermal CVD.

Plasma Enhanced Chemical Vapor Deposition

Chemical vapor deposition (CVD) is an important thin-film processing technology. Other than thin film deposition, the technology is also known for developing high-quality bulk materials, powders, and composites. For thin film deposition, CVD uses a flow of precursor gas (or gases) into a process chamber, where the substrate to be deposited is placed. As a result of chemical reactions taking place in the process chamber, thin films are deposited. The byproducts of the chemical reactions along with the unreacted precursors are exhausted out of the process chamber. CVD comes in many varieties. Among the different members of the CVD family, plasma-enhanced chemical vapor deposition (PECVD) is an important CVD process.

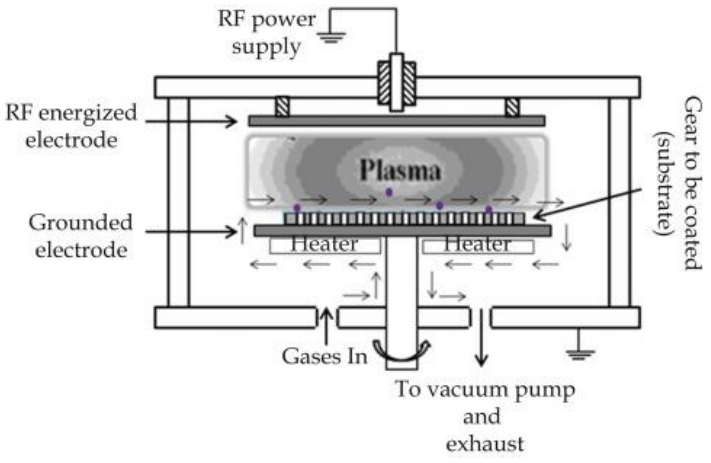

Figure 3-8. Schematic of PECVD Technique.

PECVD is a popular CVD technique for thin film deposition within the industry. The reason for its popularity is its capacity to be operated at lower processing temperatures than thermal CVD. PECVD employs a plasma of ionized species, electrons, and some unionized gas species for its operation. A high-frequency power, like that of the RF, ultrahigh frequencies, or microwaves is applied at reduced pressures to ignite and sustain the plasma. High pressure, such as the atmospheric pressures does exit, but they are scarce as plasma is more difficult to be sustained at enough high pressures. By the applied potential, the electrons are sufficiently accelerated to generate the reactive species, but without any significant rise in gas temperature. Due to these reactive species, films can be deposited at relatively lower temperatures.

Figure 3-9. Plasma Enhanced Chemical Vapor Deposition (NVPECVD).

We fabricate the antireflection coating. In which, we deposit DLC film by using the Plasma enhanced chemical vapor deposition.

3.2.2 Physical Vapor Deposition

Physical vapor deposition includes EB evaporation and sputtering, both of which may be employed with ion plating.

Commercial EB PVD coatings are deposited at deposition rates surpassing 25 μm/min in a vacuum environment (10^{-2}–10^{-4} Pa). Deposition occurs in an evaporant cloud when components are rotated between 800–1100°C. When applying these pressures, rotation is used to achieve consistent coverage. The growth of the coating

might cause problems including columnar grains with unbonded surfaces (known as "leaders"). To ensure effective adhesion, high deposition temperatures enhance surface diffusivity, decreasing the density of these leads. Preparing the substrates adequately prior to coating eliminates coating spallation.

Electron Beam Evaporation

In electron beam evaporation, a concentrated beam of high-energy electrons evaporates the source material. A heated filament emits thermionic electrons, which may be accelerated to produce enough energy to evaporate any substance. In a typical scenario, a 10 kV voltage drop accelerates 1 A of emission to 10 kW.

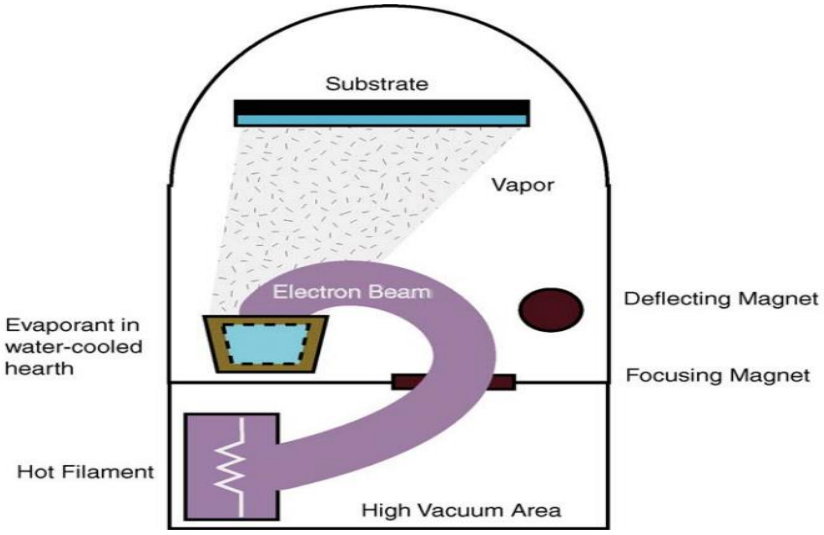

Figure 3-10. Schematic of Electron beam Evaporation.

As illustrated in Figure 3-10, a magnetic field, B, is applied to the filament to prevent it from being melted by the evaporator as it approaches it. A magnetic field, B, is applied to the filament to prevent the electron beam from being drawn to the surface by a magnetic field, B. The Lorentz force, F, on an electron in an electric (E) and the magnetic field is given by.

$$\mathbf{F} = \mathbf{F_e} + \mathbf{F_B} = q_e\mathbf{E} + q_e(\mathbf{v} \times \mathbf{B}) \qquad (3.2)$$

B = webers/m2=tesla; F = N; qe = C; E = V; v = m/s; In Fig.11, the cross-product vector FB is perpendicular to v and B. It accelerates electrons away from the filament or cathode in Eq. 3.2. According to the second force term, the electrons are deflected sideways as they cross the magnetic field lines. The second force is balanced by the centrifugal force of electrons curving at radius r.

Sputtering

The ejection of particles from a solid target material because of energetic particles bombardment onto the target is called sputtering. Energetic particles bombardment heats the target surface as well as transfers momentum to the target particles, compelling target particles to leave the surface. The energetic particles meant for bombardment are usually in the form of ions. The energetic particles that bombard the target are usually ions of sputtering gas. These ions are produced mostly because of electron collisions with the gas atoms while moving from cathode to anode via the gaseous medium [4].

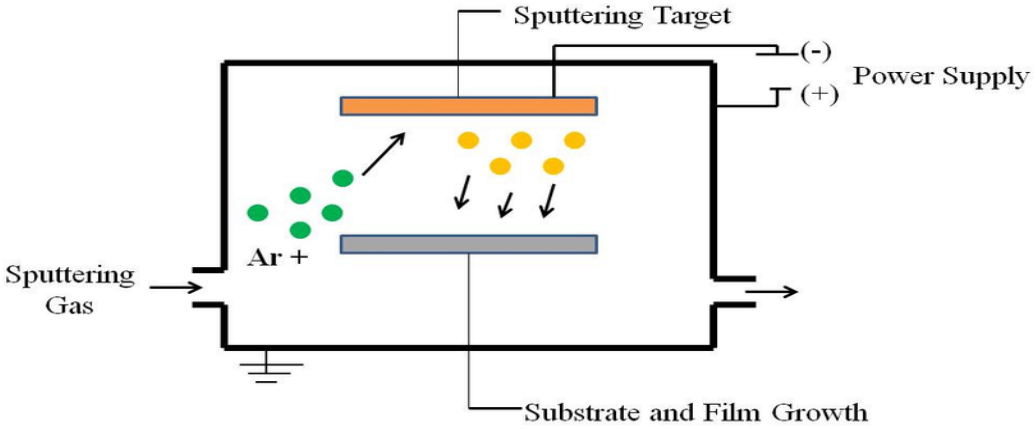

Figure 3-11. Schematic of Magnetron Sputtering.

Sputtering is an important technique. Controlled thin film deposition via sputtering is an established practice. Other than thin film deposition, today the technique is also widely used for surface cleaning and etching, surface analysis, and sputtering ion sources. There are several sputtering systems used for thin films deposition.

There are several ways to power the target, ranging from DC power for conductive targets to RF power for nonconductive targets, to several ways of applying voltage and/or current pulses to the target.

A glow discharge is the passage of electric current through a low-pressure gas, resulting in plasma formation. A potential difference is applied between the two electrodes. When the applied potential goes beyond the striking voltage (typically, in the kV range), the gas ionizes and transforms into plasma and starts to conduct electricity, causing it to glow as well. Characteristics of the discharge depend mainly upon the geometry of the cathode, anode, and the vacuum vessel, materials of the electrode, and the gaseous medium used.

Reactive-RF magnetron sputtering involves sputtering of a target material in the presence of a reactive gas or a mixture of gases as well as a magnetron arrangement. The process involves the sputtering of a target material in the presence of a reactive gas or a mixture of gases. The composition of the coating developed depends upon the composition of the sputtering atmosphere. In other words, the nature and chemistry of the sputtering material can be tuned with the type and magnitude of the reactive gas. In this way, a variety of materials can be deposited from a single target by just varying the chemistry of the sputtering atmosphere. Argon (Ar) is mostly applied as the main sputtering gas, whereas the magnitude of the reactive gas allowed into the process chamber, in most cases, controls the stoichiometry of the coating to be developed.

3.3. Characterization

3.3.1 X-ray Diffraction

Diffraction is the scattering of electromagnetic waves by a periodic long-range array, resulting in constructive interference at certain angles. When the electromagnetic waves involved are X-rays, it is termed as X-ray diffraction (XRD).

It was Von Laue in 1912, who suggested that crystals may be possibly used as diffraction gratings for X-rays. X-rays due to their wavelength (λ) resemblance with the distance between crystal atoms are considered suitable for diffraction by crystals. X-ray diffraction in crystals is a combination of two processes, i.e., scattering of X-rays by individual atoms and interference of the scattered X-rays. The following few lines explain this concept.

Each atom is a coherent scattering point, as its electrons do. An atom's light scattering strength is determined by its electron count. Crystals may diffract X-rays due to their periodic array of long-range organized atoms. The X-rays dispersed by atoms in a substance reveal their atomic organization. Amorphous materials lack periodicity and consequently lack a distinctive diffraction pattern. Thus, the diffraction pattern is indicative of a material's unique microstructure. A pattern is predicted for various atom arrangements. Many peaks may be seen in a single diffraction pattern of material.

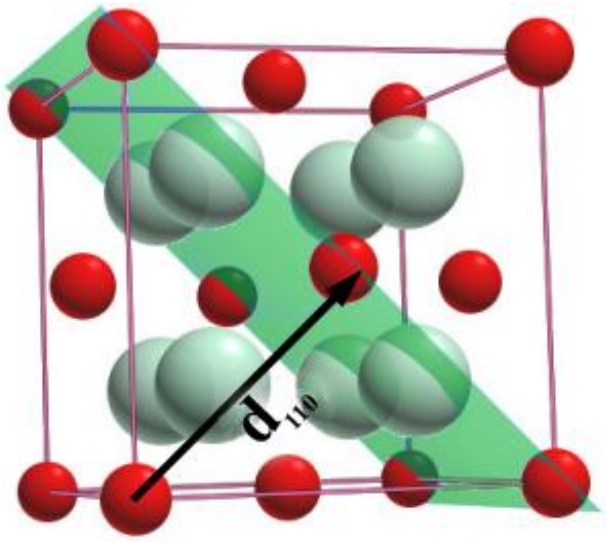

Figure 3-12. The position of the diffraction peaks is determined by the distance (d) between parallel atomic planes.

A crystal's structure is defined by its unit cell, whereas a crystal system describes the shape of the unit cell. Different planes of atoms are identified by Miller indices (hkl). The different diffraction peaks, that are commonly observed in the diffraction pattern of a single material, can be correlated to these atomic planes. Figure 3.13 explains the concept of different atomic planes and thus the different positions of peaks in a diffraction pattern.

Figure 3-13. X-ray Diffraction (D8-ADVANCE).

Bragg's law, in this regard, relates the angle for constructive interference with the interplane spacing. It states that for X-rays of wavelength λ falling on a family of parallel atomic planes, constructive interference occurs only at a specific angle 2 θ.

$$n\lambda = 2d_{hkl} \sin \theta \tag{3.3}$$

Here, n is a positive integer, whereas d_{hkl} indicates the magnitude of the vector starting from the origin of the unit cell to the plane (hkl). In simple words, it indicates the interplane distance between two adjacent planes of the (hkl) family.

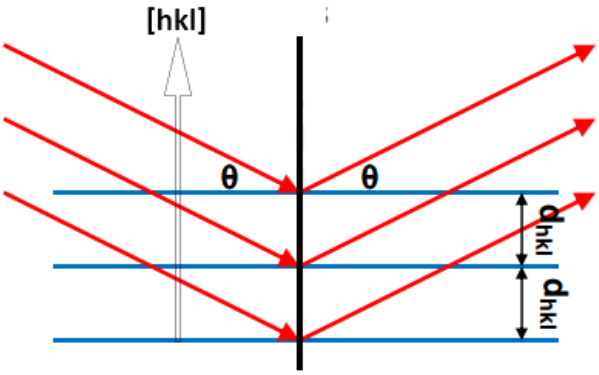

Figure 3-14. Scattering of X-rays of same λ and phase after falling on a crystal of interplane spacing, d_hkl at an angle θ.

3.3.2 Scanning Electron Microscopy

Scanning electron microscopy (SEM) involves the interaction between highly energetic electrons in the form of a focused beam, and a sample surface to produce several signals containing information about the sample. These signals contain valuable information regarding the morphology, topography, composition, microstructure, and material orientation of the test sample. Selected areas, as well as selected points, could be analyzed with SEM.

The energy of the fast-moving electrons is converted into other forms upon interaction with the sample. Some very useful signals are produced because of the electrons striking against the sample surface, including secondary electrons (SeE), backscattered electrons (BSE), diffracted BSE, X-rays, visible light, and heat. SeE and BSE are used for imaging purposes. SeE is especially important for morphology imaging and topography. BSE are often employed for showing compositional contrasts to

distinguish phases from each other. Characteristic X-rays contain information on the chemical composition of the material.

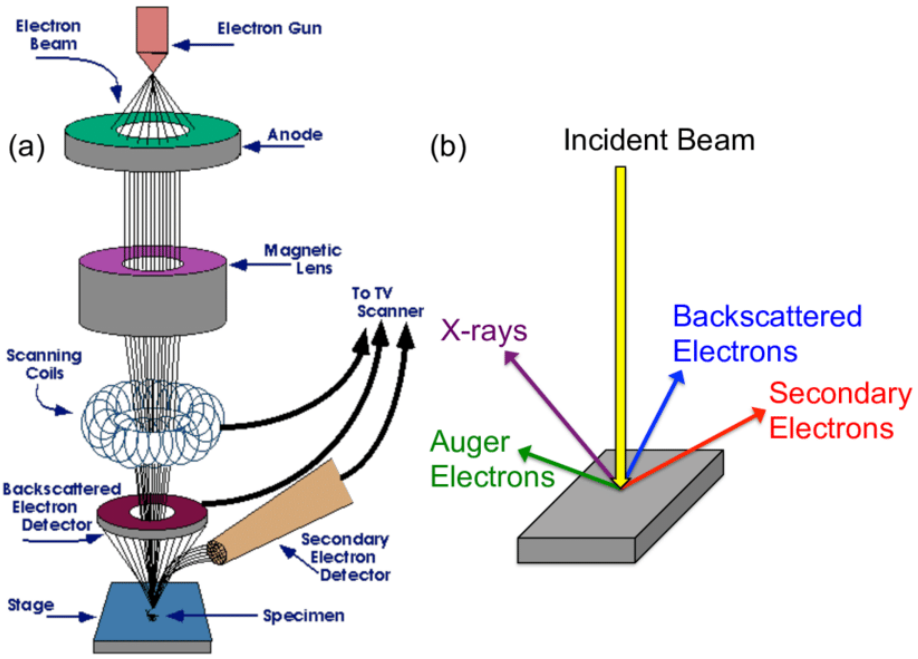

Figure 3-15. Schematic of Scanning electron Microscopy.

A scanning electron microscope typically requires an electron gun to eject electrons. The electron gun typically employs a tungsten filament, which upon heating thermionically emits electrons. A portion of the electrons, due to high velocities pass by the anode plate and stream down the column. In the process, the electrons acquire energy typically in the range 0.2 – 40 keV. The electrons are then focused by one or two lenses to a spot of diameter in the range 0.4 – 5 nm. This is followed by the passages of the beam through a pair of scanning coils or deflector plates. Here the beam is deflected in the xy-plane to cause a raster scan of the sample. The electrons lose energy because of interaction with the sample, resulting in several signals. Signal detectors in combination with data manipulation systems are used to gather information of interest. The information is further sent to the display devices. The whole process takes place at reduced pressures since electron travel with least scattering requires vacuum conditions.

Figure 3-16. Scanning electron microscopy (TECASN Vega 3).

Conventional SEM requires samples that are conductive and grounded to avoid charge buildup on the sample. Conductive samples such as metals don't require any special sample preparation procedures. Conductive samples may require cleaning followed by subsequent mounting onto the stub. However, insulating samples should be coated with a thin conducting material to avoid charge buildup on the specimen. Gold (Au) is often employed to deposit thin conducting film over non-conducting samples. Sample charging due to charge buildup results in image distortion and blurring since the incident electrons are repelled by this negative charge on the sample. For analyzing cross-section samples, cutting and polishing are often required. Cross-sections are usually mounted on a cross-section holder. Other than that, biological samples that are soft and contain fluids, to be analyzed by conventional SEM, require chemical fixation and dehydration prior to analysis.

In this work, Diamond like carbon film and Zinc Oxide thin film's morphology was analyzed by using VEGA 3 LMU, TESCAN model of SEM.

3.3.3 Energy Dispersive X-ray Spectroscopy

As seen in Figure 3-17, energy dispersive X-ray spectroscopy (EDS, EDX, XEDS, or EDXS), also referred to as energy dispersive X-ray microanalysis (EDXMA) or energy dispersive X-ray analysis (EDXA), is a method used to determine the elemental composition of a sample. EDS is predicated on the premise that each element is composed of atoms with a distinct atomic structure. Thus, each element emits a distinct

collection of distinctive x-rays upon stimulation. To cause a sample to emit X-rays, the sample must be bombarded with a beam of energetic charged particles (electrons or protons), or X-rays. Thus, EDS entails the examination of the X-ray spectra produced by the bombardment in order to determine the elemental composition.

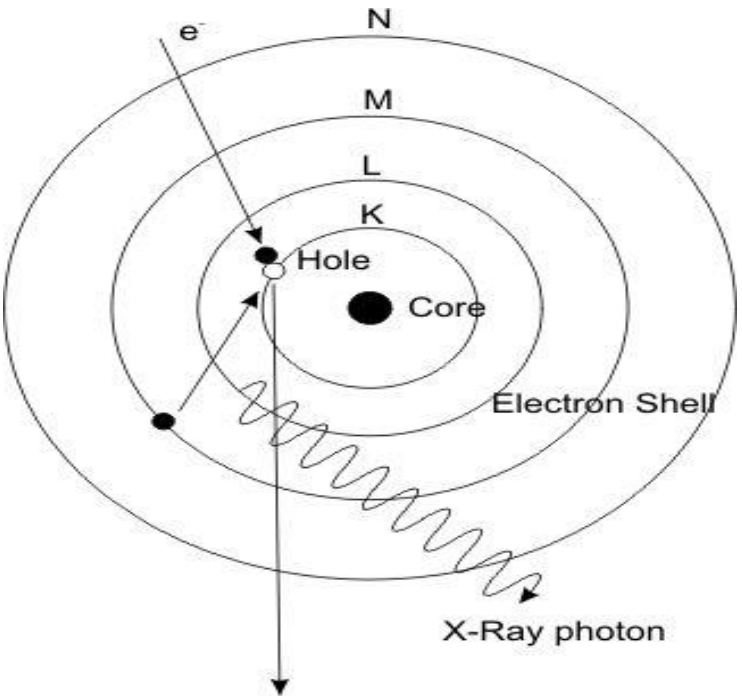

Figure 3-17. Working Principle of EDX.

When particles/radiations fall on a surface, depending upon the energy of the falling particles/radiations and the binding energies of the electrons, electrons might be removed from the surface. Sufficiently energetic particles/radiations can even remove inner shell electrons from the sample atoms. When an inner shell electron is removed, a vacancy (hole) is created in that shell. An electron from an outer orbit falls into that hole. This transition results in X-ray emission, characteristic of that element. X-ray lines are labeled by a capital letter that indicates the shell where the vacancy existed.

It may be K, L, or M, followed by a Greek letter ($\alpha, \beta, etc.$). α lines are the most important ones, β lines are less important than α but more important than lines indicated by other Greek letters that follow, and so on. The Greek letter is followed by a number (1, 2, etc.) in subscript, that corresponds to the intensity of the line in that peculiar group, such as Kα_1. Among the numbers, 1 stands for maximum intensity, while others in the sequence represent a correspondingly decreasing intensity.

When there is no number mentioned, it represents the combined intensity from all the X-rays in that group, such as Kα. Sometimes, the combined line is represented by mentioning more than one number in subscript, such as K$\alpha_{1,2}$.

3.3.4 FTIR Spectroscopy

FTIR spectroscopy involves chemical bonds and functional groups identification because of IR absorption by the specimen. These absorptions can be associated with the stretching and bending of covalent bonds of molecules of a specimen. Stretching vibrations, which are further classified as symmetric and asymmetric vibrations, are typically high energy vibrations than bending vibrations. It is to be noted that all covalent bonds are not capable of IR absorption. Only polar bonds are IR active and thus absorb IR radiations.

The results of IR spectroscopy are typically plotted as IR transmittance or absorbance vs IR frequency. Frequencies are represented as wavenumbers in units of cm^{-1}.

Figure 3-18. Fourier Transform Infrared Spectroscopy (Cary-630).

The typical frequency range for IR spectroscopy is from 650 cm^{-1} to 4000 cm^{-1}. The intensity of the bands due to absorption in the transmittance or reflectance spectra depends on the dipole moment of the polar bond. For strong polar bonds, strong IR bands are observed. For medium polar bonds, medium intensity bands, whereas for weakly polar bonds, low-intensity bands are observed. For symmetric bonds, no bands are observable.

IR spectroscopy is useful for identifying molecular fragments such as functional groups, thus providing information on the molecular fingerprint of materials. IR spectroscopy, however, does not provide proof of chemical formula or structure.

Dispersive instruments have been traditionally applied for obtaining IR spectra. Prisms were used in the first dispersive IR instruments. Later, gratings replaced the prisms in these devices. A monochromator contains the prism/grating. the dispersive element disperses the energy entering through the entrance slit and reflects it towards the exit slit. At the exit slit, the spectrum is scanned before passing it forward to meet the detector.

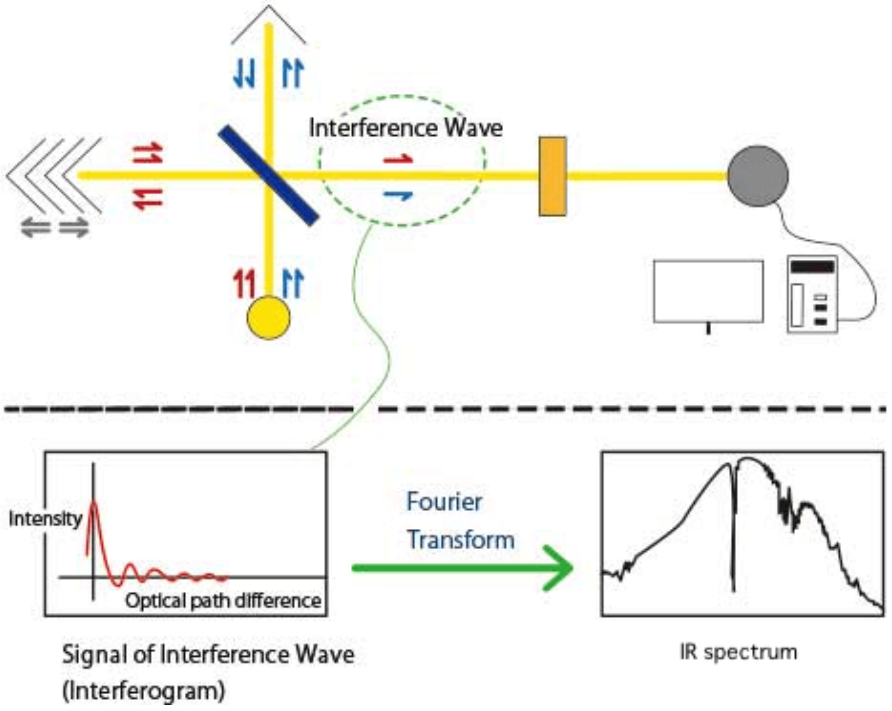

Figure 3-19. Schematic of FTIR spectroscopy.

Typically, the slit size of both the entrance and exit slits is programmed to vary to compensate for any variation of the input (source) energy with frequency. Thus, upon scanning the spectrum, the detector receives almost constant energy, provided no analysis sample is inserted.

The monochromator in the dispersive IR spectrometer has certain downsides. The entrance and the exit slits of the monochromator are meant to limit the frequency range of the energy to one resolution width. This makes the process too slow for a long-range of wavelengths. Samples that require quick speedy measurements, for example during online analysis, are not analyzable with such low sensitivity instruments.

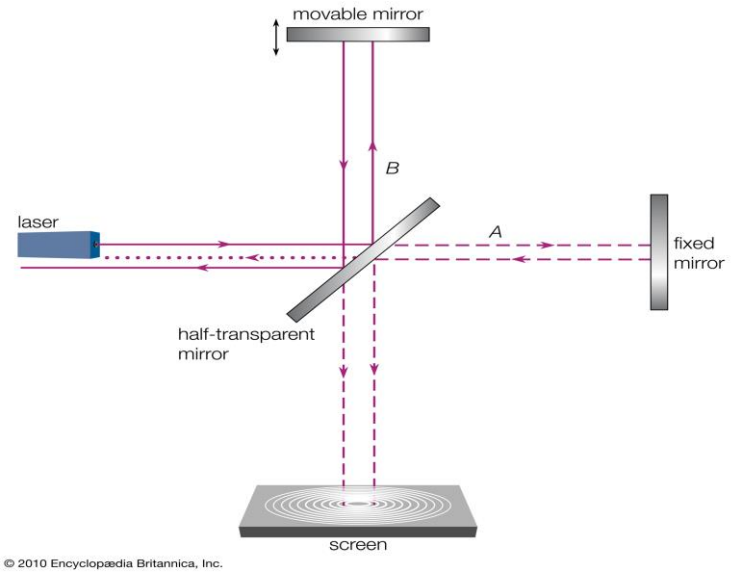

Figure 3-20. Schematic of a basic Michelson interferometer.

During the 1970s, commercial IR instruments employing a very different method were introduced. These instruments quickly replaced the traditional dispersive instruments. Spectrometers today predominantly employ the Fourier transform method to obtain the IR spectra, hence the name Fourier transform infrared (FTIR) spectrometers. These devices are superior in performance as well as data handling capability.

Any sample in any state may be analyzed with FTIR spectroscopy. Gases, liquids, pastes, powders, solutions, films, fibers, and surfaces are all examinable with FTIR, provided a judicious sample preparation choice is made. There are three basic sample preparation techniques, which include;

Mix the sample with a mulling agent (mineral oil etc.) and press between NaCl plates. NaCl is used because it is cheap and it capable of avoiding IR absorptions up to the 650 cm^{-1} mark. However, below 650 cm^{-1}, NaCl plates become absorbing as well. On the other hand, KBr plates, which are costlier than NaCl, remain transparent to 400 cm^{-1} point. Although the salt may be IR transparent, the mineral oil used is an IR absorber, and that's the downside of this technique.

KBr Method

The second technique is the KBr method, which involves mixing the sample with KBr and making pellets of the mixture through high-pressure pressing. The mulling agent and hence the absorptions associated with the mulling agent are avoided in this case. Only solids could be analyzed with this technique and that's the limitation of this method.

Another method uses CCl_4 to dissolve the sample and then press it between the salt plates. CCl_4 in this case is an IR absorber that's the limitation of this method.

In the current study, we have employed FTIR spectroscopy to detect the hydrogenated carbon bonds on the surface of the substrates to confirm the presence of DLC film. Due to this fact, (Agilent Cary 630) was used to detection of antisymmetric bonds.

3.3.5 Atomic Force Microscopy

To observe the nanometric and sub-nanometric details of a surface atomic force microscopy (AFM) is employed. Three-dimensional images of the surface can be obtained with AFM. The AFM method applies to materials, irrespective of their hardness, transparency, and conductivity.

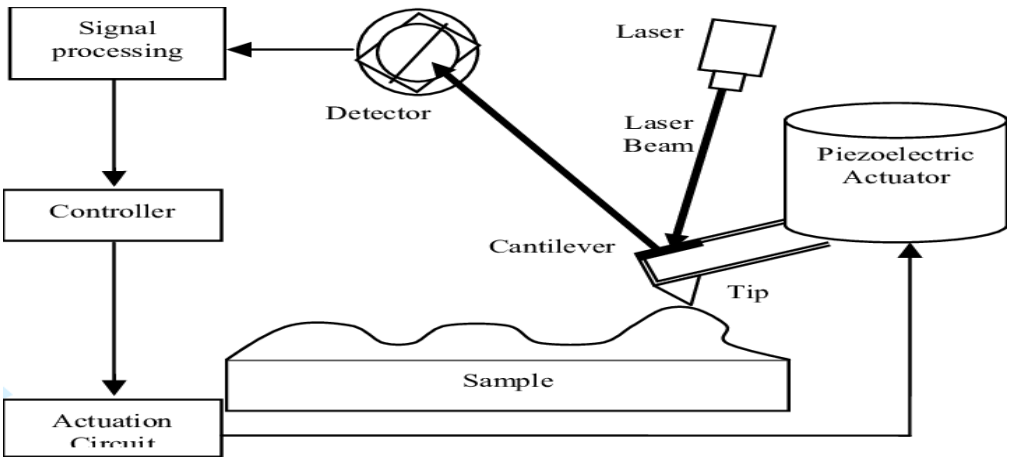

Figure 3-21. Working principle of AFM.

Each point on the 3D image exists because of the height measurements at that point. Generally, these heights are assigned typical colors, which distinguish points of different heights from each other. As a usual practice, dark for low and bright for high are the two extreme colors, whereas the color varies from dark to bright for intermediate heights. Thus, an image of multiple colors corresponding to each point height on the

surface is obtained. To measure heights, a probe is used. The probe when brought close enough to the sample surface experiences several forces, using these forces the height can be calculated. At short probe to surface distances, the dominant of these interactions for AFM purposes are Van der Waals forces. Long-range interactions such as the electrostatic, capillary, and magnetic interaction become important at farther distances from the surface and are crucial in other scanning probe microscopy (SPM) methods.

The probe is fixed to a cantilever. The cantilever can be thought of as a spring, whose spring constant (stiffness) along with the distance between the probe and the surface, determine the force experienced by the probe. According to Hook's law the force, F is given by

$$\mathbf{F} = -\mathbf{k}.\mathbf{x} \tag{3.4}$$

Here *k* is the spring constant of the cantilever and *x* is the deflection experience by the cantilever. If *k* of the cantilever (~ 0.1 – 1 N/m) is less than that of the surface, a cantilever bending is experienced. In the air, the typical range for this force is 10^{-6} uN – 10^{-9} nN. Feedback networks and piezo electronic scanners are used to control the probe motion across the surface. Monitoring the force between the probe and the surface is the primary driver behind the different instrumentation designs today. Typically, the probe deflection is measured using light reflection, the so-called beam bounce method. Light from a diode is bounced off the back surface of the cantilever onto a position-sensitive photodiode sensor. Thus, the cantilever bending is measured by the detector. These deflections are then mapped to generate the sample surface topography.

Figure 3-22. Atomic Force Microscopy (Model: Alpha 300 A).

AFMs operate in two fundamental modes: contact and non-contact. In contact mode, the probe is primarily affected by repulsive Van der Waals forces. Whereas in non-contact mode, when the probe is relatively far from the surface, it is the attractive Van der Waals interactions that are most essential.

The topography and roughness of produced DLC films were investigated using atomic force microscopy in this work.

3.3.6 UV-Vis-NIR Spectrophotometry

UV-Vis-NIR spectrophotometry is a technique that uses the electromagnetic waves in the ultraviolet, visible and near-infrared electromagnetic waves to study the absorption and/or reflectance of materials in these regions. The technique was originally developed for studying the absorption behavior of liquids. Usually, a spectrophotometer measures the percent transmittance ($\%T$) of liquid samples [5]. From $\%T$ data, the liquid's absorbance (A) can be calculated as follows

$$\boldsymbol{A = log\left(\frac{1}{T}\right)} \tag{3-5}$$

Whereas: $$\boldsymbol{T = \frac{\%T}{100}} \tag{3-6}$$

Today, however, the technique is widely employed for the analysis of solid samples as well.

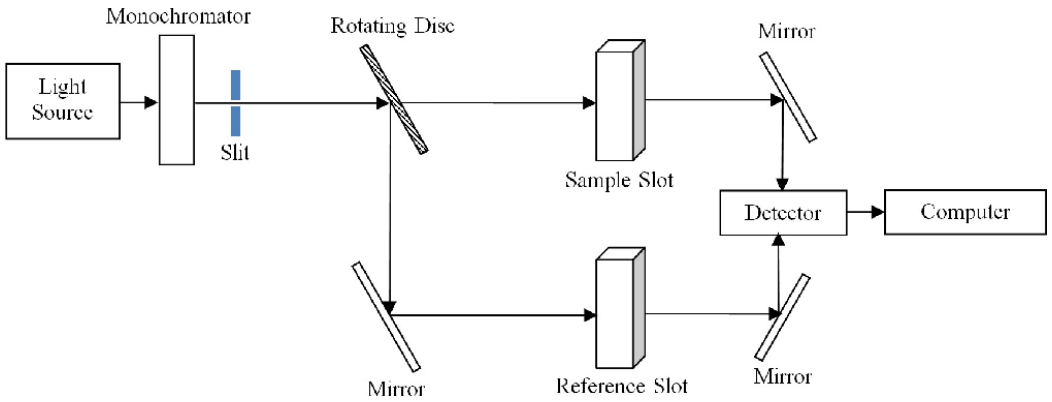

Figure 3-23. Schematic of the UV-Vis Spectrophotometer.

A beam of light when contacts solid, several phenomena may occur such as reflection, transmission, absorption, refraction, polarization, and diffusion. Typically, a spectrophotometer (or spectrometer) is used to measure the percent reflected ($\%R$), transmitted ($\%T$), and absorbed ($\%A$) components of the incident beam, bearing in

mind that the above-mentioned phenomena might be adding a degree of error to these measurements as well [8].

For a sample of dimensions large enough to receive the same amount of incident beam, both for the transmission and reflection modes, the results should be satisfactory over a large range of the electromagnetic spectrum. An integrating sphere is used to measure the overall transmittance, T. Overall transmittance includes both the direct and diffuse transmittance components. However, the direct and diffuse components of T can be measured separately as well. As far as reflectance, R is concerned, there are two types of reflectance, the specular and diffuse reflectance. When a portion of the incident beam bounces back at the same angle as the incident angle, it is called specular reflectance. Whereas diffuse reflectance is the reflectance from a sample in all directions. Generally, both specular and diffuse reflectance is observed in most of the samples.

Figure 3-24. UV-Vis-NIR Spectrophotometry (3600-PLUS).

There are techniques available to measure either specular, diffuse, or overall reflectance. An integrating sphere is most often used to measure the diffuse or overall reflectance. The percent absorbance, $\%A$, which is the percent of the incident light absorbed by a sample can be determined with simple logic. The absorbance, A is that component of the beam which is neither transmitted nor absorbed. UV-Vis-NIR spectroscopy assumes that the total incident beam after interacting with the solid goes into either T, R, or A [7]. Thus

$$\mathbf{100}\% = \%\boldsymbol{T} + \%\boldsymbol{R} + \%\boldsymbol{A} \tag{3.7}$$

or

$$\%\boldsymbol{A} = \mathbf{100}\% - \%\boldsymbol{T} - \%\boldsymbol{R} \quad (3.8)$$

Materials that cause significant light scattering and absorption such that they don't allow a significant portion of incident light to be transmitted through the material, are difficult to be analyzed for optical behavior using the UV-Vis-NIR absorption method. Thus, thick darker films with rough surfaces are difficult to be analyzed using the UV-Vis-NIR absorption method. However, Kubelka and Munk suggested that diffuse reflectance spectra of such materials can be extrapolated to obtain their absorption behavior.

The optical band gap, E_g is calculated from diffuse reflectance spectroscopy (DRS) data after transforming DRS data into data containing information on the absorption behavior of the material. Kubelka-Munk's theory is employed in this transformation. The Kubelka-Munk transformation calculates absorption spectrum in terms of the ratio of the sample's absorption coefficient, k to its scattering coefficient, s.

The Kubelka-Munk function, $f(R_\infty)$ is given as follows

$$\boldsymbol{f(R)} = \frac{\mathbf{(1-R)^2}}{\mathbf{2R}} = \frac{\boldsymbol{k}}{\boldsymbol{s}} \quad (3.9)$$

Here, R is the total diffuse reflectance measured using the integrating sphere and is given by

$$\boldsymbol{R} = \frac{\%\boldsymbol{R}}{\mathbf{100}} \quad (3.10)$$

The absorption coefficient, k can also be calculated from the extinction coefficient, κ using the relation

$$\boldsymbol{k} = \mathbf{4}\boldsymbol{\pi}\frac{\boldsymbol{\kappa}}{\boldsymbol{\lambda}} \quad (3.11)$$

Here, π equals 3.14159, whereas λ is the photon wavelength

The Kubelka-Munk transform, $f(R_\infty)$ is found to be approximately proportional to the absorption coefficient, k of the material. The scattering coefficient, s depends primarily on material properties such as particle size and refractive index. It doesn't depend strongly on λ and k. That's why s is considered as a constant in the Kubelka-Munk model. After obtaining $f(R)$ as a function of λ, a simple method to calculate band gap employs plotting $f(R)$ against photon energy in eV, followed by searching for two

linear patterns in the plot, the point on the energy axis above which the two (extrapolated) linear patterns intersect corresponds to the band gap of the material [8].

In the present work, we have used the UV-VIS Spectrophotometer to determine the optical properties of the synthesized ZnO and DLC films.

3.3.7 Hall Effect Measurement System

Hall Effect measuring device used to assess charge carrier type and density, mobility, conductivity, reactivity, and sheet resistance of semiconductor thin films.

Hall Effect measuring systems operate on the Lorentz force concept. Lorentz force is a force that combines electric and magnetic forces. When an electron travels perpendicular to the direction of the applied magnetic field, it encounters a magnetic force equal to -qv B. The direction of this magnetic force is governed by the right-hand rule, that is, in the opposite direction of the thumb. Lorentz force is the sum of electric and magnetic forces in this scenario and is computed as -q (E + v B), where E is the electric field and B is the magnetic field. Assume that a continuous current I flows along the x-axis in the presence of a magnetic field oriented in the z-direction. The charges are subjected to the Lorentz force, resulting in the generation of a hall voltage. When a charge is negative (n), the current direction is toward the negative y-axis; when a charge is positive (p), the current direction is in the opposite direction. By using ns = IB/qIVHI, the estimated hall voltage may be used to calculate the bulk density charge density.

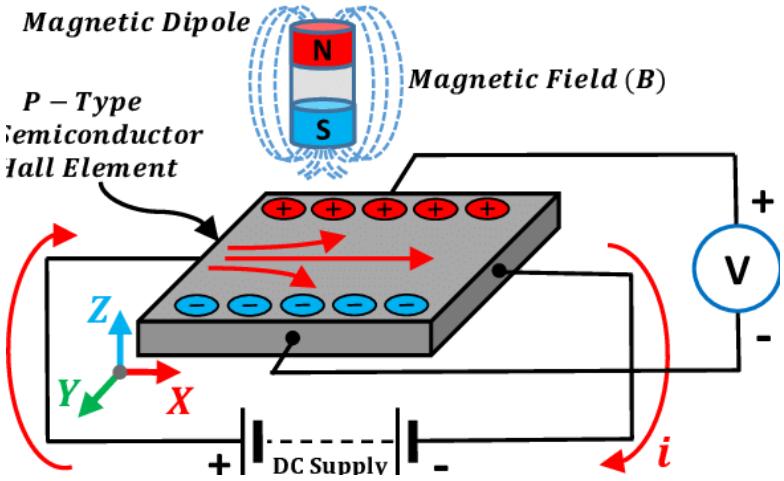

Figure 3-25. Hall Effect Schematic.

For n-type materials, the Hall voltage is negative, whereas, for p-type materials, it is positive. Now, the sample's sheet resistance is calculated using the van der Pauw

resistivity measuring method. This procedure necessitates the use of four ohmic connections and a square sample of the conducting material.

In this measurement, van der Pauw resistivity measurement technique suggest that there are two types of resistance PA and RB, which are related to sheet resistance as,

$$\mathbf{exp(-\pi RA/RS) + exp(-\pi RB/RS) = 1} \quad (3.12)$$

Mobility is calculated by $\boldsymbol{\eta=1/(qnsRs)}$ and similarly, bulk resistivity is calculated as Q=Rsd is the conductive layer thickness i.e., d is known.

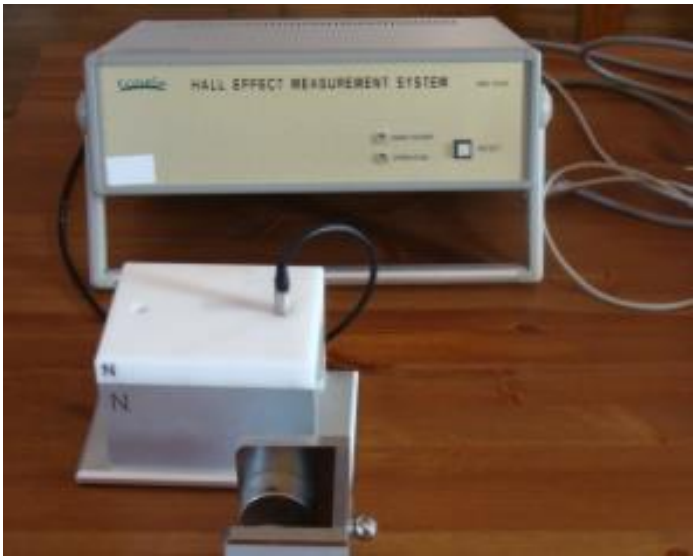

Figure 3-26. Hall Effect Measurement System (HMS-3000).

Hall Effect can also be utilized to calculate IV or IR curves for a conductive film in the required range of current. For better measurement, the sample must have,

- Flat sample of uniform thickness.
- Better ohmic contact, Sample must be symmetric.
- Sample uniformity and its thickness must be known.

3.3.8 Water Contact Angle Measurement

A goniometer is an instrument that is used to find the contact angle of the liquid droplet with the surface of the material. In which, there are two properties based on making an angle with the surface of the water droplet. If the contact angle is less than 90^o, then the material shows the property of hydrophilic. If the contact angle is greater than 90^o, then the material shows the property of hydrophobic. If the droplet makes the contact angle

less the 10^{o} with material, then material shows the property of the super hydrophilic. If the droplet makes the contact angle with a surface greater than 150^{o} then the material shows the property of the super hydrophilic.

The instrument is the main consists of several components: a monochromatic light source, a camera with high resolution, a tilting stage, software for contact angle analysis.

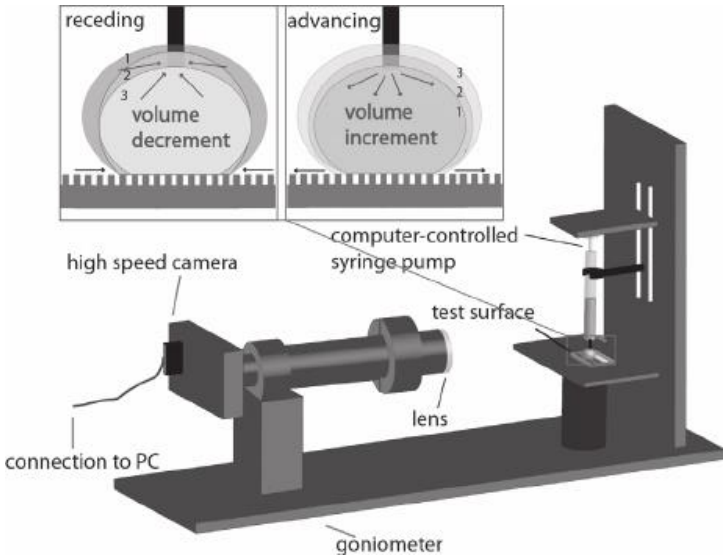

Figure 3-27. Schematic of water contact angle measurement.

When suspending a droplet from the tip of the needle and then comparing the droplet models over to the image capture by the whole system and the optical profile has been taken tensiometry measurement of the contact angle goniometer.

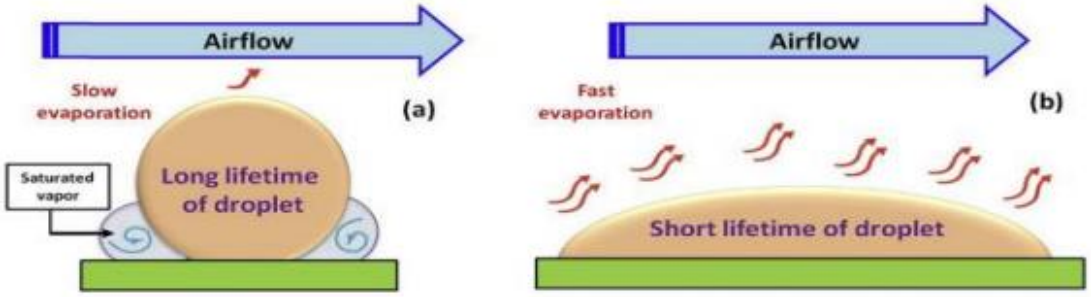

Figure 3-28 Water evaporation mechanism schematic diagram a) Hydrophobic b) Hydrophilic.

3.3.9 Raman Spectroscopy

Raman spectroscopy is a non-destructive system used to determine the chemical, structural, molecular interactions, polymorphism, and crystallinity of substances. It is entirely dependent on light's interaction with matter and on matter's interaction with

itself. (Internal Chemical Bonds) The study of molecules is carried out using light scattering methods such as Raman. In this method, the molecules scatter light emitted by a high-intensity laser source. Rayleigh Scattered is so named because the majority of scattering light has the same wavelength (or colour) as the laser source and so provides no useful information. While a little amount of light is scattered at different wavelengths, the wavelengths at which light is dispersed change according to the chemical structure of the analyte; this is referred to as Raman Scattering.

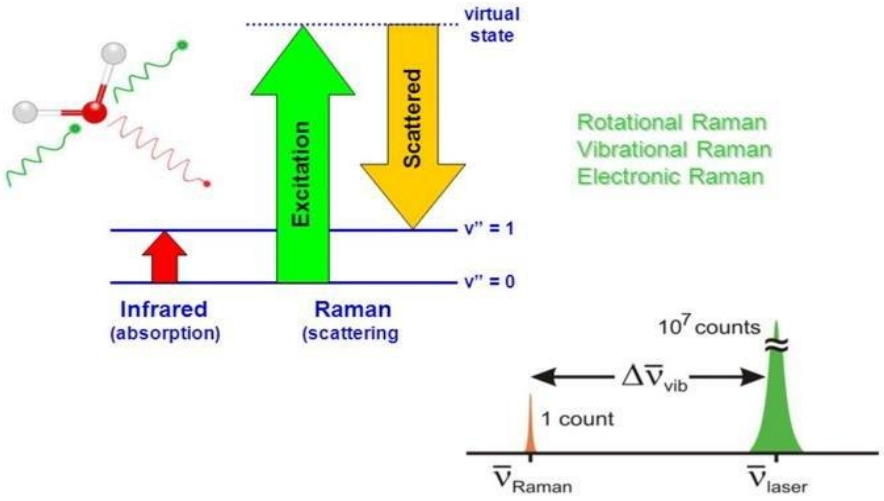

Figure 3-29. Working Principle of Raman Spectroscopy.

In a Raman spectrum, there are multiple peaks, each of which corresponds to a different intensity and spectrum position of the Raman scattered light. A separate chemical bond vibration is represented by each peak, including individual bonds such as C-C, C=C, N-O, and C-H, and groups of bonds.

Summary

Several deposition techniques for film formation have been employed in various experiments. Among the wet chemistry deposition routes, spin coating and electrodeposition techniques were employed. Among the vacuum-based techniques, plasma-enhanced chemical vapor deposition has been discussed, with emphasis on the underlying principle of operation, latest trends, and models used in the experimental section of this work. Physical vapor deposition is another important vacuum-based deposition technique. We presented an overview of the chemical vapor deposition process by focusing on plasma-enhanced chemical vapor deposition.

Thin Films were characterized using several characterization techniques. X-ray diffraction has been discussed with emphasis on the working principle. The governing principles of scanning electron microscopy and energy-dispersive X-ray spectroscopy have been discussed. The underlying principles of infrared spectroscopy and a contrast between the traditional dispersive IR spectroscopy and Fourier transform infrared spectroscopy have been made. In the section for atomic force microscopy, its working principle, its different modes of operation have been discussed in fair detail. In the electrical measurements portion, electrical and hall measurements have been presented. In the section for UV-Vis-NIR spectrophotometry, the basic physics behind the absorption and diffuse reflectance spectra has been discussed. Further, we have presented an account of water contact angle with a prime focus on the wettability property.

References

1. Middleman, *S., The effect of induced air-flow on the spin coating of viscous liquids. Journal of Applied Physics*, 1987. **62**(6): p. 2530.
2. G. Rabilloud, High-Performance Polymer, Editions OPHRYS, 1999.
3. D. Depla, S. Mahieu, J. Greene, Sputter deposition processes, Handbook of deposition technologies for films and coatings: science, applications and technology (2010) 253-296.
4. J.-H. Park, T. Sudarshan, Chemical Vapor Deposition: Surface Engineering Series, ASM International, 2001.
5. J.H. Warner, F. Schaffel, M. Rummeli, A. Bachmatiuk, Graphene: Fundamentals and emergent applications, Newnes, 2012.
6. P. Kubelka, F. Munk, An article on optics of paint layers, Z. Tech. Phys 12 (1931).
7. A.E. Morales, E.S. Mora, U. Pal, Use of diffuse reflectance spectroscopy for optical characterization of un-supported nanostructures, Revista Mexicana de Fisica S 53 (2007) 18.
8. B. Wells. Bandgap measurements of nonspecular materials using a bifurcated fiber optic method of diffuse reflectance 2015.

Chapter 4: Experimental

Lanthanum doped ZnO and DLC thin film were synthesized by using wet chemistry and vapor phase deposition. In the experimentation process, we will synthesize the Lanthanum doped ZnO thin film by using the sol-gel and spin-coating techniques. Diamond-like carbon film will deposit via two methods i.e., RF-Plasma enhanced CVD and Electrodeposition.

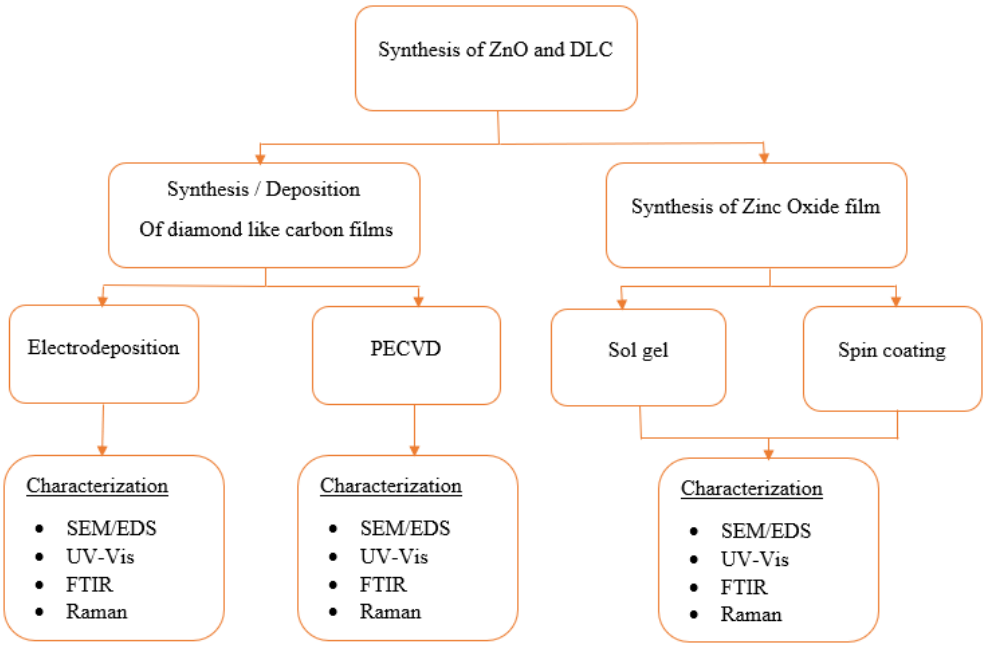

Figure 4-1. Flow chart to deposit DLC & La-doped ZnO thin film.

4.1 Formation of Lanthanum doped ZnO film

4.1.1 Substrate Cleaning

Soda-lime glass (SLG) was utilized as a substrate for deposition. Before Deposition, substrates were cleaned with cleaning solvents. First, substrates were cleaned with ethanol and acetone sequentially and then rinsed in Deionized water (DI) water to remove any contamination. After cleaning with solvents and HF solution, the substrates were cleaned in the plasma cleaner.

4.1.2 Synthesis of La-doped ZnO via Sol-Gel Method

Material and Method

Zinc Acetate Dihydrate (Sigma Aldrich 99.9% Purity), Lanthanum Nitrates Hexahydrate (Sigma Aldrich 99.9% Purity), Ethanolamine, methanol, and absolute

ethanol were procured from the sigma Aldrich.

For the synthesis of ZnO thin film, 2M solution was prepared, Zinc Acetate Dihydrate was dissolved in the solvents of methanol and ethanol having the ratio 1:1. After that, the solution was stirred for 6 hours at 60 ^{o}C. Ethanolamine (EA) was used as a stabilizer to make the solution transparent. After adding the EA, the solution was stirred for 4 hours to make the solution fully transparent. After Completion of stirring, then we aged the solution for 24 hours. The solution was labeled with the sample ID-ZO-0. For doping of the Lanthanum into ZnO, we used lanthanum nitrate hexahydrate as dopant precursor. The concentration of Lanthanum into ZnO was varied between 1 at. % to 3 at. %. After aging, the solution was ready for the spin coat to synthesize the ZnO and Lanthanum doped ZnO thin film. Thin Films was prepared after 6 spins (number of coatings) of sols via spin coater onto the substrate with the speed of 3000 rpm for 30 sec. To evaporate the volatiles and undesirable solvents, the substrate was heated to 120 ^{o}C for 10 min. Finally, to achieve the crystallinity of the ZnO and Lanthanum doped ZnO, the sample was annealed in the magma furnace at 450 ^{o}C for 2 hours with 3^{o}C/min.

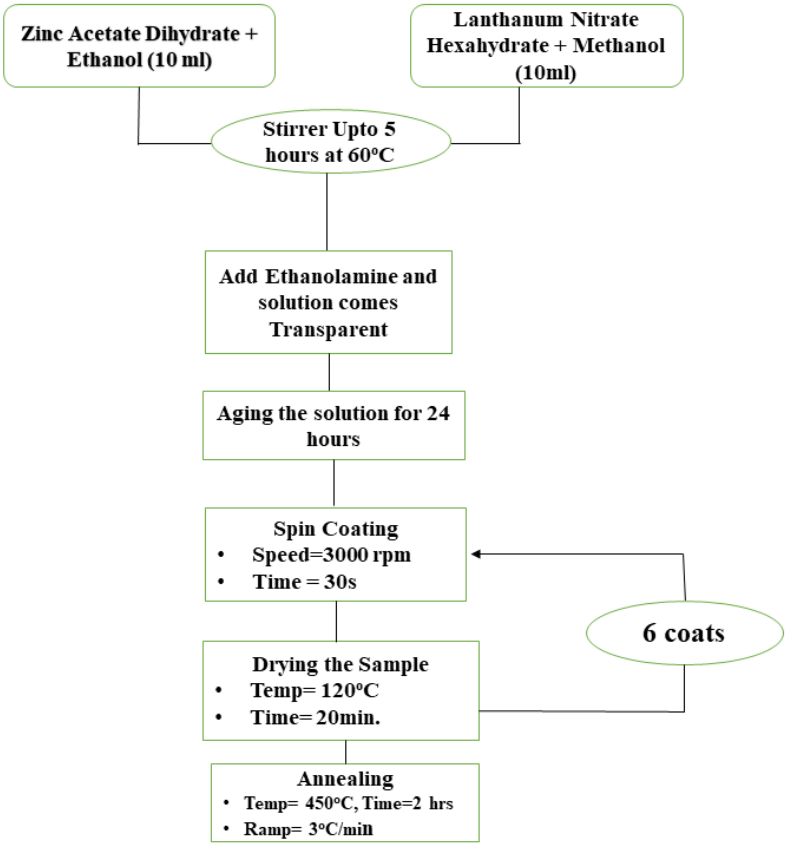

Figure 4-2. Flow chart to deposit pure ZnO & La-doped ZnO thin film.

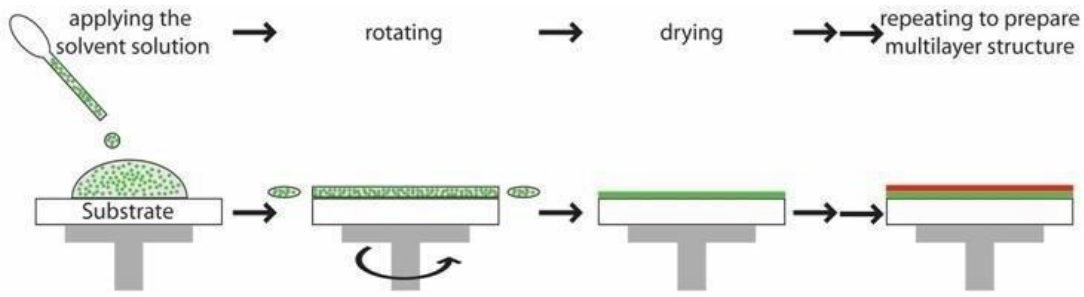

Figure 4-3. Schematic of Spin coating.

Deposition Parameters to Deposit Pure and Lanthanum doped ZnO Thin Film

Table 4-1. Deposition Parameter for deposition of La-doped ZnO Thin Film.

Precursor Solute	Precursor Solvent	Conc. Of La in ZnO	Stabilizer	Aging Time	Speed & Time	Annealing Temp.
Zinc acetate dehydrate. Lanthanum nitrate hexahydrate.	Ethanol Methanol	0% 1% 2% 3%	Ethanolamine	24 hrs	3000 & 30 s	450 °C with 3 °C/min for 2 hrs

4.1.3 Characterization for La doped ZnO film

Surface morphology was analyzed by using the Scanning electron microscope (VEGA 3 LMU, TESCAN). ZnO thin films were characterized through PXRD (Rigaku, ULTIMA, 40 kV, 30 mA) using Cu Kα radiation of wavelength 1.5418 Å. Structural characteristics of ZnO film were observed by using Raman spectroscopy by using 532nm laser. The Optical properties like absorption coefficient of the ZnO film, reflectance, and transmittance were measured by using the ultraviolet-visible spectrometer. The electrical resistivity was determined by using the Hall effect (HMS 3000, Ecopia). After that, contact angle measurement was carried out using a contact angle meter to get a better understanding of the wettability property of these materials (optical tensiometer).

4.2 Formation of DLC film

DLC film will be coated on silicon and glass substrates by using the plasma Enhanced Chemical Vapor Deposition and Electrodeposition.

4.2.1 Plasma Enhanced Chemical Vapor Deposition

4.2.1.1 Cleaning of Substrates

Silicon, FTO coated glass, and Soda-lime glass was used as a substrate. Before Deposition, substrates were cleaned with cleaning solvents. First, substrates were cleaned with ethanol and acetone sequentially and then rinsed in Deionized water (DI) water to remove any contamination. To remove the oxides from the surface, silicon was cleaned with an HF solution. After cleaning with solvents and HF solution, the substrates were cleaned in the plasma cleaner.

4.2.1.2 Synthesis of Diamond-like Carbon film via PECVD

Materials and Method

Diamond-like carbon film was deposited on 2 cm × 2 cm Soda Lime glass, FTO glass, and silicon substrates by using a 13.56 MHz RF-PECVD system. Before deposition, to avoid any contamination, the substrates were cleaned with ultra-sonication, methanol, acetone, and De-ionized water. After cleaning, the substrates were mounted on the holder in the PECVD system. To remove the oxide layer from the surface of the substrates the argon plasma was generated in the chamber for 5 minutes at the flow rate and pressure of 10 sccm and 2.13×10^{-1} Torr, respectively. To improve the adhesion between the substrate and the film, the hydrogen gas was introduced as a reducing agent for 2 minutes at the flow rate of 10 sccm and pressure of 4×10^{-1} Torr. The reaction gas was inserted into the chamber with a mixture of hydrogen and methane at the flow rate of 20 sccm and 5 sccm, respectively. RF power for plasma generation was maintained at 100 W with a working gas pressure of 5×10^{-1} Torr. The whole process was carried out at ambient and 100 ^{o}C.

Deposition Parameters for DLC formation via PECVD

Table 4-2. Deposition parameters of DLC film deposited at different Temperatures.

Substrates	SLG, silicon (100), and FTO glass

Deposition gases	Methane (CH_4): 5 sccm Hydrogen (H_2): 20 sccm
Gasses Ratio	1:4
Deposition time	20 minutes
Power	100 Watt
Working Pressure	5×10^{-1} Torr
Substrate Temperature	Ambient / 100 ^{o}C

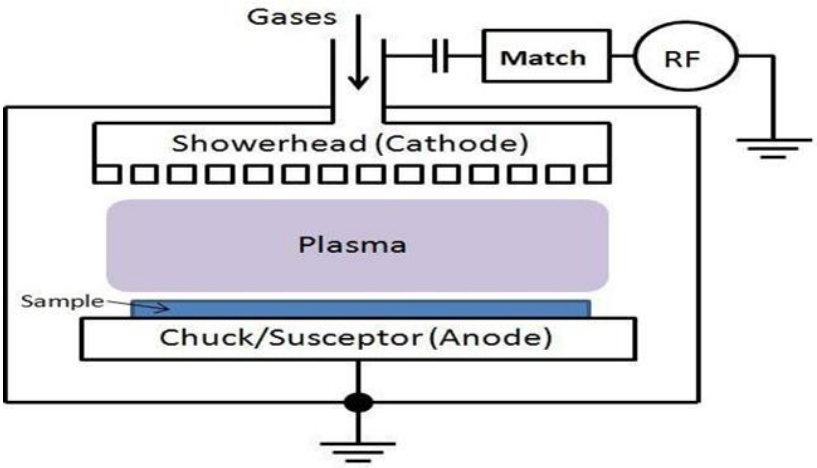

Figure 4-4. Schematic of PECVD.

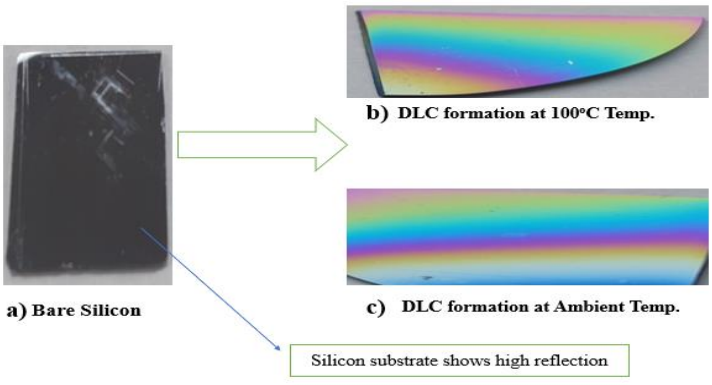

Figure 4-5. DLC deposited via PECVD technique. (a) Bare Silicon (b) DLC formation at 100 ^{0}C Temp (c) DLC formation at Ambient Temp.

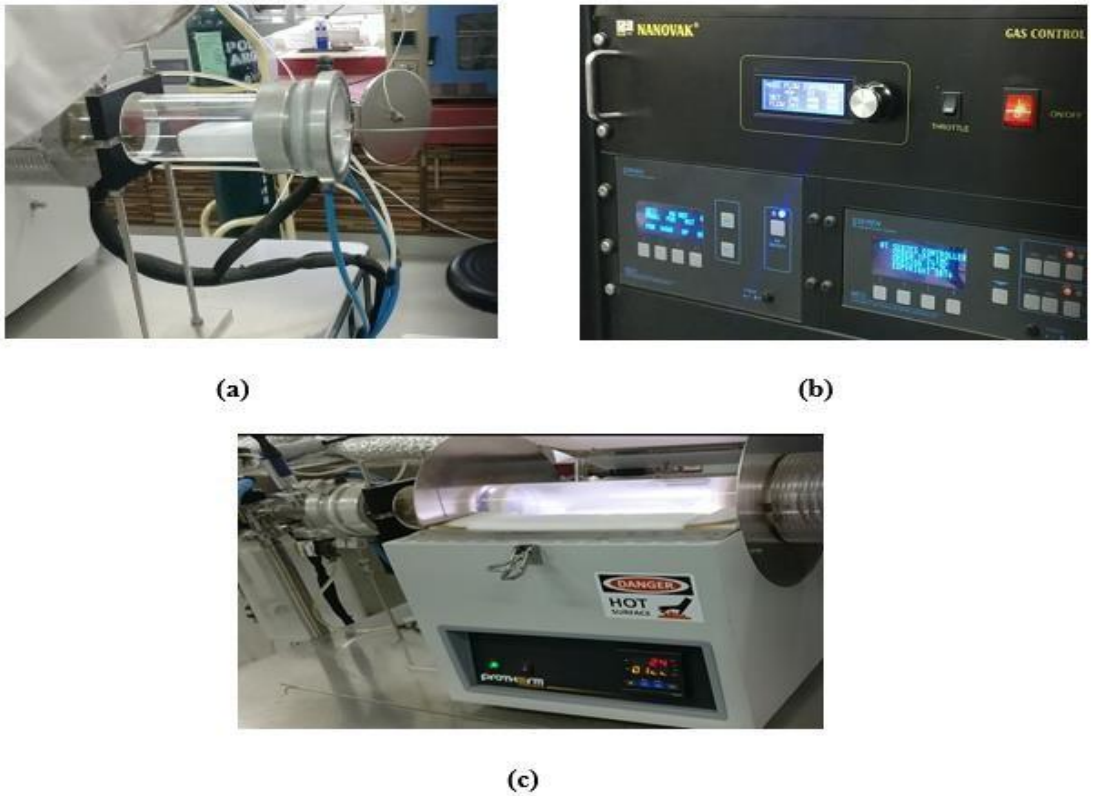

Figure 4-6. (a) Sample Adjustment inside the chamber. (b) Parameters adjustment during the experiment. (c) Plasma generation during the experiment

4.2.1.3 Characterization for PECVD deposited DLC film

The surface roughness and morphology of the film were analyzed by using the Scanning electron microscope (VEGA 3 LMU, TESCAN) and atomic force microscope (Nano surf Flex AFM with a C3000 controller). Structural characteristics of DLC film were observed by using Raman spectroscopy and FTIR (Agilent Cary 630). The Optical properties like absorption coefficient of the DLC film, reflectance, and transmittance were measured by using the ultraviolet-visible spectrometer. Contact angle measurement was carried out using a contact angle meter to get a better understanding of the wettability property of these materials (optical tensiometer).

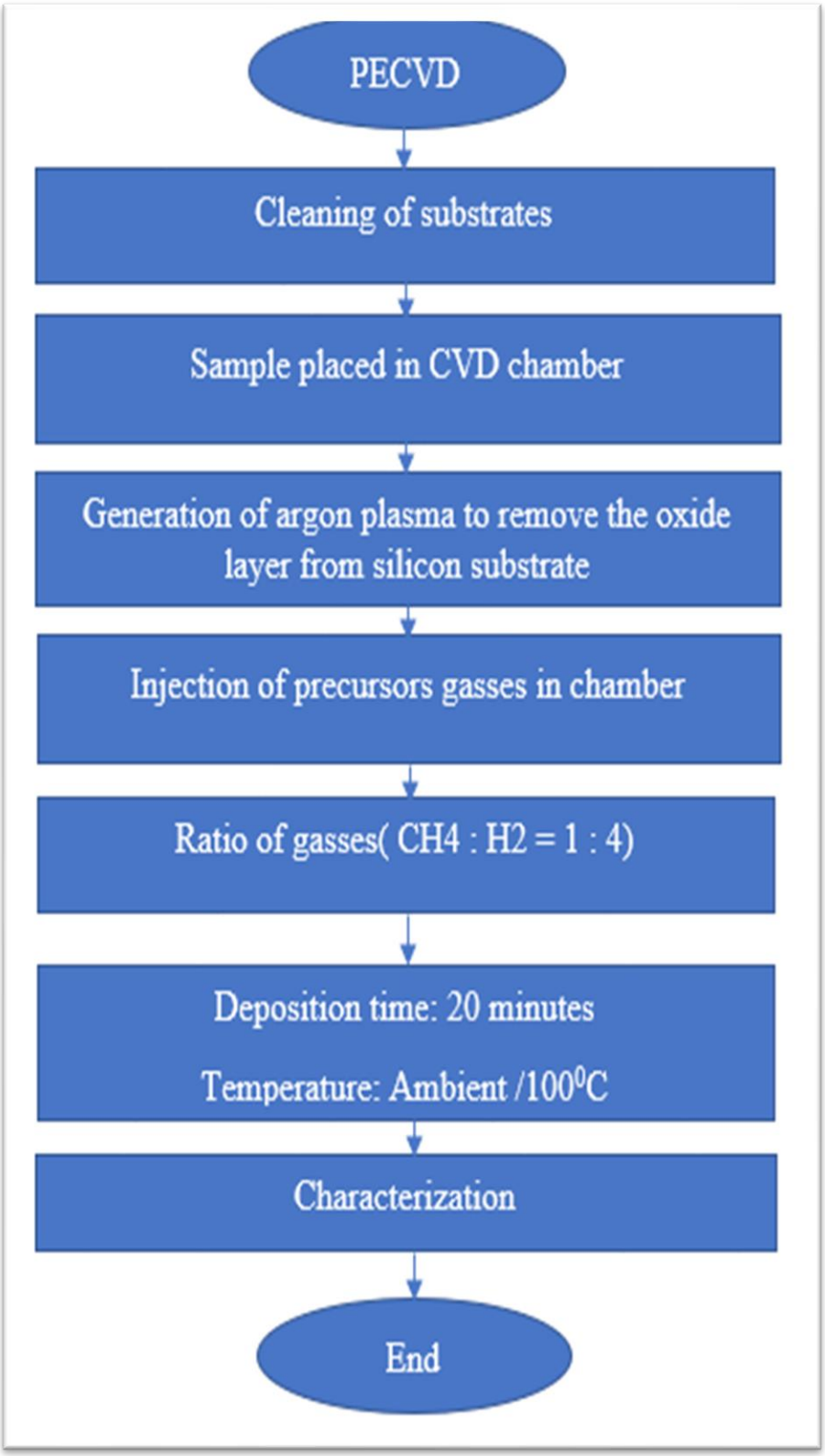

Figure 4-7. Flow chart to deposit DLC film via PECVD.

4.2.2 Electrodeposition Technique

4.2.2.1 Substrate Cleaning

Silicon and FTO coated glass were used as a substrate. Before Deposition, substrates were cleaned with cleaning solvents. First, substrates were cleaned with ethanol and acetone sequentially and then rinsed in Deionized water (DI) water to remove any contamination. To remove the oxides from the surface, silicon was cleaned with an HF solution. After cleaning with solvents and HF solution, the substrates were cleaned in the plasma cleaner.

4.2.2.2 Synthesis of DLC film by Varying Concentration of Acetic Acid in Solution

Materials and Method

Diamond-like carbon film was synthesized by the electro-deposition route. DLC film was deposited on the silicon substrate and conductive glass. Acetic acid and DI water are used as an electrolyte. Rubber is used as an insulator to separate the distance between the electrodes. A 300 volts DC power supply was used to apply potential. Copper wires were used as a connector with electrodes.

The graphite plate was mounted at the anode, and it acted as a counter electrode. Silicon substrate was mounted at the cathode and used as a working electrode. The separation distance of 7 mm was maintained between the electrodes. Before deposition, the silicon substrate was cleaned with acetone and ethanol sequentially and then rinsed in DI water. After cleaning with solvents, the oxide layer was removed by purging argon gas in plasma cleaner. 1.5 M acetic acid solution was used as an electrolyte. The deposition was carried out at room temperature and atmospheric pressure.

The voltage was kept fixed, and the concentration of the acetic acid was varied between 2% to 10%. The reaction was carried out at 2.7 V for 2 hours. To determine the effect of voltages, an experiment was also performed at different voltages by fixing the concentration of acetic acid shown in table 4-3 .

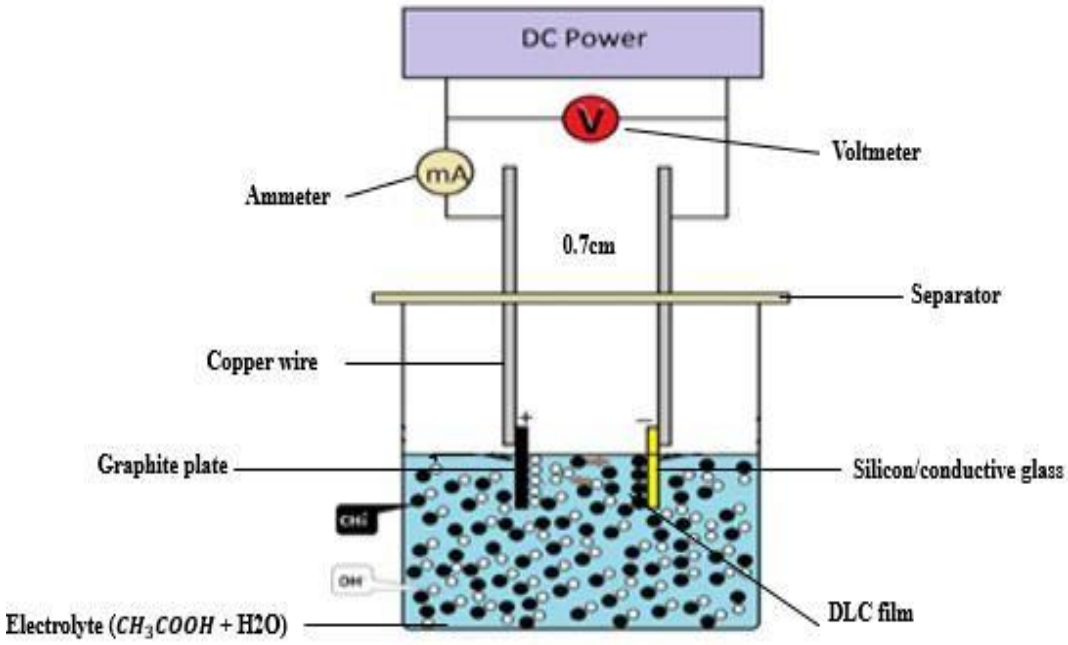

Figure 4-8. Schematic of Electrodeposition Setup.

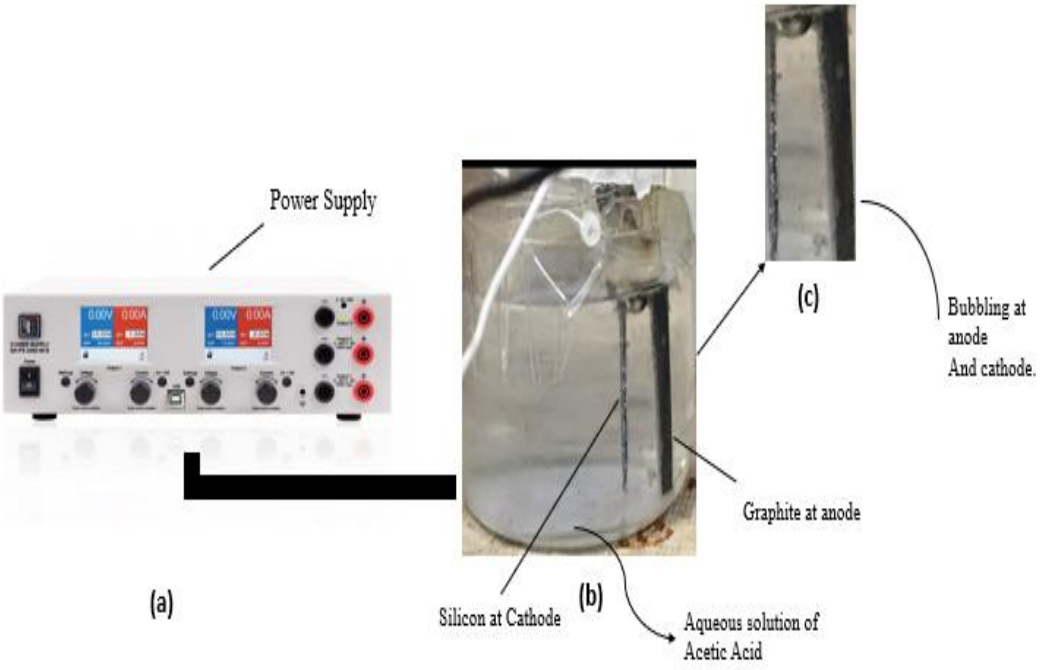

Figure 4-9. (a) Power supply capable to generate 300 V. (b) Aqueous Acetic Acid-based Electrolyte (c) Deposition at silicon substrate.

Deposition Parameters for DLC formation via Electrochemical route

Table 4-3. (a) Deposition parameters for fixed concentration and variable voltage.

Sr No.	Concentration of Acetic Acid (%)	Applied Voltage (V)	Temp. (°C)	Deposition Time (h)	Separation Distance (mm)
1		2.7			
2	2	4	Ambient	2	7
3		6			
4		8			
5		10			

Table 4-3. (b) Deposition parameters for fixed voltage and variable concentration of acetic acid.

Sr No.	Concentration of Acetic Acid (%)	Applied Voltage (V)	Temp. (°C)	Deposition Time (h)	Separation Distance (mm)
1	2				
2	4	2.7	Ambient	2	7
3	6				
4	8				
5	10				

4.2.2.3 Characterization of electrodeposited DLC film

Surface morphology was analyzed by using the Scanning electron microscope (VEGA 3 LMU, TESCAN). Structural characteristics of DLC film were observed by using Raman spectroscopy by using 532 nm laser and FTIR (Agilent Cary 630). The Optical properties like absorption coefficient of the DLC film, reflectance, and transmittance were measured by using the ultraviolet-visible spectrometer. Optical microscopy was used to analyze the morphology after deposition at different voltages.

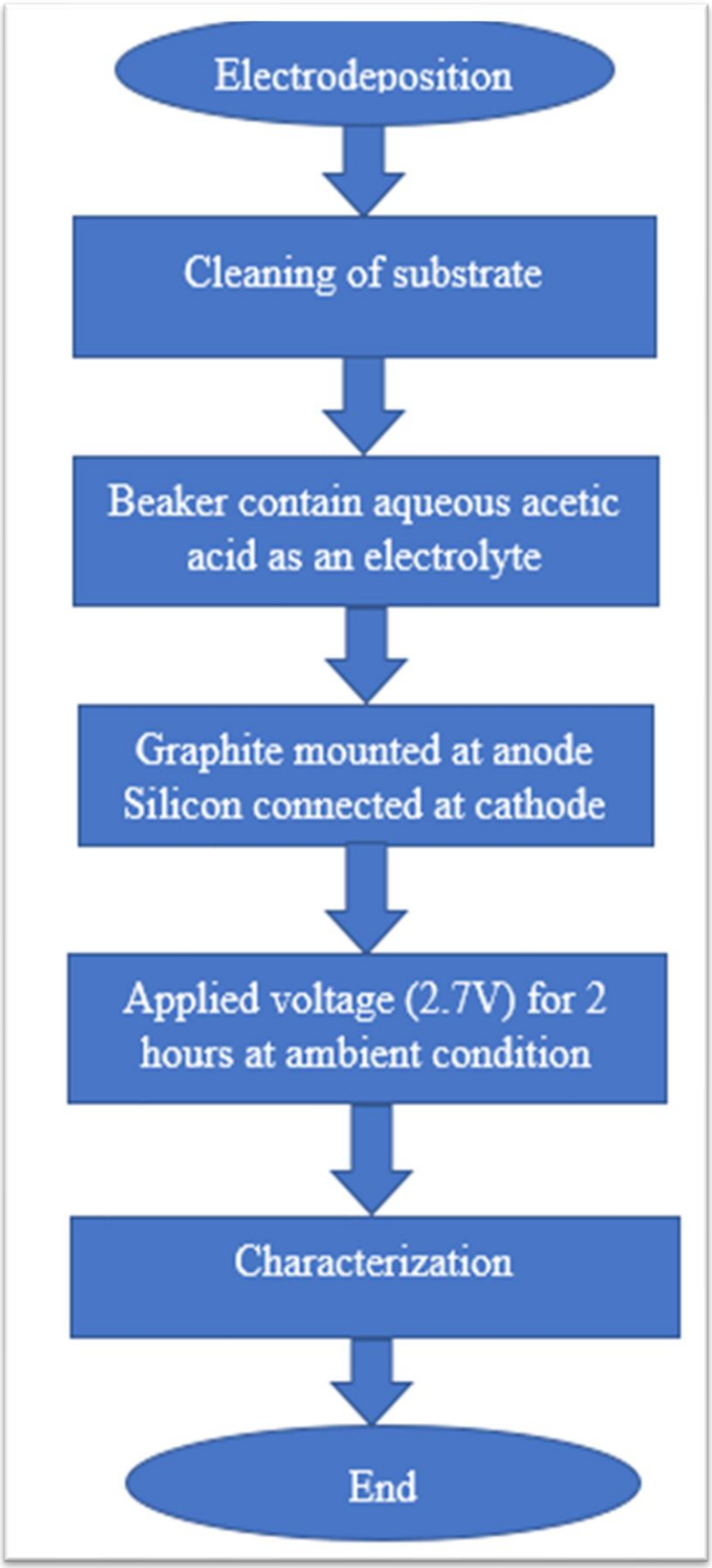

Figure 4-10. Flow chart to deposit DLC film via Electrodeposition Technique.

Summary

This chapter is basically about the development and process experimentation of antireflection-based materials, i.e., Dimond-like carbon film, Zinc Oxide, and Lanthanum doped ZnO thin film for solar cell application. Lanthanum-doped ZnO thin film was deposited through the sol-gel and spin coating technique. We employed two different methods to fabricate the DLC film, i.e., Plasma Enhanced Chemical Vapor Deposition and Electrodeposition. In each experimentation, Silicon wafer, Soda-lime glass, FTO coated glass, and Tin oxide coated glass was used as substrate material. First, clean the substrate with the cleaning solvents and in plasma cleaner to remove any type of contamination from the surface of the substrate. In the formation of ZnO and La-doped ZnO thin film, Zinc Acetate Dihydrate, and Lanthanum nitrate Hexahydrate as a Precursor material. The concentration of Lanthanum into ZnO was varied up to 1 at. % to 3 at. %. Annealing Temperature of all the synthesized films of ZnO and La-doped ZnO was fixed at 450 ^{o}C, and the ramp was kept at 3 ^{o}C/min. In the PECVD technique, we used methane and hydrogen as precursor gasses to develop the hydrogenated carbon-based film. We performed two trials at different temperatures to optimize the AR properties of DLC film. The first experiment was performed at room temperature and the other one at 100 ^{o}C to analyze the effect of substrate temperature on the DLC film. Electrodeposition was another technique to deposit DLC film on the silicon and conducting glass substrate. Acetic Acid and DI water was used as an electrolyte to fabricate the hydrogenated carbon-based film. In which, Concentration of Acetic acid and variation in the voltage was applied during the whole experimentations of the electrodeposition. All the depositions were carried out for the optimization of antireflection properties.

Chapter 5: Results and Discussion

5.1 Characterization of La-doped ZnO film synthesized via Sol-gel

5.1.1 Phase Analysis of Pure and La-doped ZnO film (XRD)

XRD was utilized to analyze the ZnO and La-doped ZnO crystal structure. In crystal structural analysis, crystallite size, phases, and lattice parameters have been determined. ZnO and lanthanum-doped ZnO thin film diffract X-rays because they are made up of a periodic array of long-range organized atoms. The X-rays scattered by atoms in a ZnO carry information about the material's atomic organization. ZnO has distinct peaks in the range of 20-80^{o}. All the doped and undoped ZnO thin films are crystallized after annealing at constant temperature 450^{o}C and kept the ramp at 3^{o}C/min. Multiple peaks can be seen in a single diffraction pattern of the material. films exhibited peaks at around 31.7^{o}, 34.3^{o}, 36.3^{o}, 47.4^{o}, 56.6^{o}, 62.7^{o,} and 67.8^{o}, which corresponds to (100), (002), (101), (102), (110), (103), and (112) planes of ZnO (JCPDS Card No. 36-1451) respectively.

The number of peaks and their relative intensity are determined by the material's crystal structure. The structure of a crystal is defined by its unit cell, whereas the shape of the unit cell is described by a crystal system. Different planes of atoms are identified by Miller indices (hkl). X-ray diffraction wavelength λ falling on a family of parallel atomic planes, constructive interference occurs only at a specific angle.

$$n\lambda = 2d \sin\theta \qquad (5.1)$$

Where, n is a positive integer, which indicates the inter-planar distance between two adjacent planes of the (hkl) family.

Furthermore, inter-planar spacing (d) using equation (5.2) and lattice parameter was calculated by Bragg's formula given in the following equation.

$$\frac{1}{d^2} = \frac{h^2+k^2+l^2}{a^2} \qquad (5.2)$$

Where, n is a positive integer, which indicates the inter-planar distance between two adjacent planes of the (hkl) family. Furthermore, inter-planar spacing (d) using equation (5.2) and lattice parameter was calculated by Bragg's formula given in the equation.

The crystallite size is calculated using full width half maxima of the characteristic XRD peaks using the Scherer formula

$$D_S = \frac{0.9\lambda}{\beta \cos\theta} \qquad (5.3)$$

D_S is crystallite size.

where λ shows the wavelength of the X-Ray which has a constant value of 1.54.

θ is Bragg diffraction angle.

β represents full width at half-maximum (FWHM) in radians.

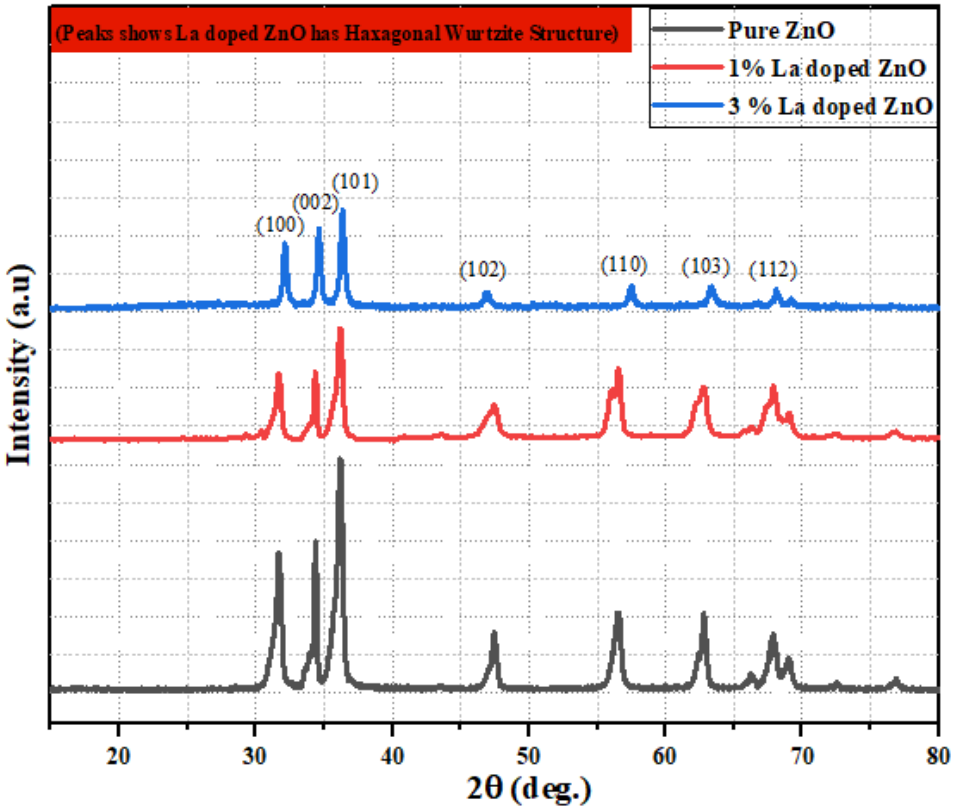

Figure 5-1. XRD graph for Pure ZnO and La-doped ZnO.

Table 5-1. Crystallite size analysis of Pure and La-doped ZnO.

Sr#	Samples	d(A^0)	(hkl)	Crystallite size (nm)
1	Pure ZnO	2.481	(101)	34 nm
2	1% LZO	2.478	(101)	31 nm
3	3% LZO	2.473	(101)	27 nm

After doping of the Lanthanum into ZnO, then there is some shift of 0.08^{o} in 2θ that shows some variation in the crystal structure. The crystallite size of the synthesized ZnO thin film decrease as increasing the doping level of lanthanum content inside the ZnO lattice. This could be happened due to the inhibition of the Lanthanum cation to the crystal growth of zinc oxide. The inhibition is directly associated with the distortion of the crystal lattice due to the high ionic radii of the lanthanum (1.15 A˚) as compared to the zinc cation (0.74 A˚). During the process of doping, its very difficult to find the crystal phase of the lanthanum oxide because a lot of phases with in the structure and their classical XRD peaks are very close to each other [1].

5.1.2 Functional & Structural Analysis of La-doped ZnO film (FTIR)

The functional group and structural study of the Zinc Oxide thin-film material were investigated using the FTIR technique. As shown in figure 5-2; FTIR results reveal that before annealing there was an intense peak of carbon, hydrogenated carbon, and O-H at 1125 cm^{-1}, 1340 cm^{-1}, and 1556 cm^{-1}, due to the occurrence of stabilizers such as Ethanolamine (EA), solvents like methanol and ethanol. The presence of ZnO and Lanthanum doped ZnO materials bond was in the range between 400 cm^{-1} to 650 cm^{-1}. These results are much correlated to the previous findings.

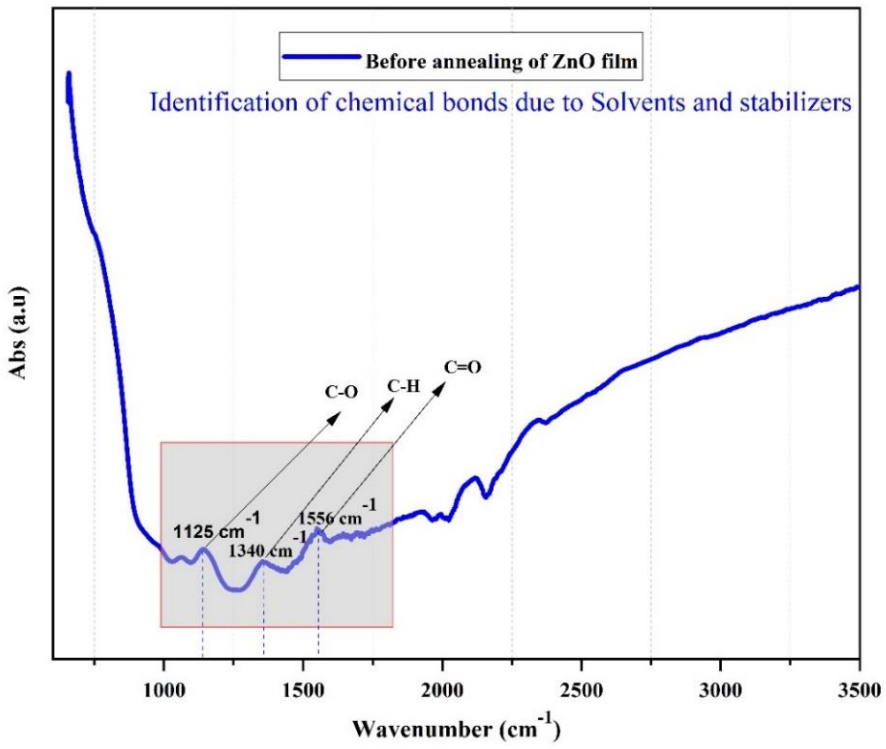

Figure 5-2. FTIR spectra for ZnO thin film before Annealing.

After Annealing at 450 ^{o}C, there was low intense peak of carbon and C-H on the FTIR spectra because the evaporation point of stabilizer and other solvents is below 400 to 450 ^{o}C. The peak after annealing validates that there were little presence hydrogenated carbon bonds in the ZnO thin film after the heating treatment due to hydrogen defects inside the ZnO lattice. Only wurtzite ZnO and Lanthanum doped ZnO thin film was left behind after the annealing.

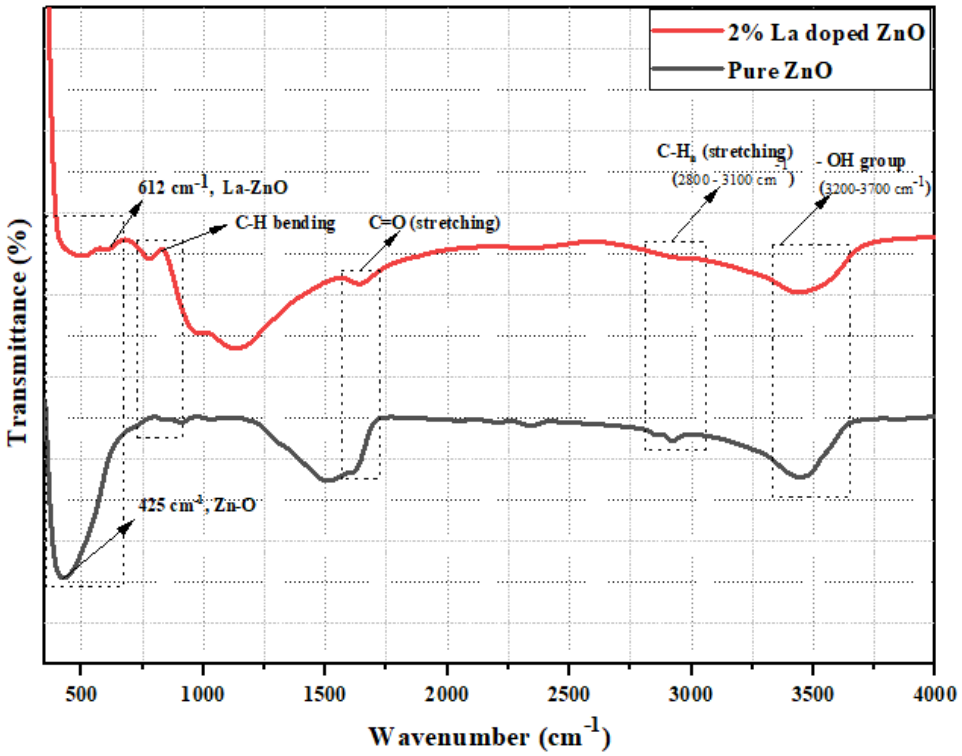

Figure 5-3. FTIR spectra for ZnO thin film after Annealing.

5.1.3 Microstructural Analysis of La-doped ZnO film (Raman Spectroscopy)

Raman scattering is a non-destructive and sensitive characterization technique that is used to investigate the vibrational characteristics of nanostructured materials.

It is utilized to clarify the quality and structure of ZnO thin films in this case. ZnO of the Wurtzite type with relation to C4. The primitive cell has a 6v (P63mc) space group with two formula units, resulting in 12 branches of phonons (9 opticals and 3 acoustics). The irreducible representation, according to group theory, and for a perfect crystal structure [2].

The number of optical phonons in the Brillouin zone is given as:

$$\mathbf{I_{opt} = A1 + E1 + 2E2 + 2B1} \qquad (5.4)$$

In Raman scattering, B1 modes are quiet, while E2 modes are nonpolar and Raman active. Because A1 and E1 modes are both Raman active and infrared active polar, they display two properties as Transverse optical (TO) and longitudinal optical (LO) phonon frequencies. This mode is mostly caused by oxygen atoms moving perpendicular to the c axis of ZnO and any change in bond bending generated by tension along this axis created a shift of the phonon E_{2H}.

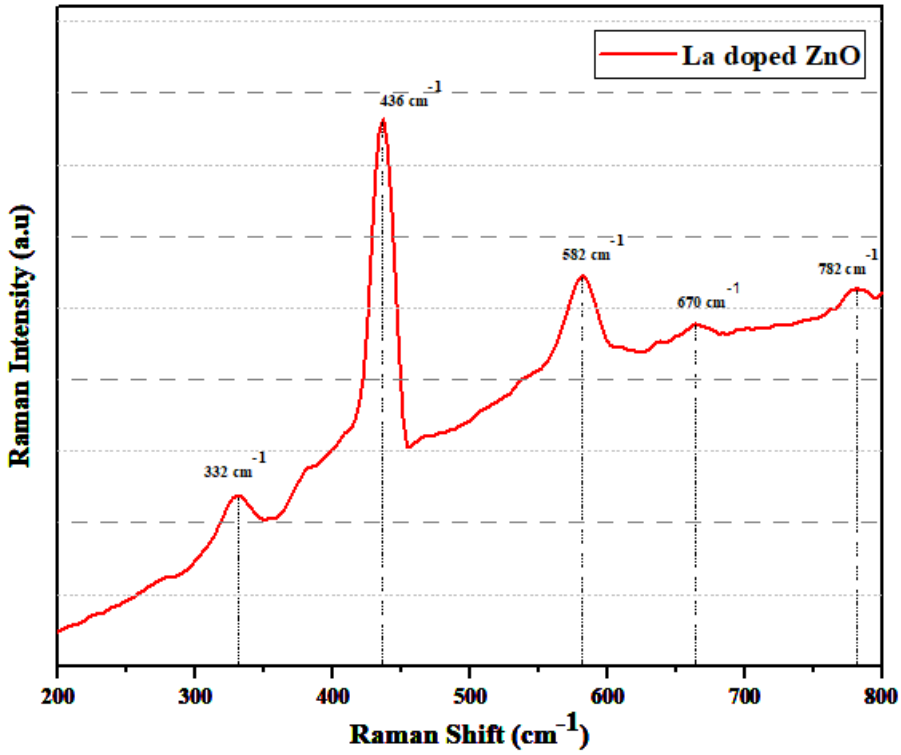

Figure 5-4. Raman Spectra for the 2% La-doped ZnO Thin Film.

There are many additional elements to consider, such as phonon confinement and Temperature changes that may induce a considerable shift in the Raman peak location. There is a further rise in the E_{2H} phonon frequency (moving up or down) after La doping. As compared to the prior discovery of simple ZnO, indicating that supplemental doped samples, compressive stress was introduced. The weak summits are found around 332 cm^{-1} and 670 cm^{-1}. The highest point 436 cm^{-1} is the location is attributed to the second-order Raman (E_{2H}) mode, which is a common mode. A property of wurtzite ZnO, there are also two extra modes at 582 and 782 cm^{-1} surfaces optical (SO) phonon modes that were identified in the ZnO Raman spectra.

5.1.4 UV-VIS NIR Analysis of La-doped ZnO film (UV-VIS NIR Spectroscopy)

Optical analysis of the synthesized films of ZnO and Lanthanum doped ZnO was done by using the UV-Vis NIR spectrophotometer. Transmission(T) and Absorbance graphs depict the percentage transmission and absorbance of light into the material. Absorbance is calculated by using the formula.

$$\mathbf{A\% + T\% + R\%=1} \quad (5.5)$$

$$\mathbf{A\% = 1 - T\% - R\%} \quad (5.6)$$

The wavelength region is set in the range from 300nm to 1200nm to determine the optical response of the desirable material deposited over the Soda-lime glass. The average transmission calculated from the UV-Vis NIR spectrophotometer is in the range of >92% in the visible region.

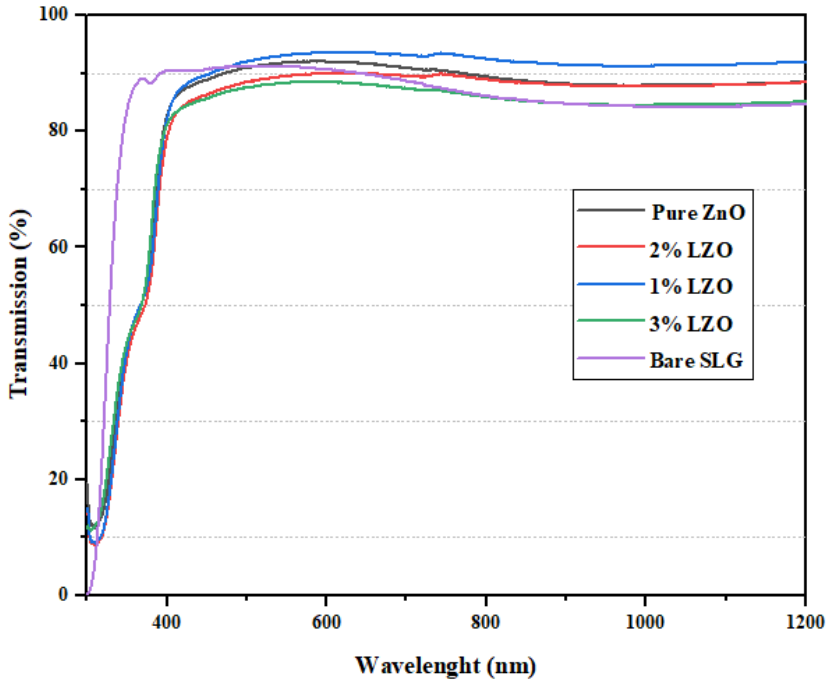

Figure 5-5. Transmission spectra of Pure and La doped ZnO thin film.

The transmission was first increased after doping of lanthanum inside the ZnO thin film and then decrease after doping of lanthanum at 2% and 3 %. The sharp absorption band edges of the synthesized ZnO and Lanthanum doped ZnO thin film are in the range of 390nm. High transmission and absorption edges are attributed to the small scattering effect resulting from the structural homogeneity of the films and the apparent high crystallinity [3]. This is due to the film the highly oxidized and no defect has been

found in ZnO and doped ZnO thin film. The reason for the widening of the bandgap after doping of lanthanum is due to the phenomena of the Moss-Burstein effect.

Table 5-2. Comparison of Average Transmission of light at various regions.

Sr#	Concentration of La-doped ZnO thin film	Visible region (Avg transmission %)	IR region (Avg transmission %)
1	Bare SLG	89.79072	84.69636
2	Pure ZnO	90.61498	88.3033
3	1% LZO	92.28879	91.63726
4	2% LZO	88.73922	88.11275
5	3% LZO	87.18378	84.89879

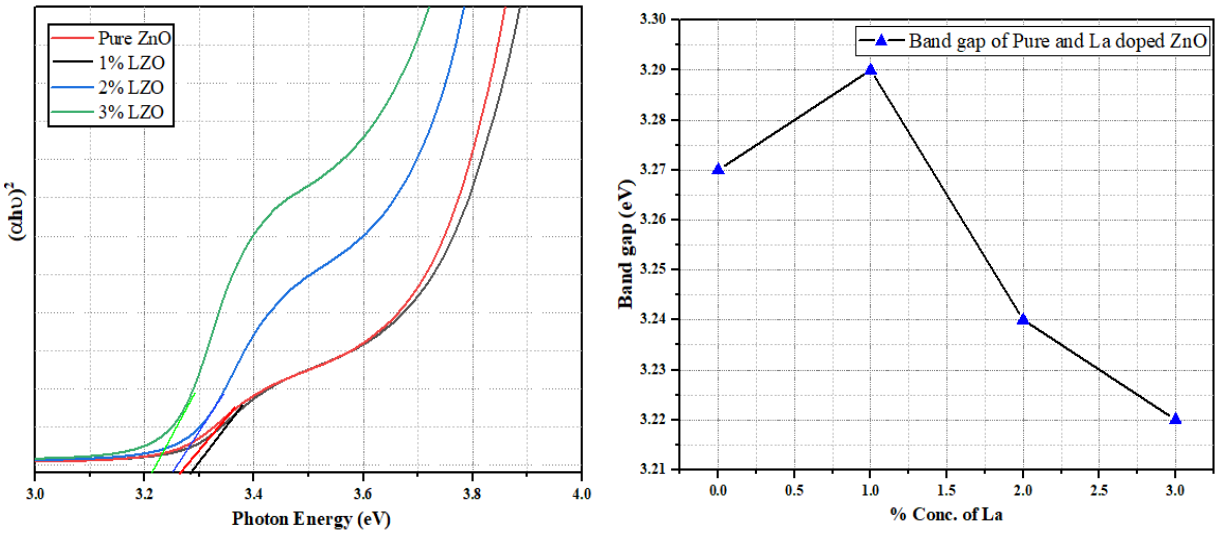

(a) (b)

Figure 5-6. (a) depicts the Absorption spectra of ZnO and Lanthanum doped ZnO thin films. (b) shows the effect of doping on Bandgap.

The widening of the bandgap is also related to the particle size and lattice parameter. As the decrease in the particle size of the 1% of lanthanum doped ZnO thin film shows

the high bandgap as compared to the other doped samples at 2 and 3 at. % this is due to quantum refinement effect. Whereas the increase in the lattice parameter after 2 and 3 % doping of lanthanum inside the ZnO thin film decrease the bandgap of the synthesized film, this is due to the decrease of the interaction of atoms with each other.

5.1.5 Hall Measurements of La-doped ZnO film (Hall Effect)

Fig. 5-7. shows the electrical resistance fluctuation with La concentration. La-doping reduces and marginally enhances film resistance.

The film with a genuine La content of 2% has a minimum resistance of 3.36×10^2 Ω.cm. Electrical conductivity might be increased because of the increased carrier concentration introduced by the La^{+3} cation. Additionally, this might signify that the films seem to be n-type conductive.

The conductivity of ZnO rises as the concentration of Lanthanum in the material increases. The substitution of Lanthanum ions for Zinc ions may increase the concentration of charge carriers in the synthesized film.

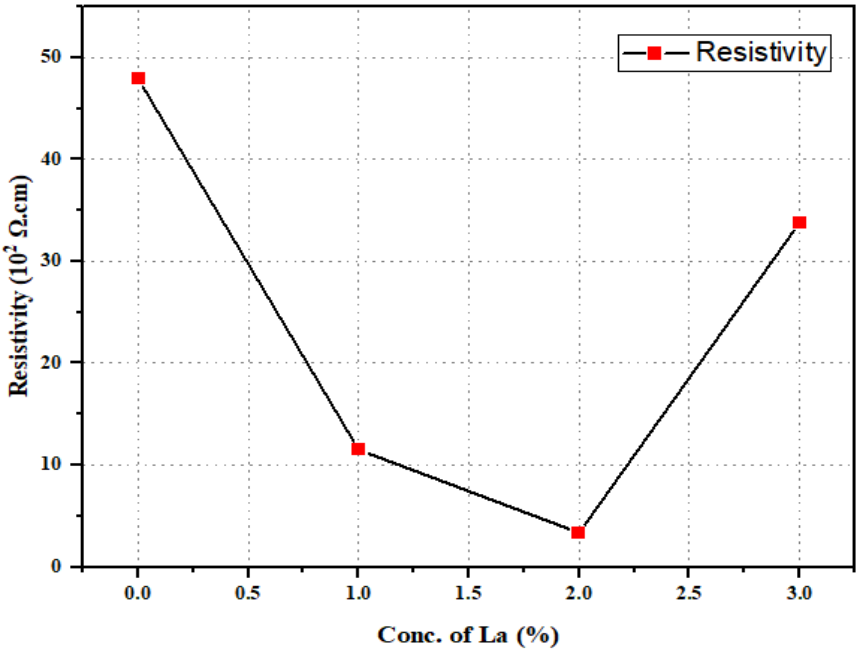

Figure 5-7. Resistivity of Pure ZnO & Lanthanum doped ZnO Thin film.

Electrical properties of the pure ZnO thin film and lanthanum doped ZnO were analyzed by using the hall effect. Bulk concentration, Conductivity, Resistivity, and semiconductor type were determined by using this technique. For pure ZnO, the carrier concentration was 1.8 x 10^{13}, for lanthanum doped ZnO it was 1.2x10^{15}, so that the

bulk concentration has increased by one to two order times as compared to pure ZnO thin film. Due to doping of Lanthanum in the ZnO lattice structure free carriers are generated which increase overall bulk concentration.

Table 5-3. Hall Measurements of ZnO and La Doped ZnO at different concentration level of doping.

Sample	n_H (cm^{-3})	ρ (10^2 Ω.cm)	σ (10^{-3} 1/Ω.cm)	Type
Pure ZnO	1.8×10^{13}	47.7	0.12	n-type
1% LZO	8.6×10^{14}	21.5	0.39	n-type
2% LZO	1.2×10^{15}	3.36	1.25	n-type
3% LZO	3.3×10^{14}	10.5	0.208	n-type
NOTE: n_H- Bulk Concentration, ρ-Resistivity, σ-Conductivity.				

As the concentration of carriers increased, the conductivity of the synthesized ZnO film also enhanced as shown in table 10. The conductivity of 2% lanthanum doped ZnO was reported as 1.25 x 10^{-3} S/cm, which lie well within the range of semiconductors. It is more than pure ZnO which is attributed due to the large presence of free carriers. The Hall Coefficient of both the samples was negative, therefore they are n-type semiconductors.

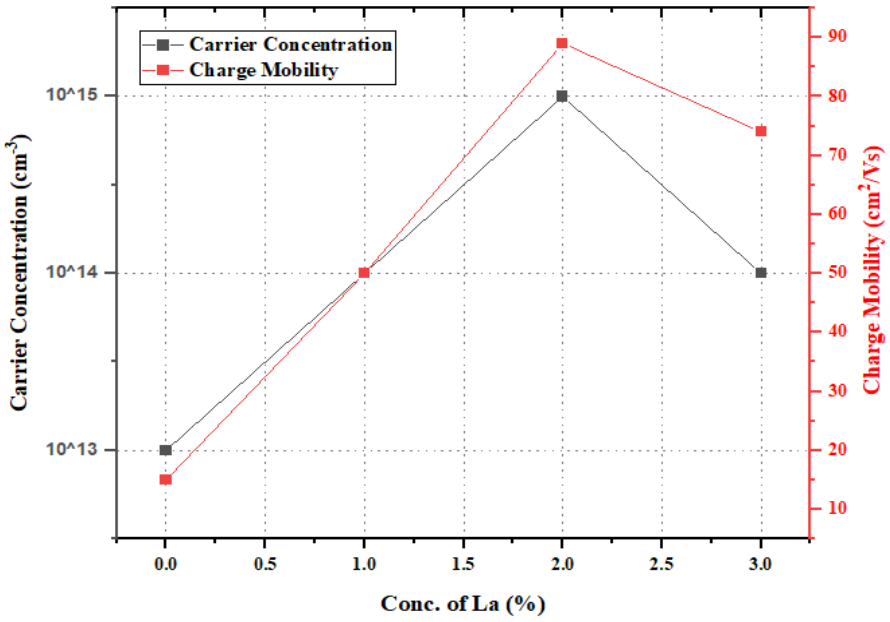

Figure 5-8.: Relation between carrier concentration, charge mobility and conc. of lanthanum in ZnO.

This might have been attributed to the electron-impurity interaction and the Coulomb interaction between the carriers, which both contribute to the decrease in optical transmittance and electrical conductivity seen with increased La concentration [4].

5.1.6 Water Contact Angle (WCA) measurement

In this study, water contact angles CA were obtained by profiling symmetrical droplets of water on the ZnO and lanthanum doped ZnO thin film's horizontal surface. The Drop Shape Analysis of the System type DSA100 was used for the measurements (Kruss GmbH, Hamburg). A needle was used to insert the sample beneath the tip of the needle. This needle was connected to a computer-controlled micro syringe pump that delivered the deionized water drop (about 2.5 microliter) to the film surface. A video camera was used to collect time-lapse photos of the drops, and image analysis of the contact angle (and other drop characteristics such as surface free energy and adhesion work) was conducted using the instrument's DSA3 software.

Contact angles were determined by fitting the sessile drop's form to the circle equation and then computing the slope of the tangent to the drop at the liquid-solid vapor interface line. It was the average of the left and right angles of each drop that was utilized for calculations or comparisons between various samples of varied sizes. For more accuracy, water was dropped onto at least three separate locations on each sample, and the average of the observed values was reported as the final CA. Mechanical vibration and airflow were avoided at all costs throughout the examination.

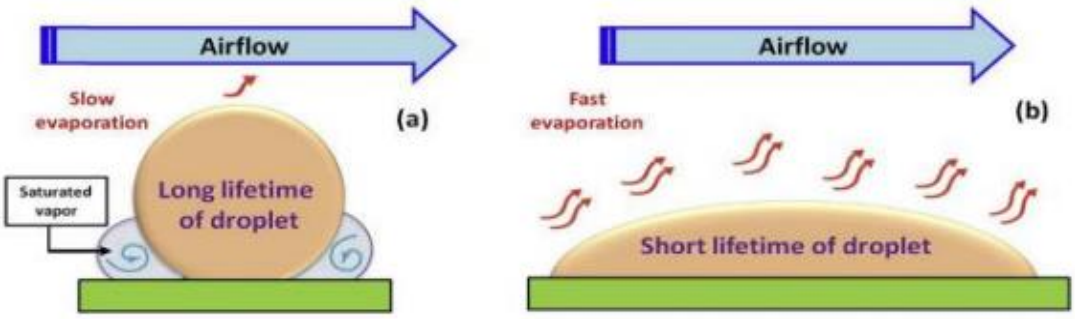

Figure 5-9. Water evaporation mechanism schematic diagram (a) Hydrophobic (b) Hydrophilic.

As can be seen in the illustration, the form of water droplets on various materials demonstrates the two sorts of states (hydrophilic and hydrophobic) that exist. Furthermore, Fig. 5.9, which depicts the development of contact angles over time,

reveals a decreasing tendency, which may be explained by the slow evaporation of the droplets after they have been deposited on the surface of the samples.

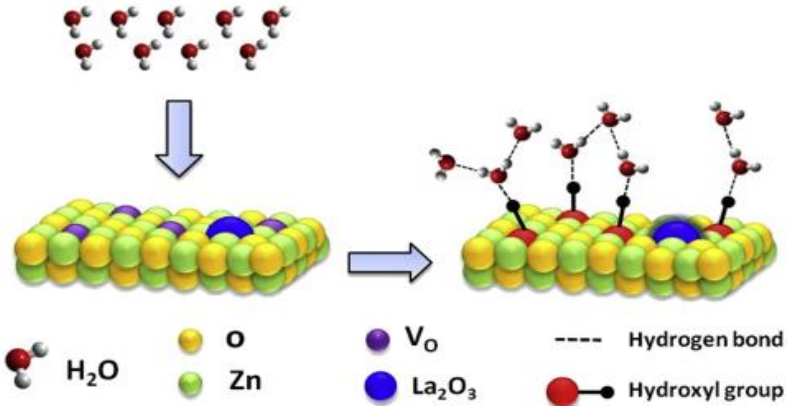

Figure 5-10. Schematic diagram showing water adsorption mechanism on La-doped ZnO surface.

Undoped ZnO has a hydrophilic surface with a contact angle of 73º. We observed that when the La content is between 1 and 2%, the contact angle reduces, and the surface becomes more hydrophilic.

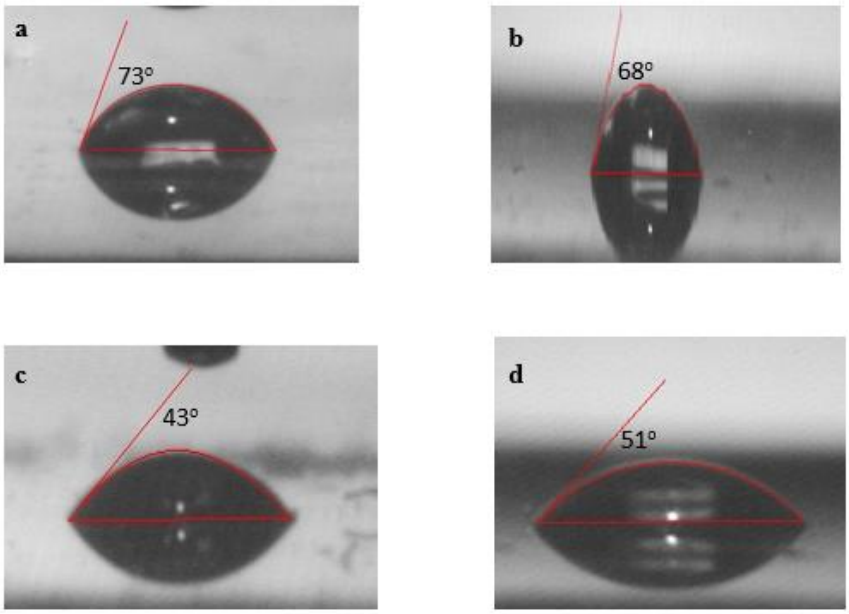

Figure 5-11. (a) Pure ZnO having WCA 73º (b) 1% La-doped ZnO having WCA 68 º (c) 2% La-doped ZnO having WCA 43 º (d) 3% La-doped ZnO having WCA 51 º

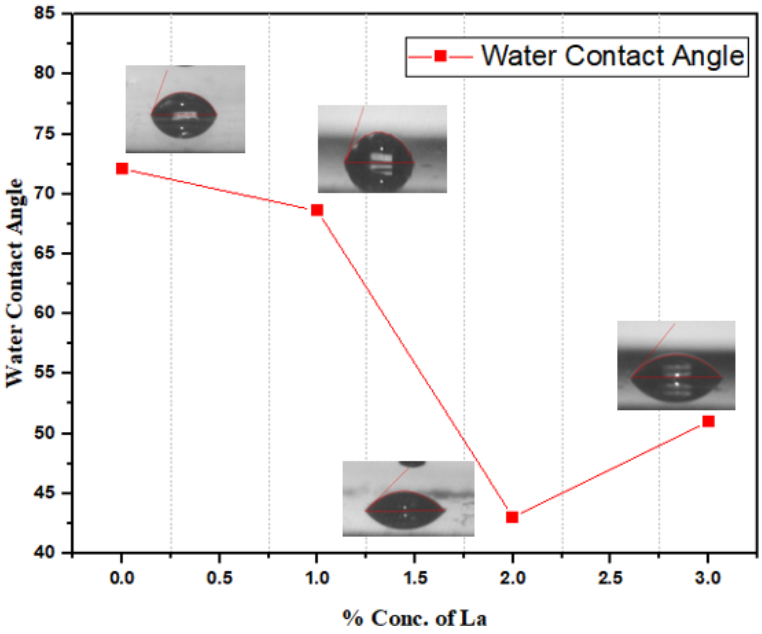

Figure 5-12. Analysis of wettability of ZnO & La-doped ZnO Thin film.

Both adhesion work and surface free energy increase with doping amount during this initial stage. It is self-evident that a low surface free energy correlates to a poor adhesive contact between water and the ZnO surface (low Wad), resulting in a low hydrophilic character (Angle = 73^{o}) as compared to other samples.

On the other hand, the hydrophilic condition of a surface indicates that the water adheres well to it and is acquired by a high surface free energy. Both rates (1 and 2%) seem to be favorable for increasing the active groups capable of forming hydrogen bonds with water and therefore increasing the wettability and making the surface more hydrophilic. This behavior occurs when the surface chemistry lacks active groups capable of forming hydrogen bonds with water [5].

5.2 Characterization of DLC film synthesized via Electrodeposition

5.2.1 Reaction Mechanism

An assortment of apposite electrolytes for the DLC formation by using the electrochemical approach would highly be dependent on the dipole moment and dielectric constant of the electrolyte. Dipole moment signifies the basic ionic nature while the strength of the electric field between the anode and cathode indicates by the dielectric constant. A solution of acetic acid (σ; 1.74×10^{-18} esu, ε; 6.15) and water (σ; 1.87×10^{-18} esu, ε; 80.37) appeared like the right choice for the selection of electrolyte

meanwhile the comparative values mentioned above can be changed by varying the concentration of water and acetic acid.

Overall Reaction:

$$CH_3COOH \rightarrow CH_3^+ + CO + OH^-$$

Cathode Reaction

$$2CH_3 + 2e^- \rightarrow 2C + 3H_2$$

Anode Reaction

$$2OH^- \rightarrow O_2 + H_2O + 4e^-$$

During the electrolysis, the aqueous solution of acetic acid was converted into the methyl ions and gaseous form of carbon monoxide. Different hybridized form of carbon has been formed on the substrate surface. There is the formation of water and oxygen at the surface of the anode while depositing OH^- ions.

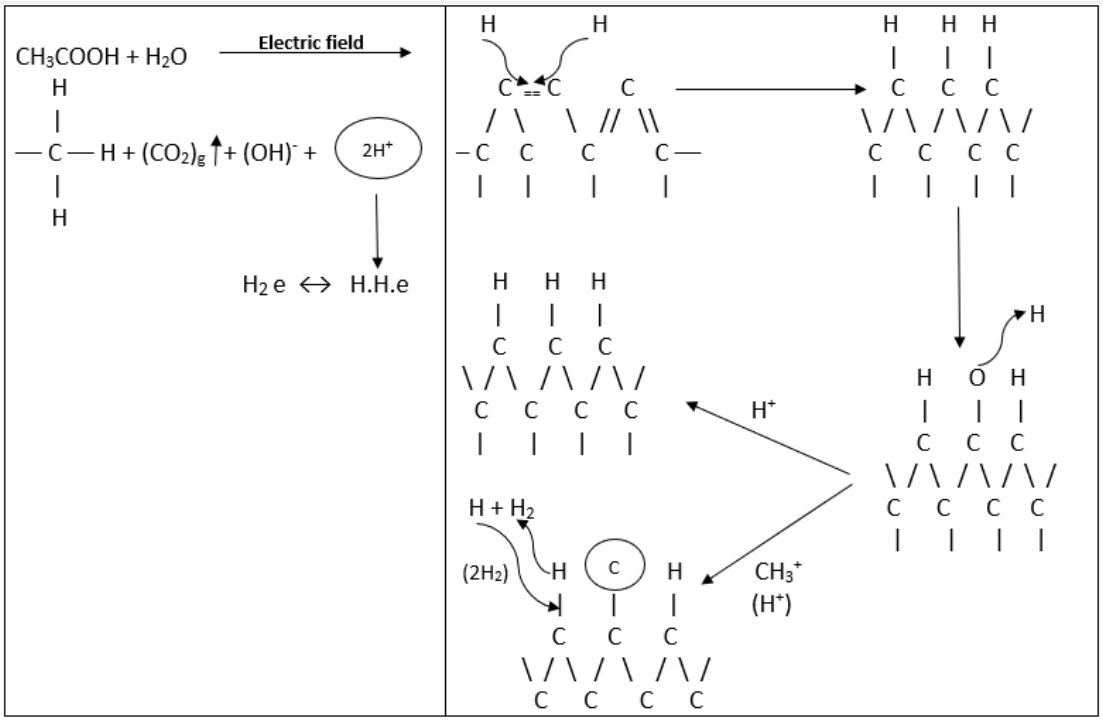

Figure 5-13. Reaction mechanism of DLC formation over the surface of the substrate by using aqueous acetic acid as an electrolyte [6].

Under an electric field, the aqueous solution of acetic acid tends to ionize. The large concentration of methyl radicals and H_2 ions is deposited at the surface of the cathode during the process of electrolysis. The major prerequisite to depositing diamond like Carbon film and diamond films, deposition of high concentration of hydrogen ions and methyl radicals at the surface of the substrate must be satisfied.

5.2.2 IV curve of Electrolytic Bath (Threshold Value for Conduction)

Fig. 5-14 shows the I–V characteristic of the electrolytic bath. It can be observed that the electrolytic conduction starts at 1.2V. After increasing the voltage, the deposition current increase exponentially and the rate of deposition was also increased. In the previous studies, S**.** Gupta, R.L. Rahini et al. used the acetonitrile and DI water as an electrolyte, they observed that current density increases exponentially after the threshold voltage of ~12V. Current density increases by increasing the voltage and then the deposition rate is also enhanced because a large number of ions move towards the working electrode [7].

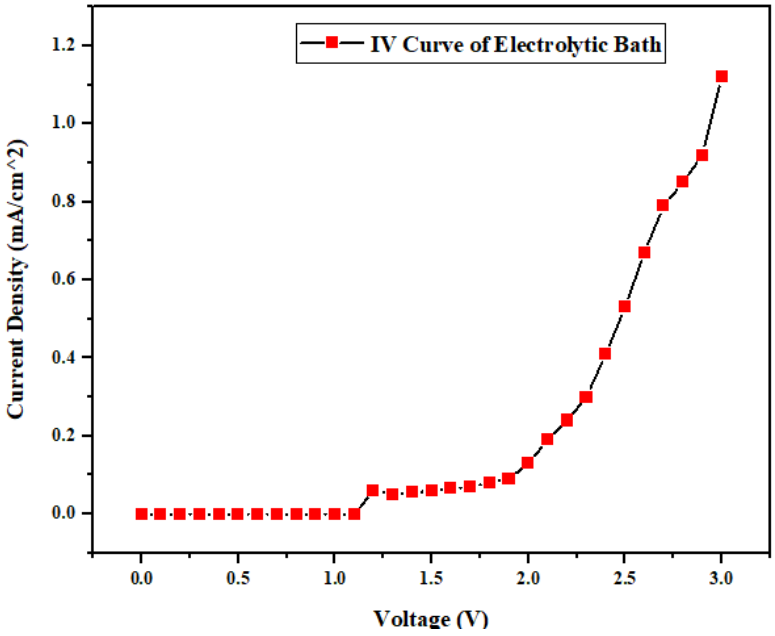

Figure 5-14. Threshold value (I-V characteristic of the electrolytic bath at 2% concentration of Acetic acid.) to start conduction.

5.2.3 Morphological Analysis of DLC film (SEM & EDS)

A scanning electron microscope was used to determine the morphology of the DLC film. Fig.5-15 (a & b) shows the morphological information about the DLC film. It was

clearly observed that the film was rough, and the roughness was increased by increasing the concentration of acetic acid in water. Small and compact grains were obtained at 2% (v/v) and 4% concentration of acetic acid in water as compared to the higher concentration of acetic acid. We observed that the film was uniform and well defined at a lower concentration of acetic acid. Table 5.4. clearly shows that at a lower concentration, less carbon is deposited as compared to a higher concentrated solution of acetic acid. During the electrolysis of the aqueous solution, a large amount of methyl radicals and hydrogen ions were deposited because the concentration of acetic acid was high that have enough content of carbon as compared to the lower concentrated aqueous solution. This result is much co-related to the previous literature. R. Paul et al observed that at lower concentrations of acetic acid, small and compact grain was obtained [8]. They also concluded that the roughness of the film was increased as increase the acetic acid concentration in the solution. Q. Zhang et al. used the chloroacetic acid aqueous as an electrolyte to deposit DLC film on the SnO_2 coated glass. He also observed that the film was quite smooth, uniform and had compact grains at the lower concentrated solution of chloroacetic acid and voltage level [9].

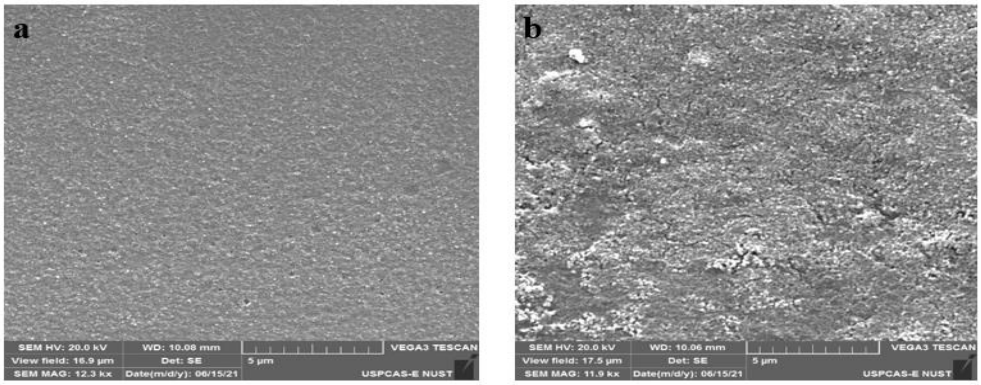

Figure 5-15. SEM images of DLC film formation at different concentrations of acetic acid in an electrolytic bath. (a) 2% and (b) 10%

Table 5-4. EDS Data for DLC film at different conc. Of Acetic Acid

Sr No.	% Conc. Of Acetic Acid	Elements	Atomic %age.
1	**2%**	Carbon	27.68
		Oxygen	2.79
2	**10%**	Carbon	69.77
		Oxygen	15.5

5.2.4 Effect of voltage on the DLC film formation (Optical Microscopy)

As shown in Table 5-5. DLC film was deposited at different voltages from 2.7 V to 10 V and a fixed concentration of acetic acid. As shown in SEM images; DLC film is quite uniform and has compact grains at 2.7 V. The deposition of DLC film at 4 to 10 volts has the formation of clusters and the size of clusters increase by increasing the voltage up to 10V. As shown in the literature; greater hydrogen content was found in the lower voltage, lower deposition temperature. Ching-Tsang Chang et al. observed in the FTIR analysis that greater hydrogen content was found in the lower voltage and no hydrogen was observed at high temperature and voltage level. Hydrogen atoms terminate the dangling bonds of carbon so that's why hydrogen in the DLC film has importance to enhancing the optical properties of the DLC film.

Deposition from organic liquid source mostly carried out at high voltage (400-3000 V) and marginally higher than room temperature. At high voltage, the organic liquid near the electrode walls starts to boil. Tosin et al. studied the effect of liquid boiling near the electrode walls during the deposition of DLC film. He concluded that boiling near the electrode walls leads to a decrease in deposition rate and non-adhesive films. This issue can be resolved by lowering the applied voltage.

Table 5-5. Deposition parameters for fixed concentration and variable voltage.

Sr No.	Concentration of Acetic Acid	Applied Voltage (Volts)	Temperature (ºC)	Deposition Time (hrs)	Separation Distance (mm)
1		2.7			
2	2 %	4	Ambient	2	7
3		6			
4		8			
5		10			

However, a decrease in the potential leads to a decrease in current density but the deposition rate will also be decreased. This problem can be overcome by decreasing the separation distance between the electrodes. Moreover, at the lower separation distance between the electrodes, there is a great probability of radicals or ions arriving at a desirable electrode before recombination [10].

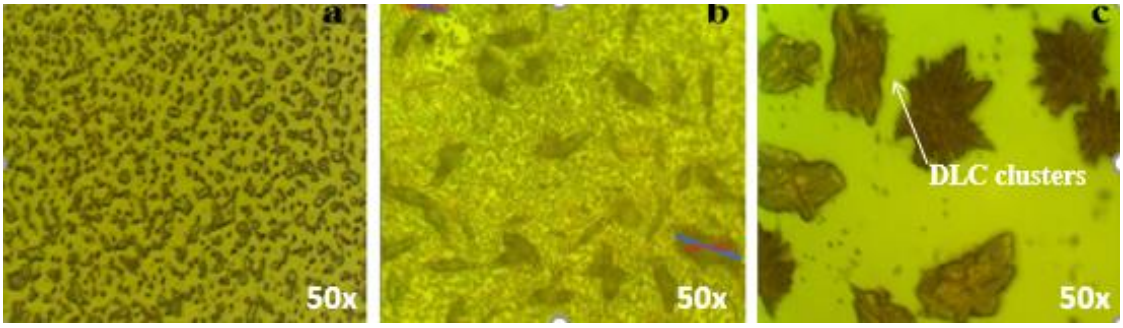

Figure 5-16. Optical microscopic images of DLC film at 50X on different voltages. (a) 2.7V (b) 6V (c) 10V

5.2.5 Functional & Structural Analysis of DLC film (FTIR)

DLC is the metastable form of amorphous carbon which is composed of hydrogenated carbon that contains a significant amount of sp^3 bonds. In this present work, DLC film is fabricated through electrodeposition by using the aqueous solution of acetic acid. The absorption spectra of DLC film were taken at 2% and 10% concentrations of acetic acid. The spectra show that there is several peaks present at 2800-3100 cm^{-1}. This region is the existence of hydrogenated carbon bonds.

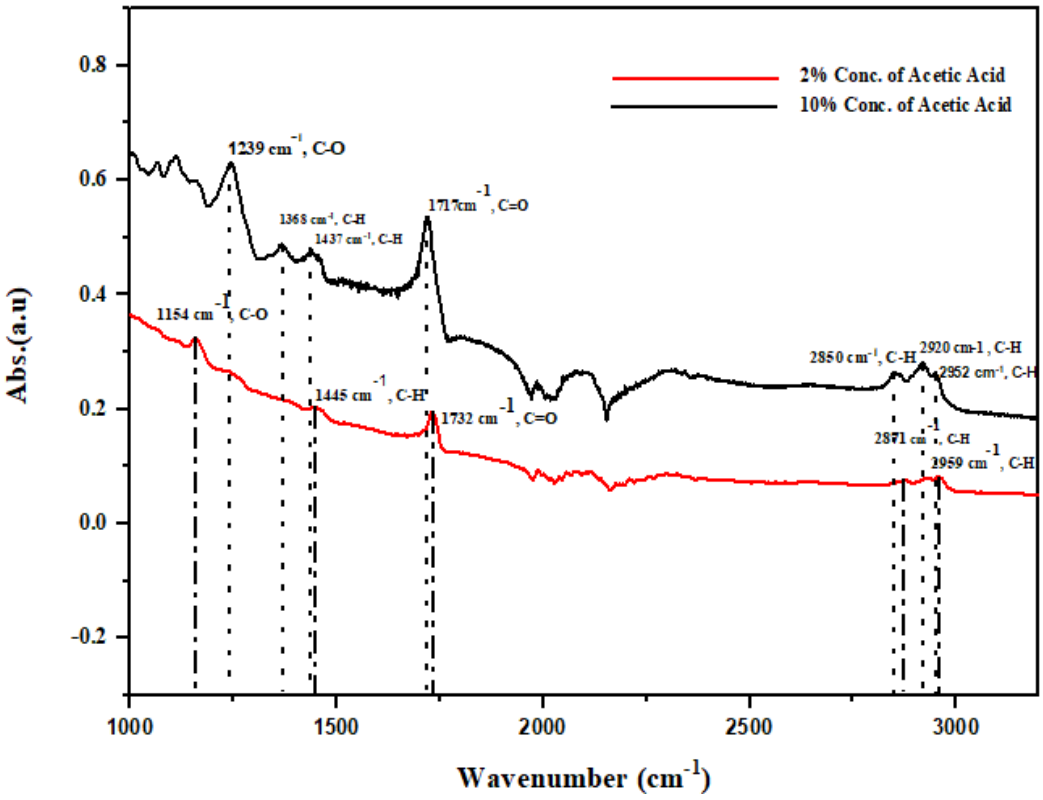

Figure 5-17. FTIR spectra of DLC film deposited at 2% and 10% conc. of acetic acid.

These absorption spectra of the DLC film have been de-convoluted into three peaks; they are due to anti-symmetrical vibrations of sp^3 -CH_3, vibrations of sp^3 - CH, and symmetrical vibrations of sp^3 -CH_2. The spectra are dominated by two peaks at ~2920 and 2850 cm^{-1}, which could be related to the sp^2-CH group and sp^3-CH modes, respectively. Two highly dense peaks at 1732cm^{-1} and 1717cm^{-1} determine the C=O at 2% and 10% concentration of acid in solution respectively. There are two peaks at 1437 cm^{-1} and 1445 cm^{-1} with hydrogen and carbon bonds.

The data shows that the film is composed of hydrogenated carbon and has a substantial amount of sp^2 and sp^3 bonded carbon atoms. The ratio between sp^2 and sp^3 would be varied by changing the concentration of acetic acid in the solution.

Table 5-6. Absorption peaks of DLC film related to the previous work with different electrolytes.

Electrolyte	**Observe Frequency (cm^{-1})**	**Configuration**	**Reference**
Ethanol	2843	sp^3 CH_2 (Symmetric)	[6]
	2920	sp^3 CH	
	2960	sp^3 CH_3 (antisymmetric)	
Ethanol (80%) and Methanol (20%)	2841	sp^3 CH_2 (Symmetric)	[11]
	2916	sp^3 CH	
	2961	sp^3 CH_3 (antisymmetric)	
Chloroacetic acid aqueous	2850	sp^3 CH_2 (Symmetric)	[8]
	2920	sp^3 CH	
Acetic acid aqueous	2850	sp^3 CH_2 (Symmetric)	**Present work**
	2920	sp^3 CH	
	2952	sp^3 CH_3 (antisymmetric)	

.

5.2.6 Microstructural Analysis of DLC film (Raman Spectroscopy)

Raman spectroscopy is one of the most fascinating non-destructive techniques to determine the structural analysis of carbon-based materials. In amorphous carbon-based films like DLC, there is the deconvolution of Raman spectrum with two Gaussian

peaks by using the gaussian fitting; the D band and G band as shown in fig. 5.18. The D band Gaussian peak is in the range from 1300 cm^{-1} to 1400 cm^{-1} and the G band Gaussian peak is in the range of 1500 cm^{-1} to 1600 cm^{-1}. The D band is directly related to the C-C, disorder structure, or sp^3 hybridized bond while the G band relates to the C=C or interconnected carbon ring. Diamond is the allotrope of carbon that has face-centered cubic symmetry, which results in the triply degenerated first-order phonon. The Brillouin zone extension is much larger than the wave vector of incident light. Fig 5.18: shows the five Raman spectra for DLC film at different concentrations of acetic acid. Fig 5.18 a indicates the D and G peaks located at 1334 cm^{-1} (D line) and 1546 cm^{-1} (G line) having low intensity as compared to other peaks.

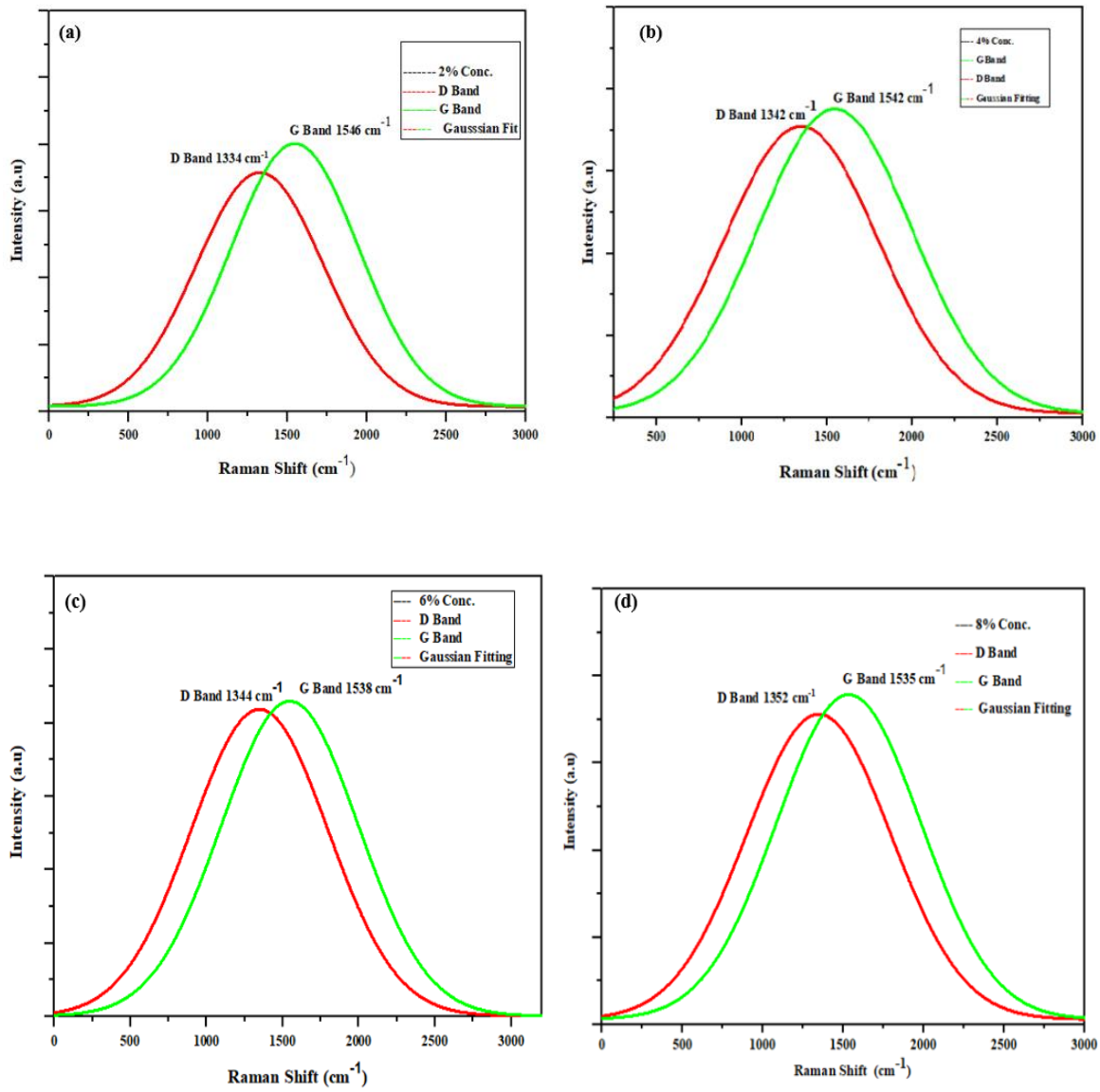

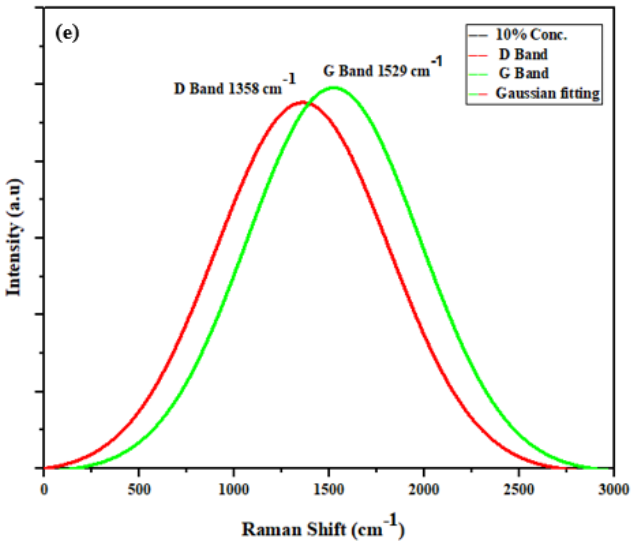

Figure 5-18. Deconvoluted Raman spectra for DLC film at different concentration of Acetic acid.

Table 5-7. I_D/I_G values at different concentration of acetic acid.

% Conc. of Acetic Acid	D Band Position (cm^{-1})	G Band Position (cm^{-1})	I_D/I_G
2%	1334	1546	0.860
4%	1342	1542	0.870
6%	1344	1538	0.875
8%	1352	1535	0.880
10%	1358	1529	0.890

DLC film deposited at 2% and 4% concentration of acetic acid having uniform and compact grains. As the increase in the concentration of acetic acid, disorders in the film such as the D band peak increased from 1334 cm^{-1} to 1358 $cm^{-1}$and graphitic behavior (G peak) shifted from 1546 cm^{-1} to 1529 cm^{-1} due to an increase in the concentration of methyl group and hydrogen ions. Raman spectra show that hydrogenated amorphous carbon film is directly associated with the microcrystalline graphite and diamond crystals that is the indication of a diamond-like carbon structure.

As shown in figure 5-19; G peak position was shifted as increasing the conc. of acetic acid in the electrolytic bath. The film deposited at 10 % concentration having low graphitic effect and disorders or carbon single bond in the film was increase as increase in the concentration. As clearly shown in table 5-7; the D and G band positions vary by

changing the concentration and I_D/I_G ratio was also dependent on the concentration of the solution.

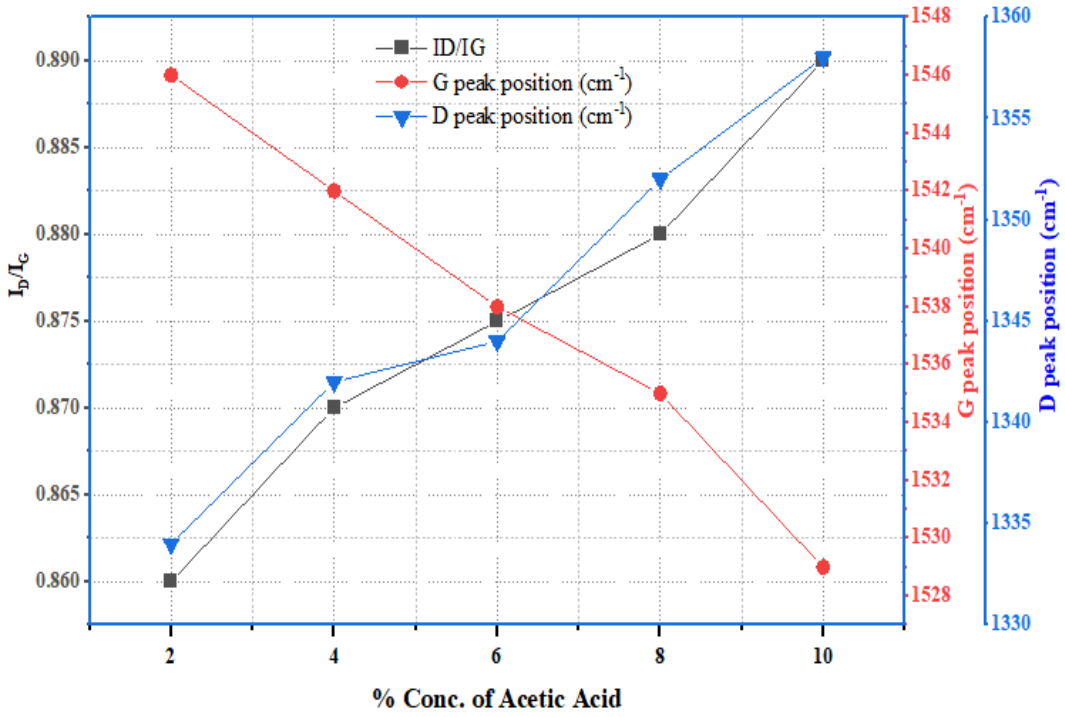

Figure 5-19. Impact of acetic acid concentration on intensity ratio (I_D/I_G), G peak and D peak.

Table 5-8. Previous findings of I_D/I_G ratio for DLC films deposited by various methods.

Techniques	**I_D/I_G**	**Reference**
Electrodeposition Route	0.6-0.8	[12]
Electrodeposition Route	0.8-0.9	[13]
Electrodeposition Route	0.9	[14]
Plasma CVD Technique	0.7	[15]
Plasma immersion implantation-deposition	0.5-1.6	[16]
PECVD	0.3-0.4	[17]
Electrodeposition	0.86-0.89	**Present work**

5.2.7 UV-VIS NIR Analysis of La-doped ZnO film (UV-VIS NIR Spectroscopy)

DLC film was coated onto the conductive glass to determine the optical characteristics such as absorption coefficient, transmission, and reflection of desirable material.

The absorption coefficient of each film was determined in the range of (300-1200nm). The absorption coefficient was calculated by using equation (1).

$$\boldsymbol{\alpha = \left(\frac{A}{hv}\right)\{hv\ - E_g\}^m} \qquad (6.7)$$

Where,

α is the absorption coefficient, A is the constant value that depends on the transition indicated by the value m, h denotes the Planck's constant, v symbolises the frequency, E_g is represents the optical bandgap.

It can be written as

$$\boldsymbol{\ln(\alpha hv) = \ln A + m \ln(hv - E_g)} \qquad (6.8)$$

And

$$\boldsymbol{\left[\frac{d(\ln(\alpha hv))}{d(hv)}\right] = \frac{m}{(hv - E_g)}} \qquad (6.9)$$

Equation (6.9) express the plot between $\left[\frac{d(ln(\alpha hv))}{d(hv)}\right]$ and hv that would signify the divergence at $hv = E_g$ from which the rough approximation of the bandgap can be attained. The obtained values of the bandgap have a good correlation with the previous finding. Fig 5-20c. In the infrared and visible region, DLC film is highly transparent. As increase the acetic acid concentration in DI water, the absorption coefficient reduces, and the bandgap increase. The absorption coefficient is dependent on the presence of hydrogen content and sp^2 bonding in the film. During the deposition, there is some oxygen content present in the film that was confirmed through the EDX results. Oxygen plays an important role in the affecting of the absorption coefficient. The absorption coefficient of 10% conc. the sample was low as compared to others because oxygen content is high as found in the EDS analysis. Table 5-4 reveals the variation in oxygen content with changing the concentration of acetic acid in the electrolytic bath.

An optical band gap is correlated to the absorption coefficient by using the Tauc equation. For the direct transition, the plot of $(\alpha hv)^2$ vs hv and extrapolate its linear

portion to $(\alpha hv)^2$=0 values attain the corresponding value of E_g. Bandgap was varied between 2.91 eV to 3.39 eV as shown in fig. 5-20 (a). It is practically confirmed that the bandgap increases after increasing the volume ratio of acetic acid in the electrolytic bath. The increase in the bandgap is due to the deposition of a high content of methyl group and hydrogen ions on the substrate surface. In the case of Hydrogenated DLC film, hydrogen content plays an important role to optimize the optical properties of the film.

Hydrogen content in the DLC film terminates the dangling bonds of carbon. Lowering the sp^2 content and then widening the bandgap of the film. As shown in the literature, Angus et al. [18] and Discher et al. [19] described that the optical bandgap of the carbon-based films is reduced by reducing the content of hydrogen in the film. The presence of the localized states in E_g because of free sp^3 states and a various number of clusters of sp^2 bonds. The distribution of clusters shape and size would define the value of the band gap. As shown in the reflection, transmission, and absorption coefficient graphs; the transmission is high due to low absorption coefficient and reflection. At higher concentrations, absorption coefficient value is low, averagely > 80 % of light has transmitted through the DLC film and 50 % to 60 % light was less reflected as compared to the bare substrate. Sample prepared at 10 % conc. of acetic acid was low reflection and highly transparent in the visible and IR region and had a low absorption coefficient value of the film.

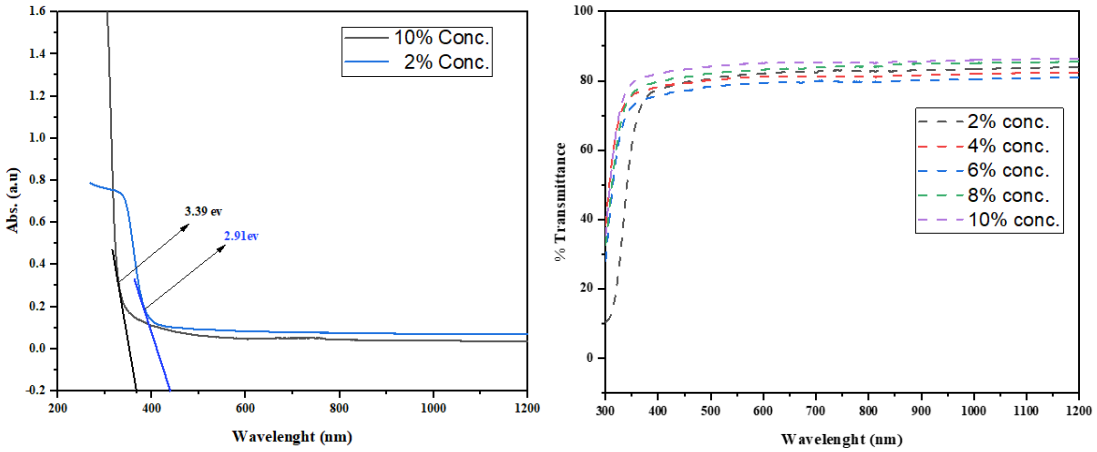

(a) **(b)**

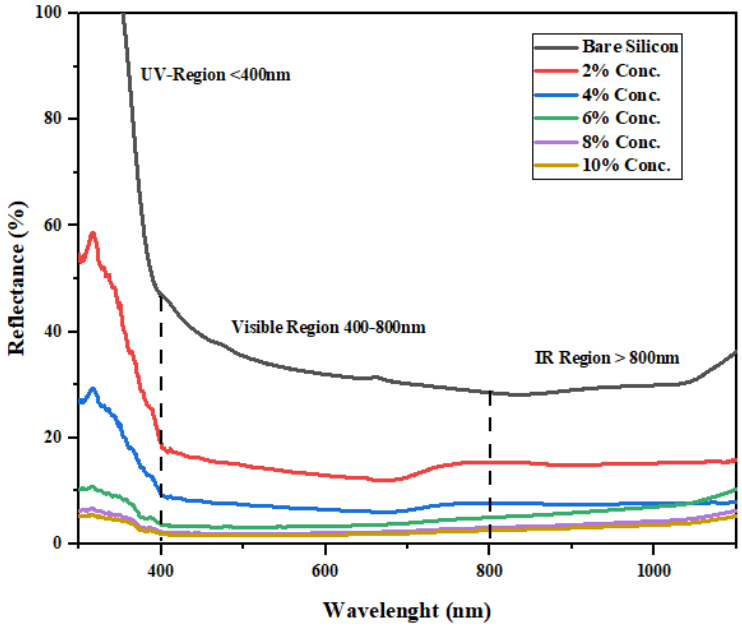

(c)

Figure 5-20. (a) Abs. Spectra of DLC film at 2% and 10% conc. solution (b) Transmission spectra of DLC film at different concentrations. (c) Reflectance spectra of the substrate after depositing DLC film.

5.3 Characterization of DLC film synthesized via PECVD

5.3.1 Functional & Structural Analysis of DLC film (FTIR)

DLC is the metastable form of amorphous carbon which is composed of hydrogenated carbon that contains a significant amount of sp^3 bonds. In this present work, DLC film is fabricated through the plasma-enhanced chemical vapor deposition technique by using methane and hydrogen as precursor gasses.

The absorption spectra of FTIR were taken of both deposited DLC film at ambient and 100 ^{o}C substrate temperature. The spectra show that there are several peaks present at 2800-3100cm^{-1}. This region is the existence of hydrogenated carbon bonds. These absorption spectra of the DLC film have been de-convoluted into three peaks; they are due to anti-symmetrical vibrations of sp^3 -CH_3, vibrations of sp^3 - CH, and symmetrical vibrations of sp^3 -CH_2. The spectra are dominated by two peaks at ~2918 and 2855 cm^{-1}, which could be related to the sp^2-CH group and sp^3-CH modes, respectively.

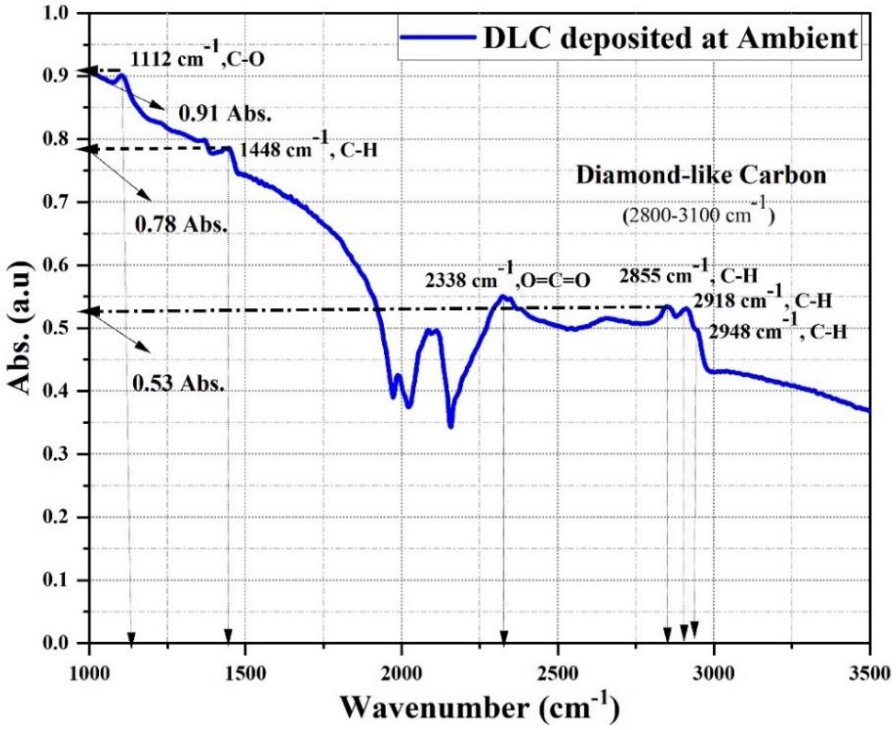

Figure 5-21. FTIR spectra for DLC deposited at Ambient Temp.

Two highly dense peaks at 2333 cm^{-1} and 2338 cm^{-1} determine the C=O at 100 ^{o}C and ambient temperature deposited DLC, respectively. There are two peaks at 1445 cm^{-1} and 1448 cm^{-1} with hydrogen and carbon bonds at different temperatures. As the temperature increase, the wavenumber shifts from higher to lower because at high temperature the concentration of the carbon double bonds increases and decrease the content of hydrogen inside the desirable thin film.

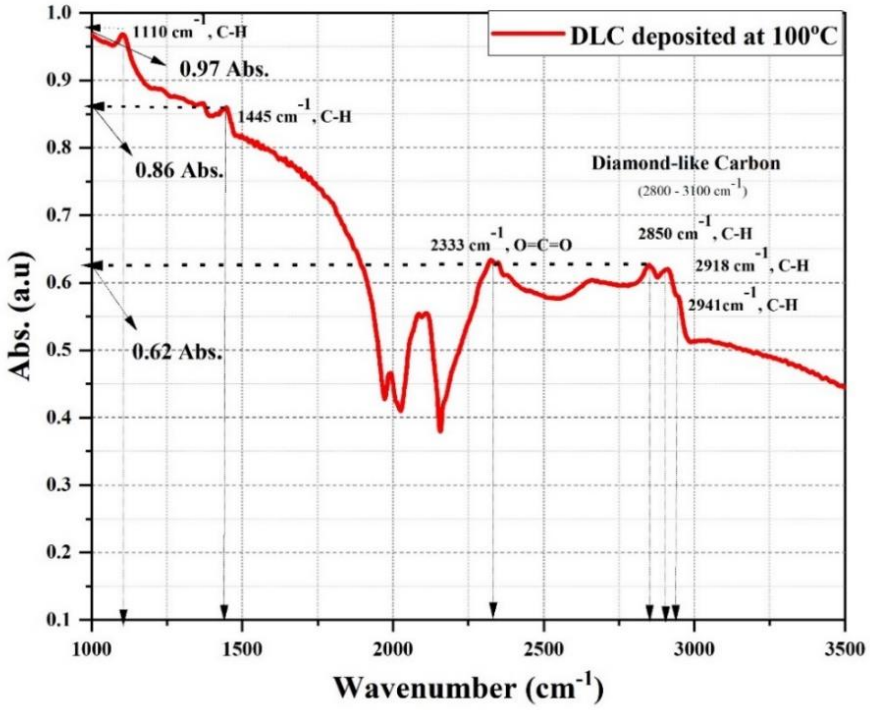

Figure 5-22. FTIR spectra for DLC deposited at 100 °C.

5.3.2 Microstructural Analysis of DLC film (Raman Spectroscopy)

Raman Spectroscopy is a non-destructive technique that is used to gain information about chemical, structural, molecular interactions of the carbon-based material. It is based on the interaction of light and interaction with each other. (Chemical Bonds within a material)

In amorphous carbon-based films like DLC, there is the deconvolution of Raman spectrum with two Gaussian peaks by using the gaussian fitting; the D band and G band as shown in fig. 5.23. The D band Gaussian peak is located in the range from 1200 cm^{-1} to 1400 cm^{-1} and the G band Gaussian peak is located in the range of 1500 cm^{-1} to 1600 cm^{-1}. The D band is directly related to the C-C, disorder structure, or sp^3 hybridized bond while the G band relates to the C=C, or interconnected carbon ring [20].

Diamond is the allotrope of carbon that has face center cubic symmetry, which results in the triply degenerated first order phonon. The Brillouin zone extension is much larger than the wave vector of incident light. As shown in figure 5.23; The intensity of the D band position is high as compared to the G band position. D band position is related to the carbon single bonds that help to transmit the light through the material

and G band position is related to the carbon double bonds that help to absorb the light. The presence of D and G band positions at the range of 1208 cm^{-1} and 1517 cm^{-1}, respectively.

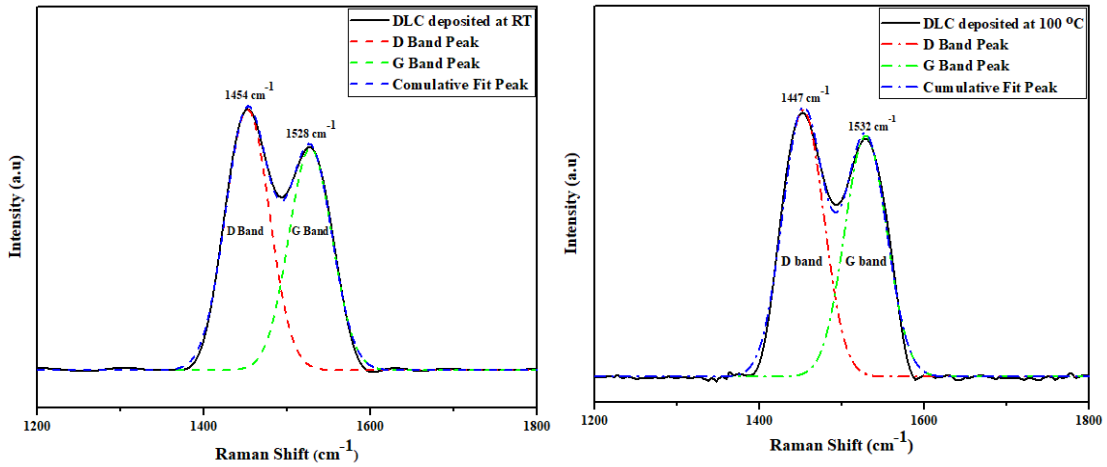

Figure 5-23. Raman spectra for DLC at Ambient Temperature and 100 °C.

The transmission of light is dependent on the concentration of the methyl radicals that helps to transmit the light from the material. Raman spectra show that hydrogenated amorphous carbon film is directly associated with the microcrystalline graphite and diamond crystals that is the indication of a diamond-like carbon structure.

5.3.3 UV-Vis NIR Analysis of DLC film (UV-VIS NIR Spectroscopy)

Optical properties of the synthesized DLC film were analyzed by a UV-Vis spectrophotometer to determine the transmission and absorption of the light through the material. To investigate the effect of the substrate temperature, we determine the optical characteristics of the DLC film at room temperature and 100 °C. In the literature, there is a variation of the thickness at the deposition of the DLC film at different substrate temperatures. As shown in the FTIR spectra, the substrate temperature directly depends on the properties of the synthesized DLC film.

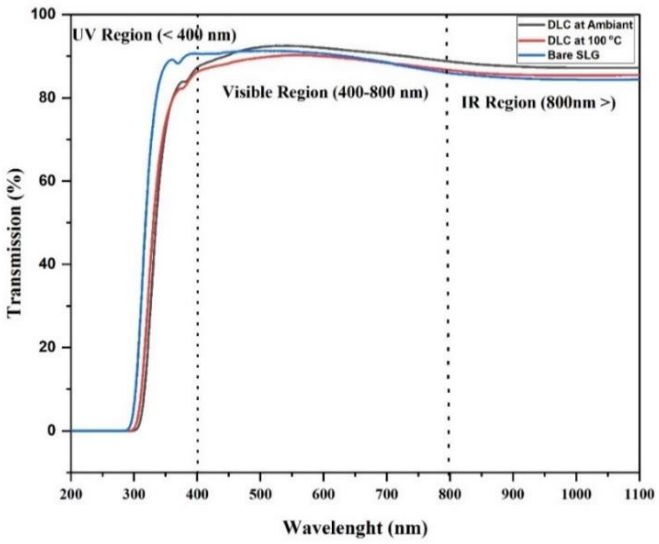

(a)

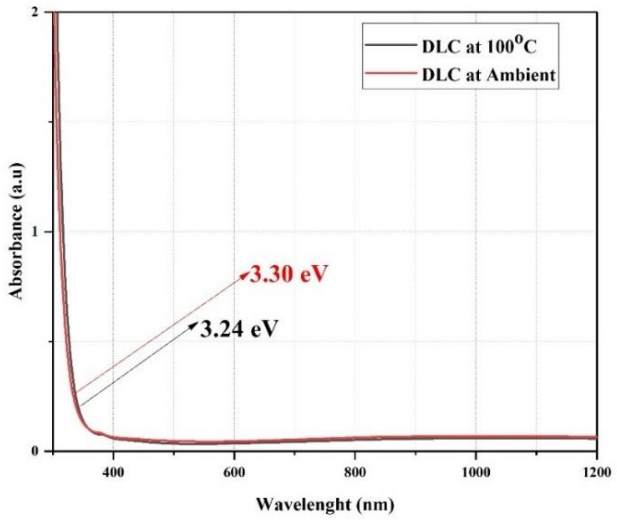

(b)

Figure 5-24. (a) Transmission spectra of the DLC film. (b) Absorption spectra of DLC film.

Table 5-9. Comparison of Average Transmission of light at various regions.

Sr#	DLC deposited Samples	Visible region (Avg transmission %)	IR region (Avg transmission %)
1	Bare SLG	89.6	82.5

2	Ambient deposited DLC	90.8	87.4
3	100 ^{o}C deposited DLC	88.7	85.5

DLC deposited at 100 ^{o}C shows a little bit low transmission of light in the visible region as compared to the Bare SLG. The reason for the transmission is that the deposition of the methyl radicals over the surface of the substrates. Now, diamond has the property to transmit light because they have to contain the number of carbon single bonds and graphite have the properties of the absorption of light due to containing carbon double bonds. DLC thin film has both the properties of diamond and graphite.

In the IR region, the average transmission of the light was 87.4% which is more than bare SLG glass and DLC coated SLG at 100 ^{o}C. The bandgap was varied between 3.30 to 3.24 eV. The concentration of the methyl radicals and the formation of carbon double or single bonds are dependent on the bandgap value. Sample prepared at ambient conditions are highly transparent in the visible and IR region and have a low absorption coefficient value of the film.

5.3.4 Water Contact Angle (WCA) measurement

As can be seen in the illustration, the form of water droplets on various materials demonstrates the two sorts of states (hydrophilic and hydrophobic) that exist. In the recent past, researchers are working on the wettability properties of the DLC film over the surface of different substrates. An element like silicon, oxygen, and nitrogen influence the water contact angle of the film because they are incorporated the structure of the DLC coating. The roughness of the film is directly associated with the water contact angle. DLC films are composed of hydrogenated carbon. There is a presence of C-C and C=C in the film.

In sample 5-25 (a); the contact angle of water with silicon substrates shows the high adhesion and high surface energy so that's why it shows a low contact angle (39^{o}) and looks hydrophilic. On the other hand, the hydrophilic condition of a surface indicates that the water adheres well to it and is acquired by a high surface free energy. Other

samples such as 5-25 (b); show the high contact angle of 102° with the surface of the silicon substrate because of the increase in the roughness and make low free surface energy with the surface of the substrate.

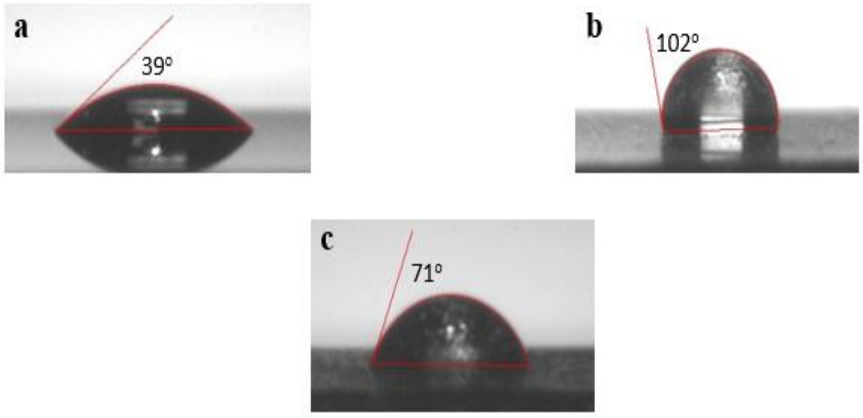

Figure 5-25. (a) Bare Silicon substrate. (b) DLC deposited at ambient. (c) DLC deposited at 100°C.

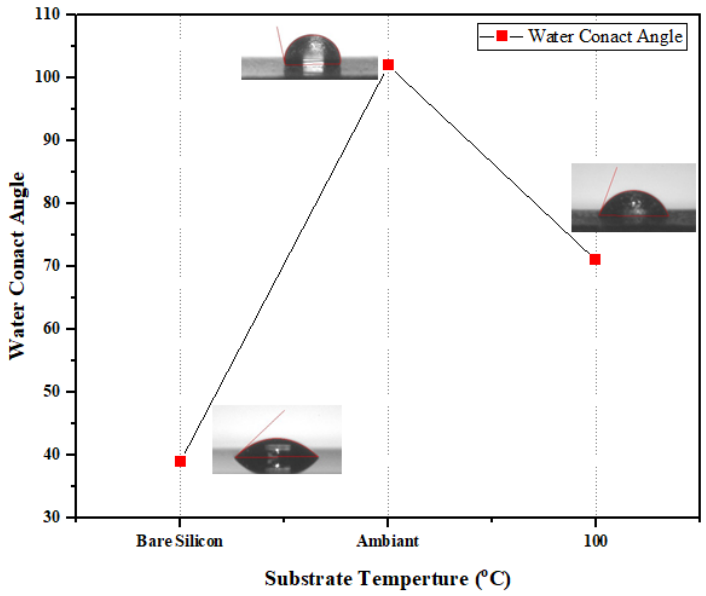

Figure 5-26. Relation between WCA and Substrate Temp.

In figure 5-25 (c); depicts that the water contact angle with the surface of the substrate makes a low contact angle of 71° as compared to the DLC deposited sample at ambient conditions. The major reason for the decrement in the WCA is a decrease in the roughness of the film. Both seem to be favorable for increasing the active groups capable of forming hydrogen bonds with water and therefore increasing the wettability and making the surface more hydrophilic.

References

1. He, H-Y., et al. "La-doping content effect on the optical and electrical properties of La-doped ZnO thin films." *Journal of Materials Science: Materials in Electronics* 26.2 (2015): 1205-1211.
2. Güldalı, Özlem Ertek, and İbrahim Okur. "Microstructural and optical properties of La-doped ZnO thin films deposited by spin coating on quartz glass." (2018)
3. Pandey, Padmini, et al. "Effects of annealing temperature optimization on the efficiency of ZnO nanoparticles photoanode based dye sensitized solar cells." *Journal of Materials Science: Materials in Electronics* 28.2 (2017): 1537-1545.
4. S. U. Awan, Z. Mehmood, S. Hussain, S. A. Shahcd, N. Ahmad, M. Rafique, M. Aftab, T. A. Abbas, Correlation between structural, electrical, dielectric and magnetic properties of semiconducting Co doped and (Co, Li) co-doped ZnO nanoparticles for spintronics applications, Physica E Low Dimens. Syst. Nanostruct. 103 (2018) 110-121.
5. Mrabet, C., et al. "Effects of surface oxygen vacancies content on wettability of zinc oxide nanorods doped with lanthanum." *Journal of Alloys and Compounds* 688 (2016): 122-132.
6. Roy, R. K., et al. "Synthesis of diamond-like carbon film by novel electrodeposition route." *Thin solid films* 422.1-2 (2002): 92-97.
7. Gupta, S., et al. "Low voltage electrodeposition of diamond-like carbon films." *Materials letters* 57.22-23 (2003): 3479-3485.
8. Paul, R., et al. "Hydrophobicity in DLC films prepared by electrodeposition technique." *Applied Surface Science* 255.5 (2008): 1705-1711.
9. Zhang, Qian, et al. "Low voltage and ambient temperature electrodeposition of uniform carbon films." *Electrochemistry Communications* 63 (2016): 22-25.
10. Sreejith, K., J. Nuwad, and C. G. S. Pillai. "Low voltage electrodeposition of diamond like carbon (DLC)." *Applied surface science* 252.2 (2005): 296-302.
11. Ismail, R.A., A.M. Mousa, and M.A.J.M.S.i.s.p. Hassan, *Synthesis and characterization of diamond-like carbon film on silicon by electrodeposition from solution of ethanol and methanol.* 2014. **27**: p. 461-467
12. Modabberasl, A., et al., *Fabrication of DLC thin films with improved diamond-like carbon character by the application of external magnetic field.* 2015. **94**: p. 485-493.
13. Yan, X., et al., *Characterization of hydrogenated diamond-like carbon films electrochemically deposited on a silicon substrate.* 2004. **37**(17): p. 2416.
14. Wang, Y., W. Yang, and C.J.C.l. Chen, *Liquid-phase electrodeposition of diamond-like carbon films on conducting glass substrates using a low deposition voltage at room temperature.* 2008. **37**(6): p. 636-637.
15. Hodgman, C., *Handbook of Chemistry and Physics, CD Hodgman, ed*. 1957, Chemical Rubber Publishing Co., Cleveland, OH.
16. Namba, Y.J.J.o.V.S., S. Technology A: Vacuum, and Films, *Attempt to grow diamond phase carbon films from an organic solution.* 1992. **10**(5): p. 3368-3370.
17. Xiao, Y., et al., *The effect of radio frequency power on the structural and optical properties of a-C:H films prepared by PECVD.* Journal of Materials Research, 2017. **32**(7): p. 1231-1238

18. Angus, J.C. and C.C.J.S. Hayman, *Low-pressure, metastable growth of diamond and" diamondlike" phases.* 1988. **241**(4868): p. 913-921.
19. Dischler, B., A. Bubenzer, and P.J.A.P.L. Koidl, *Hard carbon coatings with low optical absorption.* 1983. **42**(8): p. 636-638.
20. Yang, Qinru, et al. "Research on the fabrication and anti-reflection performance of diamond-like carbon films." *Diamond and Related Materials* 111 (2021): 108184.

Chapter 6: Conclusions and Future Recommendations

6.1 Conclusions

- DLC and Lanthanum doped ZnO thin film were fabricated through vapor phase deposition and a wet chemistry approach. Lanthanum doped ZnO was synthesized through sol-gel and spin-coating techniques DLC film was deposited via two ways i.e., Electrodeposition and PECVD.
- With the increase in the lanthanum content, particle size was reduced and transmission in the range (300-1100nm) was first to increase and then decrease at different atomic % of lanthanum content. The bandgap was varied between 3.22-3.29 eV. Moreover, the resistivity level in the synthesized film was first decreased and then increase after increasing the lanthanum content. Increased lanthanum content in ZnO shows a more hydrophilic nature of the film.
- In Electrodeposited DLC film, SEM results depicted that small and compact grains were formed at a lower voltage, and the roughness of the film increases by increasing the concentration of acetic acid in the solution.
- UV-Vis NIR spectroscopy shows that the bandgap of the DLC film increased by increasing the deposition of CH_3^+ particles on the substrate surface. More than 80 % of transmission is achieved in the visible and IR region at higher concentrations. Up to 50 % of reflection was reduced over the surface of bare silicon and conductive glass.
- In the PECVD technique, FTIR analysis confirms the DLC formation that shows intense peaks at 2855 cm^{-1}, 2918 $cm^{-1,}$ and 2948 cm^{-1} at ambient temperature.
- UV-Vis NIR spectroscopy shows that the bandgap of the DLC film decreased by decreasing the deposition of CH_3^+ particles on the substrate surface. More than 90% of transmission is achieved in the visible and IR region at ambient temperature deposited DLC film.
- Due to an increase in the roughness of the film, DLC formation at ambient shows a higher water contact angle and makes the surface hydrophobic.

6.2 Future Recommendations

We recommend several studies for future research work about the current study. Such studies would helpfully explore those aspects of this work that haven't been analyzed here due to certain limitations, especially time and facilities-related constraints.

Preparation Methods for DLC formation

Devising facile, low-cost, and nonacidic methods for DLC material preparation (Suggested: Acetonitrile).

Use of Lanthanum doped ZnO NPs as Photoanode material

Due to the increase in optoelectrical and improvement in hydrophilic properties of Lanthanum doped ZnO thin film, Nanoparticles of Lanthanum doped ZnO may be utilized as photoanode material for DSSCs devices that help to increase the adsorption of dye inside the photoanode material.

Used as IR window

Several coatings like SiO_2, MgF_2, ZnO, Si_3N_4 and SiN:H, etc. are also used for multilayer protective and anti-reflective coatings. DLC films have a broad variety of bandgaps and flexible refractive index, they may be utilized surface as anti-reflective coatings (ARC) for space solar cells and protective coatings for Infrared windows

Capability to replace fluoride-based coatings

Diamond like carbon (DLC) film may be replaced by the conventional fluoride-based IR optical coating like BaF_2, PbF_2, and ThF_4 that has poor mechanical and adhesive strength. DLC coating has better wear resistance as compared to the conventional anti-reflection coating. So, we may use DLC coating rather than any fluoride-based material coating.

Utilized as Space SCs

DLC coating is practically convenient for space SCs. Because major issues related to the solar cell reflection surface can also be resolved by using coating like DLC. Another problem is the requirement of protection from harmful irradiation like ϒ-quanta encountered in space.

Working on Deposition Parameter

Diamond-like carbon film formation at low temperature may give better results as compared to DLC film formed at high temperature. The sp^3 structure of carbon atoms in the DLC film attributes to the low-level adhesion produced by the internal stress which might be increased at high temperatures.

Use as Anti soiling coatings

Due to the hydrophobic nature of DLC coated thin film, it may be utilized as an antisoiling coating in Photovoltaic applications.

Appendix A

Diamond-Like Carbon Film Deposited Via Electrochemical Route for Antireflection Applications in Photovoltaic.

Altamash Shabbir[1,a] , Zuhair S. Khan[1,b *], Asghar Ali[1,c], Wajahat Qasim[1,d], Nisar Ahmed[1,e], Zain Hussain[1,f], Hina Pervaiz[1,g]

[1] U.S-Pakistan Centre for Advanced Studies in Energy (USPCAS-E), National University of Sciences and Technology (NUST), Sector H-12, Islamabad, Pakistan

[a] mshabbirese19.ces@student.nust.edu.pk, [* b]zuhair@uspcase.nust.edu.pk, [c]asghar@uspcase.nust.edu.pk, [d]wqasimese19.ces@student.nust.edu.pk, [e]17teenisar@uspcase.nust.edu.pk, [f]zhussaintee19.ces@student.nust.edu.pk , [g]hpervaizphdf19.ces@student.nust.edu.pk

Keywords: Diamond-like Carbon, Electrodeposition, Antireflection Coating.

Abstract

Diamond-like carbon (DLC) is widely studied for various applications such as optoelectronics, energy, aerospace, and medicine. It's hard, chemically inert, and optically transparent. Due to its superior antireflection properties, DLC films are more suited for photovoltaic technology. Here in this work, we report a facile, high speed, and low-cost method of DLC film development from an aqueous solution via electrodeposition. The effect of applied voltage and solution concentration on the properties of DLC film was analyzed. The morphology, shape, and uniformity of the DLCs were analyzed with optical and electron microscopies. The presence of C-H, C-C, and C=C bonds in the DLC films was confirmed from FTIR and Raman spectroscopies. Whereas the optical behavior was analyzed with a UV-Vis-NIR spectrophotometer. The DLC films were deposited at 2.7 V, 4V, 6V, 8V, and 10V, and it was shown that for a fixed electrolyte concentration and electrode spacing, the applied voltage can be adjusted to obtain varying deposition rates. Likewise, the solution concentration was varied in the 2 vol.% to 10 vol.%, and it was demonstrated that by increasing the solution concentration the deposition rate increases. The increase in the deposition rate was evidenced by an increase in the deposition current as well as the roughness of the films. It was noticed that smaller-sized, well-defined, and more uniform DLC films were obtained at lower concentrations and low voltage levels. The band gap was varied between 2.91ev to 3.39ev. It was clearly shown that reflection reduced remarkably after depositing DLC film on the substrate surface. This work demonstrates that DLC film has a potential to utilized as an antireflection layer in photovoltaic application.

1. Introduction

Diamond-like Carbon (DLC) is an amorphous class of carbonaceous material that is composed of hydrogen and carbon that contains a substantial amount of sp^3 hybridization. Diamond-like carbon (DLC) coatings have been widely studied due to their potential use in many applications like medical, defense, energy sector, electro-optical devices, aerospace, and other fields. They have great industrial interest due to their exclusive properties such as high mechanical stress, chemical stability, huge wear resistance, dielectric strength, low friction, extreme electrical resistance, and high optical transparency. There are several numbers of chemical and physical methods that are used to deposit DLC film, such as sputtering, pulsed laser deposition (PLD), filtered vacuum arc, Electron cyclotron resonance chemical vapor deposition, ion beam deposition, and plasma-enhanced CVD (PECVD) [3, 4].

The electrodeposition technique is a simple route to deposit a film on the substrate surface. Electrodeposition is getting intentions to the researchers because of its many advantages, such as lower deposition temperature, simple experimental setup, easily controllable parameters, low cost, and the possibility of a large area for deposition, as compared to the PVD and CVD techniques [5]. Most of the material that can be deposited by the vapor phase can also be deposited from the liquid phase via electrodeposition. Methanol (CH_3OH), 2-propanol ((CH_3) CHOH), ethanol (CH3CH2OH), tetrahydrofuran (C4H8O), acetone (CH3COCH3), and acetic acid (CH3COOH), and acetonitrile (CH3CN) are the organic liquid that can be used for the DLC formation via electrodeposition. Organic liquid as an electrolyte is majorly dependent on the dipole moment, dielectric constant, and viscous coefficient. Dipole moment defines itself alignment of a molecule with respect to the field and dielectric constant determine the maximum field that can be applied [6].

In the previous studies, DLC film deposited on the silicon substrate was done at high voltage. The first experiment was performed by *Namba* in 1992, he successfully deposited Diamond-like carbon film on silicon substrate by using the electrolysis of alcohol at a temperature under 70^{o}C and high voltage [7]. *Ismail et al.* deposited DLC film deposited on silicon from electrodeposition at 1200V by varying the ratio of ethanol to methanol content [8]. *Ceo et al.* used methanol as a carbon source to deposit DLC film on a silicon substrate, the deposited film was composed of compact and small grains [9].

In the current study, we will analyze the morphological, structural, optical changes in the DLC film on silicon substrate by varying the concentration of acetic acid in the electrolytic bath at 2.7 volts. The effect of voltage on the DLC film formation will also be investigated at a fixed concentration.

2. Experimental Setup

2.1 Materials and Method

Diamond-like carbon film was synthesized by the electro-deposition route. DLC film was deposited on the silicon substrate and conductive glass. Acetic acid and DI water used as an electrolyte. Rubber is used as an insulator to separate the distance between the electrodes. A 300 volts DC power supply was used to apply potential. Copper wires were used as a connector with electrodes.

The graphite plate was mounted at the anode, and it acted as a counter electrode. Silicon substrate was mounted at the cathode and used as a working electrode. The separation

distance of 7mm was maintained between the electrodes. Before deposition, the silicon substrate was cleaned with acetone and ethanol sequentially and then rinsed in DI water. After cleaning with solvents, the oxide layer was removed by purging argon gas in plasma cleaner. 1.5 M acetic acid solution was used as an electrolyte. The deposition was carried out at room temperature and atmospheric pressure. The voltage was kept fixed, and the concentration of the acetic acid was varied between 2% to 10%. The reaction was carried out at 2.7V for 2 hours. To determine the effect of voltages, an experiment was also performed at different voltages by fixing the concentration of acetic acid shown in table 1.

Table 1. Deposition parameters for fixed concentration and variable voltage.

Sr No.	**Concentration of Acetic Acid**	**Applied Voltage (Volts)**	**Temperature (ºC)**	**Deposition Time (hours)**	**Separation Distance (mm)**
1	2 %	2.7 V	Ambient	2 hours	7mm
2		4 V			
3		6 V			
4		8 V			
5		10 V			

Table 2. Deposition parameters for fixed voltage and variable concentration of acetic acid.

Sr No.	**Concentration of Acetic Acid**	**Applied Voltage (Volts)**	**Temperature (ºC)**	**Deposition Time (hours)**	**Separation Distance (mm)**
1	2%	2.7 V	Ambient	2 hours	7mm
2	4%				
3	6%				
4	8%				
5	10%				

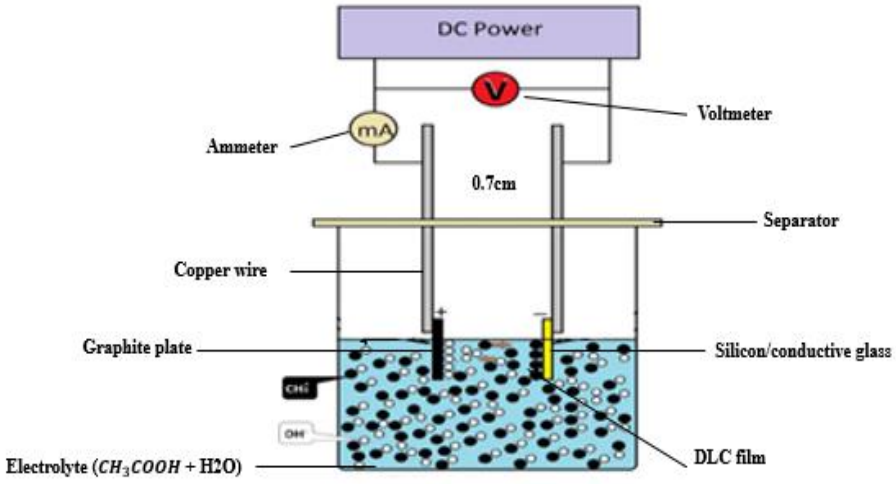

Fig. 1. Schematic of Electrodeposition setup.

2.2. Instruments and characterization

Surface morphology was analyzed by using the Scanning electron microscope (VEGA 3 LMU, TESCAN). Structural characteristics of DLC film was observed by using Raman spectroscopy by using 532nm laser and FTIR (Agilent Cary 630). The Optical properties like absorption coefficient of the DLC film, reflectance, and transmittance was measured by using the ultraviolet visible spectrometer.

3. Results and Discussion

3.1 Reaction Mechanism

An assortment of apposite electrolytes for the DLC formation by using the electrochemical approach would highly be dependent on the dipole moment and dielectric constant of the electrolyte. Dipole moment signifies the basic ionic nature while the strength of the electric field between the anode and cathode indicates by the dielectric constant. A solution of acetic acid (σ; 1.74×10^{-18} esu, ε; 6.15) and water (σ; 1.87×10^{-18} esu, ε; 80.37) appeared as the right choice for the selection of electrolyte meanwhile the comparative values mentioned above can be changed by varying the concentration of water and acetic acid.

Under an electric field, the aqueous solution of acetic acid tends to ionize. The large concentration of methyl radicals and H_2 ions is deposited at the surface of the cathode during the process of electrolysis. The major prerequisite to deposit Diamond-like Carbon film and diamond films, deposition of a high concentration of hydrogen ions and methyl radicals at the surface of the substrate must be satisfied.

Overall Reaction:

$$CH_3COOH \rightarrow CH_3^+ + CO + OH^- \quad (1)$$

Cathode Reaction

$$2CH_3 + 2e^- \rightarrow 2C + 3H_2 \quad (2)$$

Anode Reaction

$$2OH^- \rightarrow O_2 + H_2O + 4e^- \quad (3)$$

During the electrolysis, the aqueous solution of acetic acid was converted into the methyl ions and gaseous form of carbon monoxide. Different hybridized form of carbon has been formed on the substrate surface. There is the formation of water and oxygen at the surface of the anode while depositing of OH^- ions [10].

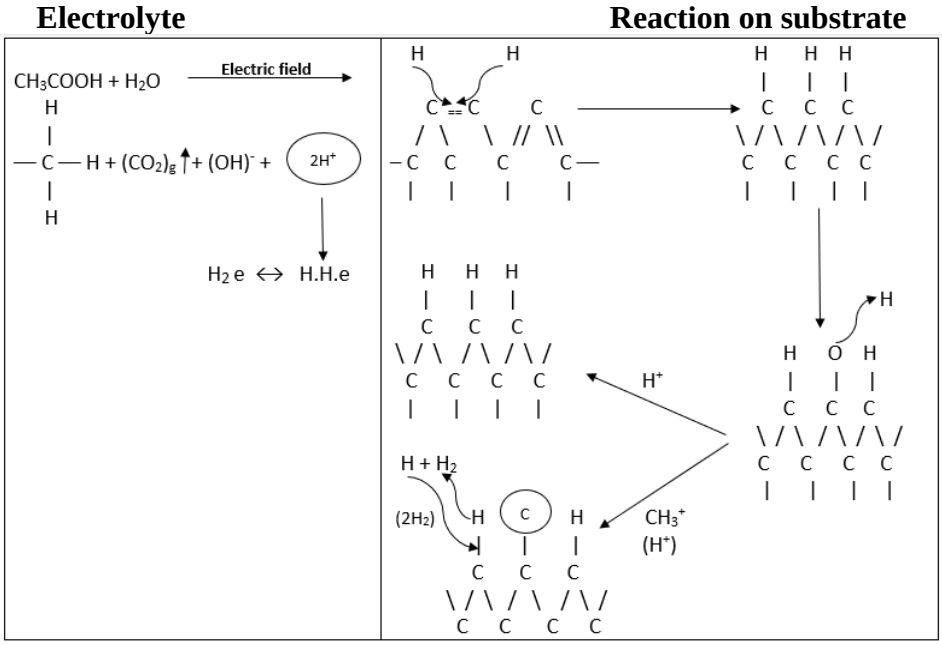

Fig. 2. Reaction mechanism of DLC formation over the surface of the substrate by using aqueous acetic acid as an electrolyte [10].

3.2 I-V characteristics of Electrolytic Bath

Fig. 3 shows the I–V characteristic of the electrolytic bath. It can be observed that the electrolytic conduction starts at 1.2V. After increasing the voltage, the deposition current increase exponentially and the rate of deposition also increased. In the previous studies, *S. Gupta.* used the acetonitrile and DI water as an electrolyte, they observed that current density increases exponentially after the threshold voltage of ~12V [11]. Current density increases by increasing the voltage and then the deposition rate also enhanced because a large number of ions move towards the working electrode.

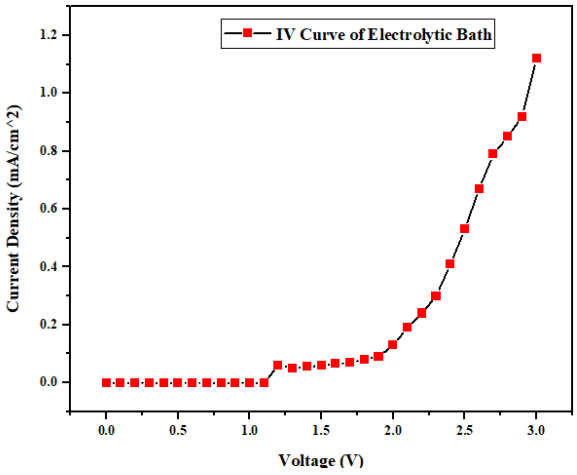

Fig. 3. I-V characteristic of electrolytic bath at 2% concentration of Acetic acid.

3.3 Effect of Voltage on DLC film Formation

As shown in Table 1. DLC film was deposited at different voltages from 2.7 V to 10 V and fixed the concentration of acetic acid. As shown in SEM images; DLC film is quite uniform and having compact grains at 2.7 V. The deposition of DLC film at 4 to 10 volts having the formation of clusters and the size of clusters increases by increasing the voltage up to 10V (as shown in fig. 4). As shown in the literature; Usually deposition from organic liquid source mostly carried out at high voltage (400-3000V) and marginally higher than room temperature. At high voltage, the organic liquid near the electrode walls starts to boil. This issue is resolved by lowering the applied voltage. However, a decrease in the potential leads to a decrease in current density but the deposition rate will also be decreased. This problem can be overcome by decreasing the separation distance between the electrodes. Moreover, at the lower separation distance between the electrodes, there is a great probability of radicals or ions arriving at a desirable electrode before recombination [12].

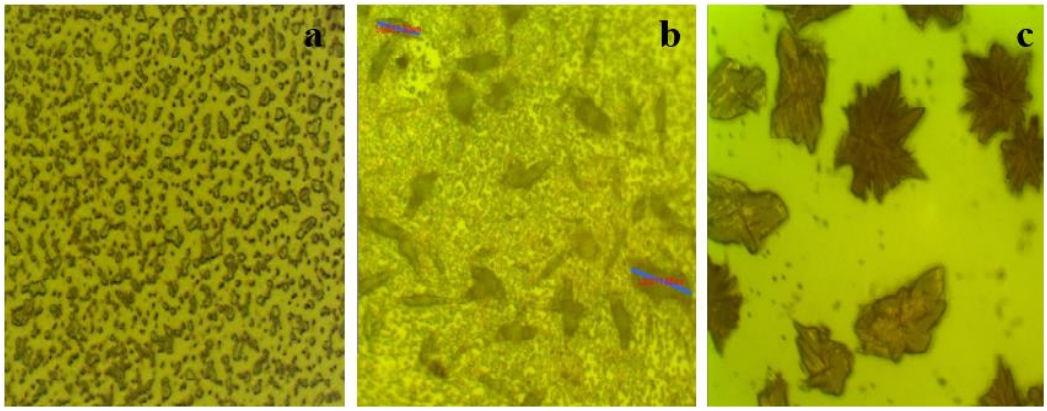

Fig. 4. Optical microscopic images of DLC film at 50X on different voltages. a) 2.7V b) 6V c) 10V.

3.4 Surface Analysis

Fig.5 (a & b) shown the morphological information about the DLC film. It was observed that the film was rough, and the roughness was increased by increasing the concentration of acetic acid in water. Small and compact grains were obtained at 2% (v/v) and 4% concentration of acetic acid in water as compared to the higher concentration of acetic acid. We observed that the film was uniform and well defined at a lower concentration of acetic acid. SEM images shows that at a lower concentration, less carbon is deposited as compared to a higher concentrated solution of acetic acid. During the electrolysis of the aqueous solution, a large number of methyl radicals and hydrogen ions were deposited because the concentration of acetic acid was high that have enough content of carbon as compared to the lower concentrated aqueous solution. This result is much correlated to the previous literature. *R. Paul et al* observed that at a lower concentration of acetic acid, small and compact grain was obtained. They also concluded that the roughness of the film was increase as increase the acetic acid concentration in the solution [13].

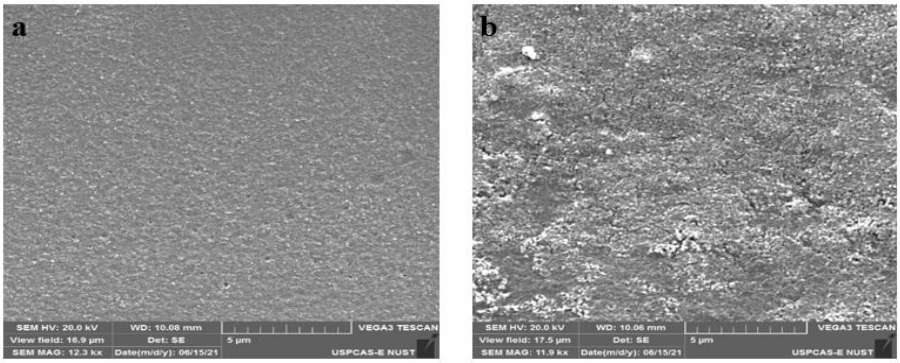

Fig. 5. SEM images of DLC film formed at different conc. of acetic acid. (a) 2% and (b) 10%.

3.5 Structural Analysis

FTIR analysis of fabricated DLC films were performed to take the absorption spectra at 2% and 10% concentration of acetic acid. The spectra shows that there are several peaks present at 2800-3100cm^{-1}. This region is the existence of hydrogenated carbon bonds [14].

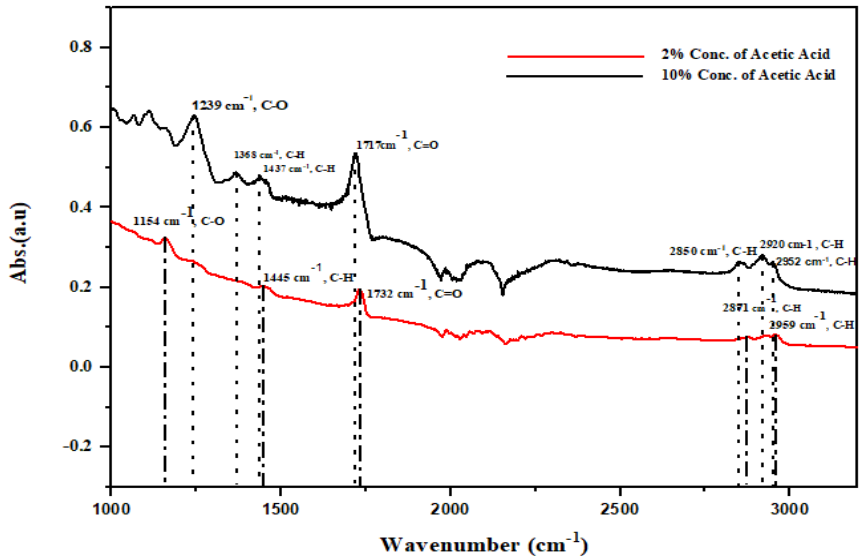

Fig. 6. FTIR spectra of DLC film deposited at 2% and 10% conc. of acetic acid.

These absorption spectra of the DLC film have been de-convoluted into three peaks; they are due to anti-symmetrical vibrations of sp^3 -CH_3, vibrations of sp^3 - CH, and symmetrical vibrations of sp^3 -CH_2.The spectra are dominated by two peaks at ~2850 cm^{-1} and 2920 cm^{-1}, which could be related to the sp^2-CH group and sp^3-CH modes, respectively. Two highly dense peaks at 1732 cm^{-1} and 1717 cm^{-1} determine the C=O at 2% and 10% concentration of acid in solution respectively. There are two peaks at 1437 cm^{-1} and 1445 cm^{-1} with hydrogen and carbon bonds. The above data shows that the film is composed of hydrogenated carbon and having a substantial amount of sp^2 and sp^3 bonded carbon atoms. The ratio between sp^2 and sp^3 would be varied by changing the concentration of acetic acid in the solution.

Raman spectroscopy is one of the most fascinating non-destructive techniques to determine the structural analysis of carbon-based materials. Amorphous carbon-based

films like DLC, there is the deconvolution of Raman spectrum with two Gaussian peaks by using the gaussian fitting; the D band and G band as shown in fig. 05. The D band Gaussian peak is located in the range from 1300 cm^{-1} to 1400 cm^{-1} and the G band Gaussian peak is located in the range of 1500 cm^{-1} to 1600 cm^{-1}. The D band is directly related to the C-C, disorder structure, or sp^3 hybridized bond while G band relates to the C=C, or interconnected carbon ring [15]. Fig 7. shows the five Raman spectra for DLC film at different concentrations of acetic acid. Fig 7a indicates the D and G peaks located at 1334 cm^{-1} (D line) and 1546 cm^{-1}(G line) having low intensity as compared to other peaks. DLC film deposited at 2% and 4% concentration of acetic acid having uniform and compact grains. As an increase in the concentration of acetic acid, disorder structure in the film such as D band peak increased from 1334 cm^{-1} to 1358 $cm^{-1}$and graphitic behavior (G peak) shifted from 1546 cm^{-1} to 1529 cm^{-1} due to an increase in the concentration of methyl radicals and hydrogen ions.

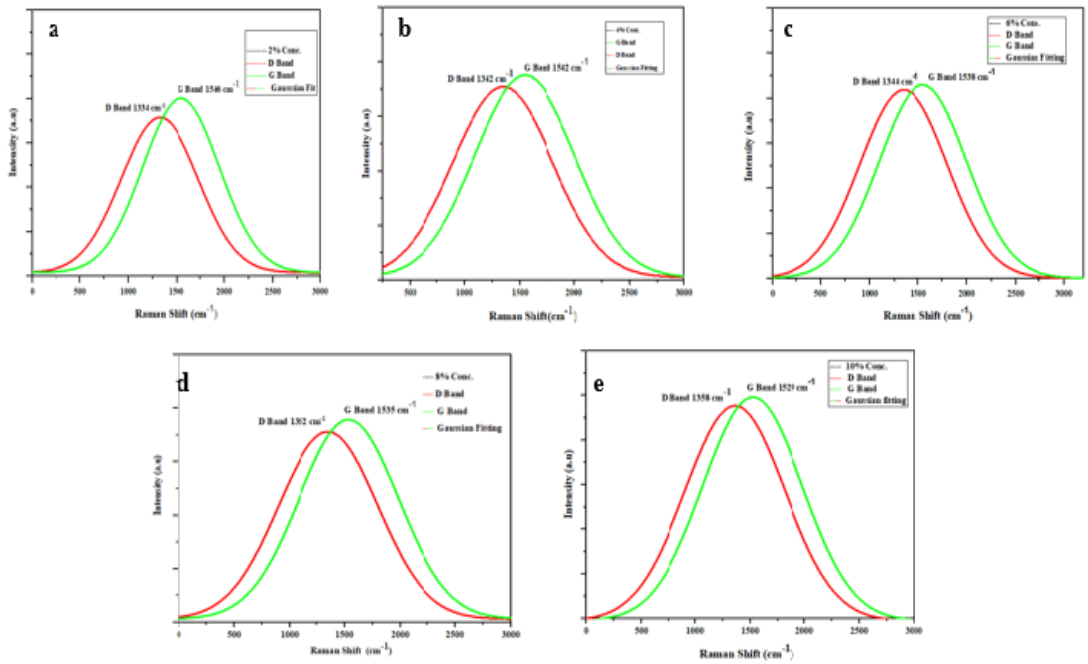

Fig. 7. Deconvoluted Raman Spectra for DLC film at different concentration of Acetic acid. a) 2% conc. solution b) 4% conc. solution c) 6% conc. solution d) 8% conc. solution e) 10% conc. solution

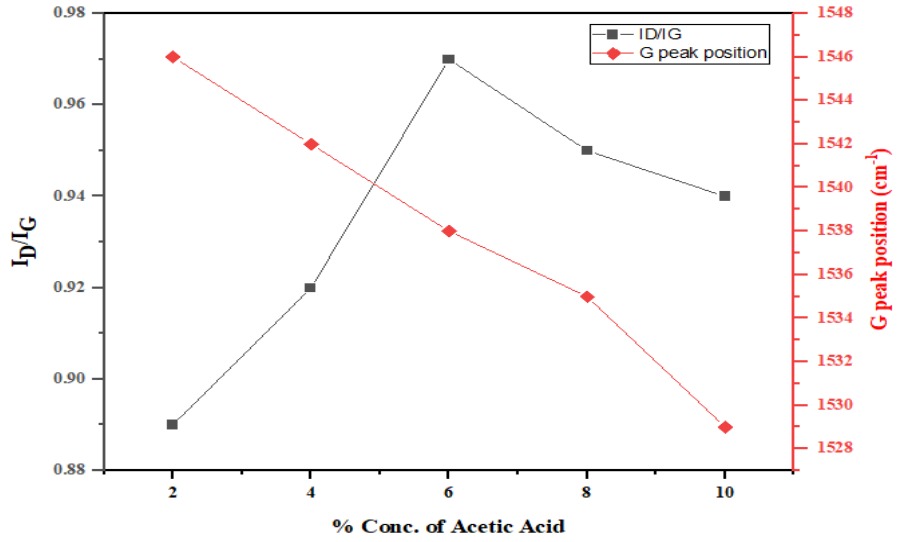

Fig 8. Impact of acetic acid concentration on intensity ratio and G peak position.

As shown in fig. 6; G peak position was shifted as increasing the conc. of acetic acid in the electrolytic bath. The film deposited at 10% concentration having low graphitic effect and disorder structure or carbon single bond in the film was increased as increase in the concentration. Raman spectra shows that hydrogenated amorphous carbon film is directly associated with the microcrystalline graphite and diamond crystals that is the indication of a diamond-like carbon structure.

Table 3: I_D/I_G values at different concentration of acetic acid.

% Conc. of Acetic Acid	D Band Position (cm^{-1})	G Band Position (cm^{-1})	I_D/I_G
2%	1334	1546	0.89
4%	1342	1542	0.92
6%	1344	1538	0.97
8%	1352	1535	0.95
10%	1358	1529	0.94

3.6 Optical Analysis

DLC film was coated onto the conductive glass to determine the optical characteristics such as absorption coefficient, transmission, and reflection of desirable material. The absorption coefficient of each film was determined in the range of (300-1200nm). The absorption coefficient was calculated by using equation (4) [16].

$$\alpha = \left(\frac{A}{hv}\right)\{hv - E_g\}^m \qquad (4)$$

Where, α is the absorption coefficient, A is the constant value that depends on the transition indicated by the value m, h denotes the Planck's constant, v symbolizes the frequency, E_g is represents the optical bandgap. It can be written as

$$ln(\alpha hv) = lnA + m\, ln(hv - E_g) \quad (5)$$

And

$$\left[\frac{d(ln(\alpha hv))}{d(hv)}\right] = \frac{m}{(hv - E_g)} \quad (6)$$

Equation (6) express the plot between $\left[\frac{d(ln(\alpha hv))}{d(hv)}\right]$ and hv that would signify the divergence at $hv = E_g$ from which the rough approximation of bandgap can be attained. The obtained values of the band gap having a good correlation with previous findings [15, 16]. Fig 9c. In the infrared and visible region, DLC film is highly transparent. As increase the acetic acid concentration in DI water, the absorption coefficient reduces, and the bandgap increase. Bandgap was varied between 2.91ev to 3.39ev as shown in fig. 09a. It is practically confirmed that the bandgap increases after increasing the volume ratio of acetic acid in the electrolytic bath. The increase in the bandgap is due to the deposition of high content of methyl radicals and hydrogen ions on the substrate surface. In the case of Hydrogenated DLC film, hydrogen content plays an important role to optimize the optical properties of the film. Hydrogen content in the DLC film terminates the dangling bonds of carbon [17]. Lowering the sp^2 content and then widening the bandgap of the film. As shown in the literature, *Angus et al.* and *Dischер et al.* described that the optical bandgap of the carbon-based films is reduced by reducing the content of hydrogen in the film [18, 19].

The presence of the localized states in E_g is because of free sp^3 states and the various number of clusters of sp^2 bonds. Distribution of clusters shape and size would define the value of the band gap. As shown in the reflection, transmission, and absorption coefficient graphs; the transmission is high due to low absorption coefficient and reflection. At higher concentrations, absorption coefficient value is low, averagely > 80% of light has transmitted through the DLC film and 50% to 60% light was less reflected as compared to the bare substrate. Sample prepared at 10% conc. of acetic acid was low reflection and highly transparent in the visible and IR region and having a low absorption coefficient value of the film.

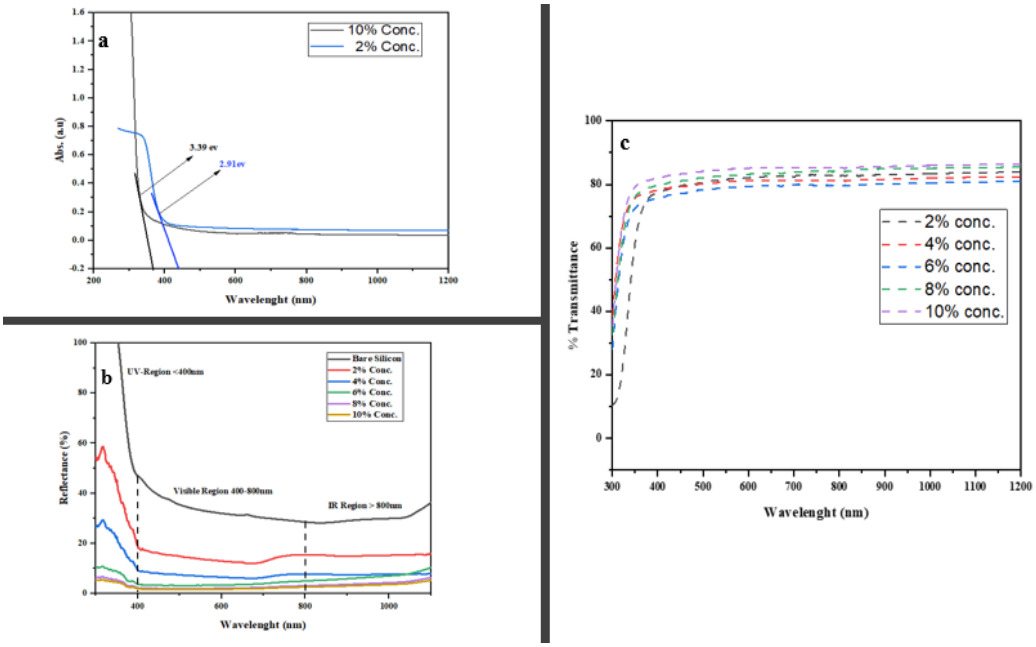

Fig. 9. a) Abs. Spectra of DLC film at 2% and 10% conc. solution. b) Reflectance spectra of substrate after depositing DLC film. c) Transmission spectra of DLC film at different concentrated. Solution.

4. Conclusion

Diamond-like carbon film was synthesized through the electrodeposition route at low voltage. According to the scanning electron microscopy results, small and compact grains were formed at low voltage and concentration solution. The roughness of the film increases by increasing the concentration of acetic acid in solution. When increasing the voltage level, the deposition current increases and then there was the formation of clusters of DLCs on the surface of a substrate. FTIR analysis confirms the DLC formation that shows intense peaks at 2850 cm^{-1}, 2920 $cm^{-1,}$ and 2952 cm^{-1} at 10% concentrated solution. A large number of methyl radicals and hydrogen ions are deposited at higher concentrations. Raman spectra show that hydrogenated amorphous carbon films are directly associated with the microcrystalline graphite and diamond crystals that is the indication of a diamond-like carbon structure. UV-Vis NIR spectroscopy shows that the bandgap of the DLC film increased by increasing the deposition of CH_3^+ particles on the substrate surface. More than 80% of transmission is achieved in the visible and IR region at higher concentrations. Up to 50% of reflection was reduced over the surface of bare silicon and conductive glass. DLC deposited from acetic acid as an electrolyte is one of the facile, high speed, and low-cost methods to fabricate antireflection coating. This finding can also be utilized in the solar field for protective and window layer applications.

5. Acknowledgment

PGP Directorate research department of the National University of Science and Technology (NUST) Pakistan has financially supported to complete of this Project.

References

1. REN, R.J.R.e.p.n.f.t.s.c.P., France: REN21 Secretariat, *Global status report.* 2015.
2. Kruskopf, M., et al., *Comeback of epitaxial graphene for electronics: large-area growth of bilayer-free graphene on SiC.* 2016. **3**(4): p. 041002.
3. Modabberasl, A., et al., *Fabrication of DLC thin films with improved diamond-like carbon character by the application of external magnetic field.* 2015. **94**: p. 485-493.
4. Yan, X., et al., *Characterization of hydrogenated diamond-like carbon films electrochemically deposited on a silicon substrate.* 2004. **37**(17): p. 2416.
5. Wang, Y., W. Yang, and C.J.C.l. Chen, *Liquid-phase electrodeposition of diamond-like carbon films on conducting glass substrates using a low deposition voltage at room temperature.* 2008. **37**(6): p. 636-637.
6. Hodgman, C., *Handbook of Chemistry and Physics, CD Hodgman, ed*. 1957, Chemical Rubber Publishing Co., Cleveland, OH.
7. Namba, Y.J.J.o.V.S., S. Technology A: Vacuum, and Films, *Attempt to grow diamond phase carbon films from an organic solution.* 1992. **10**(5): p. 3368-3370.
8. Ismail, R.A., A.M. Mousa, and M.A.J.M.S.i.s.p. Hassan, *Synthesis and characterization of diamond-like carbon film on silicon by electrodeposition from solution of ethanol and methanol.* 2014. **27**: p. 461-467.
9. Cao, C., H. Zhu, and H.J.T.S.F. Wang, *Electrodeposition diamond-like carbon films from organic liquids.* 2000. **368**(2): p. 203-207.
10. Roy, R., et al., *Synthesis of diamond-like carbon film by novel electrodeposition route.* 2002. **422**(1-2): p. 92-97.
11. Gupta, S. and R.J.E.A. Rahini, *Electrochemical synthesis and characterization of amorphous hydrogenated carbon (aC: H) using acetonitrile as electrolyte.* 2017. **258**: p. 1-8.
12. Tosin, M., et al., *Deposition of diamond and diamond-like carbon nuclei by electrolysis of alcohol solutions.* 1999. **144**: p. 260-264.
13. Paul, R., et al., *Hydrophobicity in DLC films prepared by electrodeposition technique.* 2008. **255**(5): p. 1705-1711.
14. Xiao, Y., et al., *The effect of radio frequency power on the structural and optical properties of a-C:H films prepared by PECVD.* Journal of Materials Research, 2017. **32**(7): p. 1231-1238.
15. Chang, C.-T., et al. *Electrodeposition of diamond-like carbon thin film on conductive indium-tin-oxide glass substrate*. in *2015 International Symposium on Next-Generation Electronics (ISNE)*. 2015. IEEE.
16. Ismail, R.A., et al., *Synthesis of diamond-like carbon films by electro-deposition technique for solar cell applications.* 2016. **48**(1): p. 1-11.
17. Choi, W.S., et al., *Diamond-like carbon protective anti-reflection coating for Si solar cell.* 2008. **62**(4-5): p. 577-580.
18. Angus, J.C. and C.C.J.S. Hayman, *Low-pressure, metastable growth of diamond and" diamondlike" phases.* 1988. **241**(4868): p. 913-921.
19. Dischler, B., A. Bubenzer, and P.J.A.P.L. Koidl, *Hard carbon coatings with low optical absorption.* 1983. **42**(8): p. 636-638.